Material Design and Engineering for Polymer Electrolyte Membrane Zinc-Air Batteries

by

Jing Fu

A thesis

presented to the University of Waterloo

in fulfillment of the

thesis requirement for the degree of

Doctor of Philosophy

in

Chemical Engineering

Waterloo, Ontario, Canada, 2018

Examining Committee Membership

The following served on the Examining Committee for this thesis. The decision of the Examining Committee is by majority vote.

External Examiner	Dr. Mark Obrovac Professor
Supervisor	Dr. Zhongwei Chen Professor
Internal Member	Dr. Mark Pritzker Professor
Internal Member	Dr. Michael Fowler Professor
Internal-external Member	Dr. Bo Cui Professor

Author’s Declaration

This thesis consists of material all of which I authored or co-authored: see Statement of Contributions included in the thesis. This is a true copy of the thesis, including any required final revisions, as accepted by my examiners.

I understand that my thesis may be made electronically available to the public.

Statement of Contributions

The body of this thesis is based upon a combination of published works. Various chapters are adapted from the following list of publications.

Chapter 1 and **Chapter 2** of this thesis consist of a review paper that was co-authored by myself, my supervisor, Drs. A. Yu, and M. Fowler, and two PhD students, Z. Cano and M. Park. Z. Cano and I contributed equally to the paper and M. Park assisted with the writing of the paper. All authors reviewed the manuscript.
"Electrically rechargeable zinc-air batteries: progress, challenges and perspectives", *Advanced Materials*, 29 (2017) 51604685.

Chapter 3 of this thesis consists of a paper that was co-authored by myself, my supervisor, a PhD student, M. Park, two post-doctoral fellows, Drs. D. Lee and F. Hassan, and two collaborators, Drs. L. Yang and Z. Bai. I designed and carried out the experiment, collected and analyzed the data, as well as the writing of the manuscript. Dr. Lee and Dr. Hassan assisted with the writing of the manuscript. M. Park helped with the synthesis of a control catalyst of $LaNiO_3$. All authors reviewed the manuscript.
"Flexible high energy polymer-electrolyte-based rechargeable zinc-air batteries", *Advanced Materials*, 27 (2015) 5617-5622.

Chapter 4 of this thesis consists of a paper that was co-authored by myself, my supervisor, three PhD students, J. Zhang, H. Zarrin, L. Rasen, and four collaborators, Drs. X. Song, X. Tian, J. Qiao, K. Li. I designed the experiment, and Drs. Tian, Song, and Li synthesized and supplied the raw cellulose fibers. I carried out the lab experiment, collected and analyzed the data, as well as the writing of the

manuscript. J. Zhang and H. Zarrin assisted with the functionalization of nanocellulose. L. Rasen helped with drawing a cover image. All authors reviewed the manuscript.

"A flexible solid-state electrolyte for wide-scale integration of rechargeable zinc-air batteries", *Energy & Environmental Science*, 9 (2016) 663-670.

Chapter 5 of this thesis consists of a paper that was co-authored by myself, my supervisor, a post-doctoral fellow, Dr. F. Hassan, a Co-op student, H. Liu, and collaborators, Drs. J. Lu, C. Zhong, and A. Yu. I designed and carried out the experiment, collected and analyzed the data, as well as the writing of the manuscript. Dr. Hassan contributed in the experimental design and review. H. Liu assisted with the synthesis of catalysts. Dr. Lu helped with the writing of the paper. All authors reviewed the manuscript.

"Defect engineering of chalcogen-tailored oxygen electrocatalysts for rechargeable quasi-solid-state zinc air batteries", *Advanced Materials*, (2017)10.1002/adma.201604685.

Chapter 6 of this thesis consists of a paper that was co-authored by myself, my supervisor, two post-doctoral fellows, Drs. F. Hassan and J. Li, four PhD students, D. Lee, A. Ghannoum, G. Lui, A. Hoque, Dr. Hassan and I designed the experiment together. I carried out the lab experiments, collected and analyzed the data, as well as the writing of the manuscript. D. Lee and Dr. Hassan assisted with the writing of the manuscript. G. Lui and A. Ghannoum contributed to the characterization of the material. All authors reviewed the manuscript.

"Flexible rechargeable zinc-air batteries through morphological emulation of human hair array", *Advanced Materials*, 28 (2016) 6421-6428.

Abstract

Zinc-air batteries, whose advantages include relatively high energy density (1218 Wh kg^{-1}), abundance of zinc in earth's crust, and very safe operational characteristics, are promising for applications in consumer electronics, electrified transportation, grid storage, and other fields. At the moment, primary zinc-air batteries are produced for low-drain electronic gadgets such as hearing aids. However, secondary (i.e., electrically rechargeable) zinc-air batteries have eluded widespread adoption due mainly to the slow reaction kinetics of oxygen evolution at the air electrode during recharge. A bifunctional oxygen electrocatalyst that can recharge the batteries more efficiently is required. Moreover, in the presence of aqueous alkaline electrolytes, zinc-air batteries suffer from low durability and performance loss due mainly to the formation of zinc dendrites during charging, the loss of aqueous electrolytes, the detachment of the catalyst layer and the precipitation of carbonates at the air electrode. These persistent issues have motivated a shift in electrolyte design towards efficient hydroxide ion-conductive polymeric electrolytes. A combination of efficient bifunctional oxygen electrocatalysts and polymeric electrolyte improvements may enable zinc-air batteries to be implemented in widespread applications in flexible/lightweight electronic devices and electric vehicles.

In this work, I present a feasible strategy combining material innovations with engineering methods to develop a new type of zinc-air battery, i.e., a flexible, rechargeable polymer electrolyte membrane zinc-air battery (PEMZAB). In the first study, a proof of concept of a film-shaped, rechargeable PEMZAB was conducted by using a KOH-doped poly(vinyl alcohol) (PVA) gel electrolyte, porous zinc electrode and bifunctional air electrode

comprising a commercial Co_3O_4 nanoparticles-loaded carbon cloth. Then, a novel hydroxide ion-conductive polymeric electrolyte membrane and an efficient bifunctional oxygen electrocatalyst were synthesized and characterized, respectively, for further improvements in zinc-air battery performance. Specifically, highly quaternaized cellulose nanofibers were synthesized to produce a hydroxide ion-conductive electrolyte membrane (referred to as QAFC). The QAFC membrane shows advantages of a high ionic conductivity of 21.2 mS cm^{-1}, good chemical stability, mechanical robustness and flexibility, and inhibition of zinc dendrites and carbonations. In addition to the QAFC electrolyte membrane development, a hybrid bifunctional oxygen electrocatalyst, consisting of cobalt oxysulfide nanoparticles and nitrogen-doped graphene nanomeshes ($CoO_{0.87}S_{0.13}$/GN), was prepared. The defect chemistries of both oxygen-vacancy-rich cobalt oxysulfides and edge-nitrogen-rich graphene nanomeshes lead to a remarkable improvement in electrocatalytic performance, where $CoO_{0.87}S_{0.13}$/GN exhibits strongly comparable catalytic activity and much better stability than the best-known benchmark noble metal catalysts.

A simple, water-based filtration method for a direct assembly of the QAFC membrane and the $CoO_{0.87}S_{0.13}$/GN catalyst film was demonstrated with the PEMZAB. Such a fabrication approach enables intimate contact between the solid-solid catalyst-electrolyte interfaces for facile charge transfer. Moreover, benefiting from the performance improvement of the QAFC electrolyte membrane and the $CoO_{0.87}S_{0.13}$/GN bifunctional catalyst, the resulting battery possesses a higher energy density of 857.9 Wh kg^{-1} and a more stable cycling performance, over 300 hours of operation at 20 mA cm^{-2} under ambient conditions, than those of a battery using PVA-KOH gel electrolyte and commercial Co_3O_4 bifunctional catalysts.

In the last study, the knowledge gained from the hybrid $CoO_{0.87}S_{0.13}$/GN bifunctional catalyst is transferred to the fabrication of a hybrid catalyst/current collector assembly for the bifunctional air electrode. In this assembly, a hair-like array of mesoporous cobalt oxide nanopetals in nitrogen-doped carbon nanotubes is grown directly on a stainless-steel mesh through chemical vapor deposition and electrodeposition methods. Such integrative design not only ensures a large number of catalytically active sites in a given electrode surface, but also increases the electron transfer between each individual catalyst and the conductive substrate. This advanced air electrode assembly further boosts the PEMZAB performance, with a high peak power density of 160.7 mW cm^{-2} at 250 mA cm^{-2} and a remarkable cycling durability: lasting over 600 hours of operation at 25 mA cm^{-2} under ambient conditions.

Acknowledgements

I would like to thank my advisor Professor Zhongwei Chen who gave me the opportunity to work on the topic of zinc-air batteries, and who guided and encouraged me throughout my Ph.D. studies. He gave me the freedom to pursue various research ideas; without his support, I would never have accomplished so much. Also, I want to thank my Ph.D. thesis examining committee, including Professor Mark Pritzker, Professor Michael Fowler, Professor Bo Cui from the University of Waterloo, and Professor Mark Obrovac as my external examiner from Dalhousie University for their time and contributions through this important process.

Special thanks go to Dr. Fathy Hassan for sharing his thoughts on both research and life in general, and to Dr. Dong Un Lee for his support and assistance at the beginning of my Ph.D. study. Also, I want to thank my outstanding colleagues in the Applied Nanomaterials & Clean Energy Laboratory for all the help and fun we have had in the last four years.

Moreover, I would like to express my gratitude to my parents for their unconditional support, encouragement and love. I also want to thank my former Director Mr. ZW Wang at Volvo Cars for encouraging me to pursue a doctoral degree at the University of Waterloo.

Finally, I would like to acknowledge the funding sources, Natural Sciences and Engineering Research Council of Canada, Ontario Graduate Scholarship, the Waterloo Institute for Nanotechnology, and the University of Waterloo, for the financial support during the completion of my project.

Table of Contents

List of Figures

List of Tables

List of Abbreviations

BET – Brunauer-Emmett-Teller

CV – Cyclic voltammetry

CNF – Cellulose nanofibers

CVD – Chemical vapor deposition

DDI – Distilled de-ionized

EDS – Energy dispersive X-ray spectroscopy

ELNES – Electron energy loss near-edge structure

EV – Electric vehicles

GO – Graphene oxide

GDL – Gas diffusion layer

Ir/C – Carbon support iridium catalyst

ORR – Oxygen reduction reaction

OER – Oxygen evolution reaction

NCNT – N-doped carbon nanotube

Pt/C – Carbon support platinum catalyst

PEMZAB – Polymer electrolyte membrane zinc-air battery

QAFC – quaternary ammonia-functionalized nanocellulose membrane

RDE – Rotating disc electrode

RHE – Reversible or reference hydrogen electrode

SAED – Select area electron diffraction

SEM – Scanning electron microscopy

STEM – Scanning transmission electron microscopy

SS – Stainless steel

TEM – Transmission electron microscopy

TGA – Thermogravimetric analysis

XPS – X-ray photoelectron spectroscopy

XRD – X-ray diffraction

Chapter 1 Introduction

1.1 Motivation

Batteries are electrochemical energy storage devices that power many electronic devices and play a vital role in our everyday activities. With the popularity of more mobile and interactive lifestyles, it is becoming more and more important to find batteries not only to fulfill energy requirements but also to afford certain flexibility and thinness.[1] Particularly, the growing interest in portable and flexible electronics, such as healthcare patches, wearables, and sensors, requires decreased form factors to the existing rigid, bulk-size batteries – a limitation of the materials and their fabrication methods.[2] Today lithium-ion batteries (200-300 Wh kg^{-1}) are the main solutions for the most portable consumer electronics, but they use liquid and flammable organic electrolytes, thus struggling to achieve safety, flexibility, and other special mechanical properties for more widespread market penetration. Thin, flexible lithium-polymer batteries have been available for over 10 years, yet they have had limited commercial success due to premium pricing, as well as the fact that they offer lower energy density (less than 120 Wh kg^{-1}) than traditional lithium-ion or other established Ni-based rechargeable batteries.[3] To advance with viable flexible electronics, the preferred battery technology to be developed must be the most compelling fit between high energy density, sufficient power, extended cycle life, flexibility, safety, and cost advantages.

In this decade there has been renewed interest in the development of zinc-air battery technologies, due to their high theoretical specific energy (1086 Wh kg^{-1}, calculation using the mass of ZnO) and volumetric energy density (6136 Wh L^{-1}, calculation using the density of

ZnO),[4] inherent safety using aqueous electrolytes, and cost advantage of using the earth-abundant zinc. A high volumetric energy density is particularly desirable for portable and flexible electronic devices because there is a limited volume for mounting the batteries in these applications. Conventional zinc-air batteries are typically operated in aqueous alkaline (e.g., KOH) electrolyte solutions that have high ionic conductivities.[5] However, such the alkaline solutions are difficult to handle especially at the flexible devices because of their corrosive nature and leakage problem. To avoid these complications, a solid-state electrolyte is desired to allow easy shaping of the device and to increase operational resiliency against extreme conditions, such as vibrations, impact, and compression. Ion-conductive polymers are attractive as potential solid electrolytes because of their processing simplicity in different form factors for a variety of solid-state devices.[6] But such solid systems generally face difficulties in maintaining fast ion transport in the solid electrolyte, that is, the ionic conductivity is a few orders of magnitude lower than that of aqueous systems. Further enhancements of the ionic conductivity may be reached with suitable nanostructures and surface functionalization of the polymers.[7, 8] Despite improvements in polymeric electrolytes, their compatibility with the electrode surfaces, in terms of the solid-electrolyte-electrode interfacial conductivity, also poses a challenge to rechargeable zinc-air battery performance (e.g., rate capability and cycling stability).[9] Several strategies for the cell fabrication route have been developed to improve the interfacial conductivity.[10-13]

In addition to the polymeric electrolytes, another challenge hampering the performance and reversibility of the zinc-air battery stems from difficulties in achieving fast reaction kinetics for both oxygen reduction and evolution reactions at the air electrode; thus an efficient

bifunctional oxygen electrocatalyst is necessary to promote these processes. The improvement of both the activity and stability of the bifunctional oxygen electrocatalysts would lead to an appreciable improvement of power performance and energy efficiency.[14] Meanwhile, there are physical limits to how much catalyst can be loaded onto the planar air electrode without inhibiting charge and mass transport.[15] Typically, catalysts are made into inks and coated onto a carbon-based gas diffusion layer (GDL) to prepare the air electrode.[16] The process of making catalyst inks requires introducing polymer binders to form a thin film and provide a good connection between the catalysts and the GDL, which will affect the electronic conductivity of the whole air electrode and eventually lead to a large ohmic polarization of the battery performance. What is worse, during the battery operation, the degradation of polymer binders always causes aggregation and/or leaching of nanostructured catalysts, which results in poor electrochemical activity and durability of the electrode. Therefore, the development of advanced bifunctional electrocatalysts that enable implementation of binder-free air electrodes could be beneficial to battery performance.

In short, energy storage challenges exist in the transportation industry, such as electric vehicles (EVs), and in next-generation consumer electronics, such as flexible devices for communication and healthcare. Meeting these challenges depends on developing low-cost, high-performance rechargeable batteries. This thesis is thereby motivated by the desire to develop high-performance materials and fabrication methods for advancement of flexible, rechargeable, high-energy-density PEMZAB. The central focuses of this thesis work include rational nanostructured catalyst and polymeric electrolyte design/synthesis, characterizations, and their device integration.

1.2 Background and fundamentals of zinc-air batteries

Primary zinc-air batteries are most notable for being the predominant energy source for hearing aids, where they provide impressive volumetric energy densities of 1300-1400 Wh L^{-1}.[17] Mechanically rechargeable and electrically rechargeable forms of the zinc-air batteries were both proposed. In mechanically recharged zinc-air batteries (also referred to as zinc-air fuel cells), the battery was charged by removing spent zinc and re-supplying a fresh zinc anode. This avoided the issues of poor zinc electrode reversibility and unstable bifunctional air electrodes. However, this concept was never widely adopted due to the high costs of setting up a network of zinc recharging and supplying stations. The most successful electrically rechargeable zinc-air batteries employed a flowing electrolyte design, which greatly improved the durability of the zinc electrode.[18-22] However, their power performance has traditionally been a drawback due mainly to fundamental challenges in catalyzing reactions involving oxygen gas at the air electrode. Moreover, corrosion of the air electrode during the charging reaction was another critical issue, which, along with the advent of lithium-ion batteries, slowed down zinc-air battery development at the end of the 20th century.

Notwithstanding these problems, advances in materials science and nanotechnology have brought about renewed interest in electrically rechargeable zinc–air batteries in this decade. Several companies have developed unique zinc–air systems; the most prominent ones are EOS Energy Storage, Fluidic Energy, and ZincNyx Energy Solutions. EOS Energy Storage's Aurora product is a 1 MW/4 MW h zinc-air battery for utility scale grid storage, offered for as low as 160 US$ $(kW\ h)^{-1}$.[23] Fluidic Energy has partnered with Caterpillar and Indonesia's public utility to provide over 250 MW h of its zinc–air batteries to store

photovoltaic solar energy in 500 remote communities.[24] ZincNyx Energy Solutions has developed a 5 kW/40 kW h zinc-air backup system that is undergoing a field test at a subsidiary of Teck Resources.[25] The 160 US$ $(kW\ h)^{-1}$ price offered by EOS Energy Storage is remarkable given that manufacturing of rechargeable zinc–air batteries is far from mature; for comparison, average lithium-ion battery prices are not expected to approach 160 US$ $(kW\ h)^{-1}$ until at least 2025.[26] A recent economic analysis also found that zinc-air batteries were the most economically feasible battery technology for smart-grid energy storage.[27] Therefore, the combination of high energy density, low cost, safe operation, and market-ready solutions leads to the recent enthusiasm for zinc-air batteries among many other types of emerging batteries.

The zinc-air battery is typically composed of four main components: an air electrode comprising a catalyst painted gas diffusion layer (GDL), an alkaline aqueous electrolyte, a separator and a zinc electrode. A schematic of a rechargeable zinc-air battery is shown in **Figure 1-1**. During discharge, the zinc-air battery functions as a power generator through the electrochemical coupling of a zinc metal electrode with an air electrode in the presence of an alkaline electrolyte with an inexhaustible cathode reactant (oxygen) from the atmosphere. The electrons liberated at zinc travel through an external load to the air electrode, while zinc cations are produced at the zinc electrode. At the same time, atmospheric oxygen diffuses into the porous air electrode and is ready to be reduced to hydroxide ions via the oxygen reduction reaction (ORR) (forward **Equation 1**) at a three-phase reaction site, which is the interface of oxygen (gas), electrolyte (liquid), and electrocatalysts (solid). The generated hydroxide ions then migrate from the reaction site to the zinc electrode, forming zincate ($Zn(OH)_4^{2-}$) ions, which then further decompose to insoluble zinc oxide (ZnO) at supersaturated $Zn(OH)_4^{2-}$

concentrations. **Equation 2** shows the zinc redox reaction. During charging, the zinc-air battery is capable of storing electric energy through the oxygen evolution reaction (OER) (reverse of **Equation 1**), occurring at the electrode-electrolyte interface, whereas zinc is deposited at the cathode surface (reverse of **Equation 2**). The overall reaction (**Equation 3**) can be simply shown as Zn combining with O_2 to form ZnO. Thermodynamically, both reactions are spontaneous and produce a theoretical potential of 1.66 V. However, the redox reactions of oxygen during charging and discharging cycles are kinetically slow; thus bifunctional oxygen electrocatalysts are often used to accelerate these processes.

The air electrode reaction:

$$O_2(g) + 2H_2O(l) + 4e^- \rightleftharpoons 4OH^-(aq), \quad E_0 = 0.40\ V \text{ vs. standard hydrogen electrode (SHE)} \quad (1)$$

The zinc electrode reaction:

$$\mathrm{Zn(c) + 2OH^-(aq) \rightleftharpoons ZnO(c) + H_2O(l) + 2e^-}, \quad E_0 = -1.26\ \mathrm{V\ vs.\ SHE} \quad (2)$$

The overall reaction:

$$\mathrm{2Zn(c) + O_2(g) \rightleftharpoons 2ZnO(c)}, \quad E_0 = 1.66\ \mathrm{V} \quad (3)$$

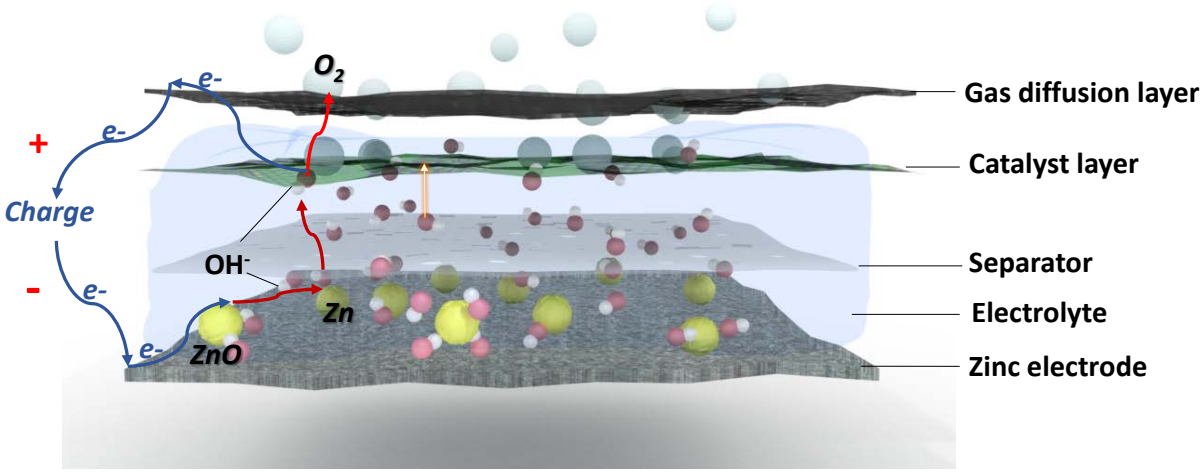

Figure 1-1. Schematic of an aqueous rechargeable zinc-air battery during charge. Reproduced from reference 4, with permission from John Wiley and Sons (2016).

1.3 Conventional planar and solid-state battery configurations

Conventional zinc-air batteries are constructed in a planar arrangement in order to maximize open air access (**Figure 1-2a**). Such design is also the most common configuration used in the aqueous-electrolyte-based zinc-air battery research, which allows quick assembly and de-assembly of the electrodes and electrolytes being investigated. Planar zinc-air batteries can either be positioned horizontally (i.e., electrode surfaces parallel to the ground) or vertically. Horizontally positioned zinc-air batteries, with the air electrode facing upward, are claimed to offer better current distribution in the zinc electrode and easier oxygen removal from the air electrode during charging.[28] However, substantial loss of the aqueous electrolyte due to evaporation could lead to a complete loss of ionic connectivity between the zinc electrode and air electrode in a horizontal configuration; therefore, most research groups employ a vertical configuration in their investigations.[29-31] Electrically rechargeable zinc–air batteries with a conventional planar configuration have not yet penetrated the commercial market. However, they are good candidates for EVs and other energy-storage applications requiring low weights and volumes due to their simple design, which prioritizes a high energy density.

Solid-state batteries have become a major area of research due to development of a wide variety of flexible electronics over the past 15 years.[32, 33] Zinc-air batteries are an excellent candidate to be designed into flexible power sources due to their low cost, high energy density and inherent safety, the latter of which negates the requirement for a rigid protective casing. Since zinc-air batteries are open to the air, it is not desirable to use aqueous electrolytes which can evaporate or leak onto sensitive electronic equipment. Therefore, to build fully flexible and robust devices, a solid-state electrolyte that is mechanically flexible and durable while

maintaining sufficient ionic conductivity is needed. Moreover, compatible and flexible electrodes and current collectors/conductive substrates must also withstand and maintain operation at a high degree of bending.[34-37] Flexible, three-dimensional (3D) electrodes based on carbon nanotubes/nanofibers and graphene materials have been reported for applications in flexible lithium-ion batteries and supercapacitors.[38-44] Fabrication methods of these 3D electrodes include *in-situ* hydrothermal method, electrodeposition, and chemical vapor deposition.[45-48] Advantages of these 3D electrodes are their significant higher amount of active materials on a given electrode area than their planar counterparts, thus higher areal energy density.[49] In the literature, two types of flexible energy storage devices that were mostly reported are thin-film type[34-36, 41, 50, 51] and cable type.[52-55] **Figure 1-2b** shows an example of a thin-film solid-state zinc-air battery layout where the battery is formed by laminating a zinc electrode, a solid electrolyte, and an air electrode. The chemistry of the solid-state zinc-air battery is similar to that of the aqueous system, where hydroxide ions migrate between the electrodes films by diffusing through the solid electrolyte.

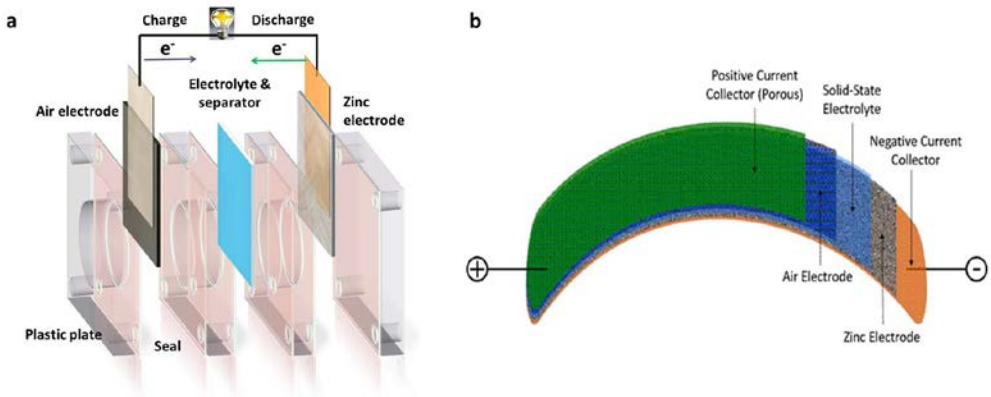

Figure 1-2. Schematic representation of (a) conventional planar and (b) flexible zinc-air battery configurations. Reproduced from reference 4, with permission from John Wiley and Sons (2016).

1.4 Polymer electrolyte

In the zinc-air battery, the electrolyte conducts hydroxide ions between the zinc and air electrodes. Up to now, aqueous alkaline electrolytes are still the most popular for zinc-air batteries, owing mainly to their superior electrode wettability and high ionic conductivities. However, in an aqueous system the performance of zinc electrode is often limited by the dendrite growth during recharge, which leads to poor cycling durability and even internal shorting of the battery. Alternatively, zinc-air batteries using solid-state alkaline electrolytes can sustain cell operation substantially longer than aqueous alkaline electrolytes, due to the low corrosion rate and low dendrite formation of the zinc electrode in a non-aqueous system.[2,56]

Polymer electrolytes, due to their solid-like nature and relatively low liquid content, enable the construction of solid-state zinc-air batteries while ensuring ion transport within the solid phase. Moreover, elastic/plastic deformation of polymeric materials is able to compensate for volume changes of the zinc electrode that occur during cycling.[57] There are commonly two approaches for designing hydroxide ion-conductive polymeric electrolytes. One way is to incorporate conducting salts (e.g., KOH, NaOH) and a large quantity of solvents into polymeric hosts (e.g., poly(vinyl alcohol), poly(ethylene oxide), poly(vinylidene fluoride)) to design alkaline gel electrolytes.[7] Another way is to immobilize functional cationic groups (e.g., quaternary ammonium cations) to the polymer backbone to design alkaline solid polymer electrolytes, where hydroxide ions are associated to each cationic group. The gel electrolyte possesses both the cohesive properties of the quasi-solid and the diffusive transport property of the liquid and thus enables a higher ionic conductivity compared to solid polymer electrolytes, but poorer mechanical strength. Such poor mechanical property will lead to poor stability at the

electrode/electrolyte interface, especially when batteries experience internal deformation (i.e., volume change of the zinc electrode upon cycling) and external deformation (e.g., bent or flexed operation).[58] To improve the mechanical robustness of the gel electrolytes, physical or chemical cross-linking processes are applied to form a more robust gel polymer network.[59] Aside from the mechanical property of the gel electrolytes, issues related to solvent exudation upon open-atmosphere conditions, as well as the weak chemical (e.g., hydrogen bonding and covalent bonding) interactions existing between the conducting salts and polymeric host materials, which lead to phase separation and/or leaching of the conducting salts and undesired side reactions with the electrodes, must be addressed.[58, 60-63] These issues would cause a dramatic decrease in the ionic conductivity and interfacial conductivity, which leads to poor cycling stability of the battery.

Compared to quasi-solid gel electrolytes, alkaline solid polymer electrolytes, also known as hydroxide ion-exchange electrolyte membranes that are often used in alkaline membrane fuel cells, do not contain additional conducting salts, and thus the likelihood of the build-up of an instable electrode/electrolyte interface during cycling can be avoided. There is a similarity between the alkaline polymer electrolytes for zinc-air batteries and those for alkaline membrane fuel cells, where the hydroxide conductivity is of highest importance. However, different from alkaline membrane fuel cells where only hydroxide-ion migration occurs between the electrodes, it has been found that in zinc-air batteries the dissolution and crossover of zinc ions from the zinc electrode to the air electrode occurs.[64] Such crossover can reduces battery capacity retention with cycling and accelerates battery aging, because the deposition of ZnO on the air electrode will passivate the active surface of the catalyst layer.[65, 66] In this case,

the selective transport of hydroxide ions in alkaline polymer electrolytes is beneficial to minimize the "cross-talk" effect of zinc ions, while allowing free movement of hydroxide ions between the electrodes. However, the room-temperature ionic conductivities of most solid polymer electrolytes (e.g., typically in the range of 10^{-4} to 10^{-5} S cm^{-1}) still remains too low for practical zinc-air battery applications.[67] To increase conductivities, several approaches for the design and optimization of the polymer matrix and structure, and the addition of inorganic nanofillers have been investigated.[68]

1.5 Bifunctional oxygen electrocatalyst

The realization of electrically rechargeable zinc-air batteries relies significantly on the air electrode that consumes oxygen during battery discharge and reversely evolves oxygen while charging. However, the kinetics for both oxygen reduction reaction (ORR) and oxygen evolution reaction (OER) are slow, and thereby the performance significantly relies on a truly bifunctional electrocatalyst to efficiently promote both the ORR and OER processes. The bifunctional catalyst materials must also be stable with respect to highly oxidative conditions upon oxygen evolution as well as strong reducing conditions under oxygen reduction at high current rates and a wide working range of potentials, spanning from about 0.6 V (versus reversible hydrogen electrode RHE, pH=14) during discharge to about 2.0 V during charge. The use of decoupled air electrodes for respective ORR and OER has been reported to improve battery cycling stability, but this configuration unavoidably complicates the cell design and incurs weight and volume penalties on power and energy density.[69] Typically, the bifunctional air electrode consists of a hydrophobic GDL and a moderately hydrophilic catalyst layer. The GDL provides a physical and conductive support for the catalysts, as well as a passage for

oxygen diffusion in and out during discharging and charging, respectively. The ORR occurs at a three-phase interface (gaseous oxygen-liquid electrolyte-solid catalyst), while the OER takes place at a two-phase reaction zone (liquid electrolyte-solid catalyst).

Platinum (Pt) exhibits a superior activity for the ORR but rather poor performance for the OER due to the formation of a stable oxide layer with low electrical conductivity.[70] Noble metal oxides such as Ruthenium (Ru)- and Iridium (Ir)-oxides, though being excellent OER catalysts are less active for the ORR.[71] In particular, the durability of existing noble metal-based catalysts is still far from being satisfied under rechargeable zinc-air battery operation; their implementation in the zinc-air system is also plagued by the scarcity and resultant high cost of noble metals.[71-74] To be commercially viable, while achieving catalytic efficiency for both the ORR and OER at the same air electrode, bifunctional catalysts free of precious metals have been extensively sought for practical zinc-air batteries.[31, 75-81] However, it is still quite challenging to find a stable catalyst material without significantly sacrificing bifunctional catalytic efficiency, due mainly to the wide operating range of the ORR/OER potential during the discharge and charge process.

Significant progress has been made in bifunctional catalyst development including transition metal-based materials (oxides, chalcogenides, nitrides and carbides), heteroatom-doped carbon nanomaterials, and hybrid materials which consist of the former two.[82] Despite the progress, most catalyst research is still generally based on the trial-and-error method. This is because the mechanism and reaction kinetics of the ORR and OER varies between different catalyst materials and electrolytes, and thus is hard to predict.[83-85] In terms of ORR, the

reduction of oxygen in aqueous electrolytes may proceed by two overall pathways: a direct four-electron pathway (**Equation 4**) or a two-electron pathway (**Equation 5**).

$$O_2 + 2H_2O + 4e^- \rightleftharpoons 4OH^- \quad (4)$$

$$O_2 + H_2O + 2e^- \rightleftharpoons HO_2^- + OH^- \quad (5)$$

For practical battery applications, catalysts that can promote ORR through the direct four-electron reduction pathway are highly preferred.[85] This is because oxygen in this pathway is reduced to OH^- without producing peroxide in the solution phase. These catalysts are often noble-metal (e.g. Pt, Pd, Ag)-based materials,[86, 87] some transition metal macrocycles (e.g. iron phthalocyanine),[88, 89] metal oxides (e.g. perovskites),[90, 91] and some nitrogen-doped carbon materials.[79, 92, 93] In contrast, the two-electron reduction path involves peroxide species that are present in the electrolyte. The peroxide build up not only reduces the efficiency of the ORR catalysis but also poisons the catalysts or carbon support materials because of its high oxidizability.[84]

Precise reaction pathways during OER are relatively ambiguous and thus difficult to be determined. Generally accepted mechanisms for metal-catalyzed OER involve the reverse process of ORR through four sequential electron transfer steps.[86, 94] Noble metal oxides (e.g. IrO_2 and RuO_2) are highly OER active and display metallic-like conductivity, but are fairly expensive.[95] The drive to replace these expensive noble metal oxides has led to a class of catalysts consisting of earth-abundant transition metal (e.g. Co, Ni and Mn) oxides and (oxy)hydroxides.[48] Some transition metal oxides, exhibiting semiconducting properties, demonstrate good oxygen evolution performance.[96] This is particularly the case with spinel- and perovskite-type metal oxides, such as cobalt oxide,[97-100] nickel cobalt oxide[101-103] and

lanthanum nickel oxide.[104-106] In these materials, surface metal cations (M) are considered as the active sites for OER, where the reaction proceeds via a series of metal-stabilized intermediates (i.e. M-OH, M-O, M-OOH, M-OO) and changes the oxidation state of metal cations accordingly.[71] The relative stabilities of these intermediates at metallic surfaces, namely, the binding strength of M-O bonds and the activation barriers between intermediates, determine the rate-determining step and therefore the overall OER rates.[71] A thorough understanding of the rate-determining steps could provide insight into how compositional, structural, geometric, and electronic properties of catalysts could be tuned to enhance the reaction rates of OER. A number of activity trends have been presented computationally and experimentally, in which OER activities are relative to the number of *d*-electrons in the e_g orbital of the metal cations.[48] These trends are complex due to many factors, including electronic structure, electrochemically active surface area, surface composition and stoichiometry, electrical conductivity and geometric structure (strain).[48]

Although recent advances in the computational analysis of catalysis enable us to predict and select potential candidates for ORR and OER, there is currently no exemplary benchmark performance for bifunctional catalysts to which all newly developed catalysts can be compared.[107] State-of-the-art carbon-supported Pt (i.e. Pt/C) and RuO_2 or IrO_2 (i.e. RuO_2/C or IrO_2/C) catalysts are currently the most accepted benchmark electrocatalyst materials for the ORR and OER, respectively.[82] A common approach to obtain high-performance bifunctional catalysts is to physically combine the above ORR catalysts (e.g. Pt/C) with efficient OER catalysts (e.g. IrO_2/C). Such approach, however, is often neither effective nor reliable due to poor material compatibility of these composite catalysts. It is thus challenging, but desirable, to

find a general principle to achieve rational designs of bifunctional catalysts, yielding a strong bifunctional capability and high stability for the sake of long-term zinc-air battery rechargeability.

1.6 Gas diffusion layer

The gas diffusion layer (GDL) plays a vital role in the performance of bifunctional air electrodes. For zinc-air batteries, the GDL has the following essential functions: i) provides a physical support for the catalysts/catalyst layer, ii) allows uniformly distributed air (oxygen) transportation to/from the catalysts, iii) serves as a wet-proofing electrode backing that prevents electrolyte from leaking out, and iv) possesses high electrical conductivity to provide an electrically conductive pathway for current collection. To facilitate air transport in zinc-air batteries, the GDL should be thin, highly porous, and hydrophobic in nature. The hydrophobicity can be realized by impregnating the GDL with hydrophobic agents such as polytetrafluoroethylene (PTFE),[108, 109] polyvinylidene fluoride (PVDF),[110, 111] and fluorinated ethylene propylene (FEP).[112, 113] The degree of GDL hydrophobicity influences battery polarization behavior in terms of electrical conductivity (ohmic resistance) and gas permeability (mass transfer). To achieve optimal performance, a GDL should possess the capability of alleviating electrolyte evaporation and resisting electrolyte flooding under extreme conditions.[114] Moreover, an ideal GDL should have properties such as fast air diffusion with high electrolyte repellency, high mechanical integrity (with optimum bending stiffness in the case of flexible designs), superior electrical conductivity, and reliable electrochemical-oxidation stability and chemical durability in strong alkaline electrolytes.

Two types of commercially-available carbon-based GDLs that are commonly used in

zinc-air batteries are non-woven carbon paper (e.g. Toray, Freudenber, Sigracet) and woven carbon cloth (e.g. Zoltek, GDL-CT, ELATTM). These carbon-based GDLs typically have a dual-layer design, consisting of a macroporous gas diffusion backing and a thin microporous layer (MPL) (**Figure 1-3a**). The macroporous backing layer is made up of a highly hydrophobic array of graphitized carbon fibers to provide large gas diffusion pores, while the MPL is a thin, relatively hydrophilic carbon (e.g. carbon black) layer having fine porosity for supporting the catalytic active materials. The MPL helps to distribute air effectively throughout the catalyst layer and minimize the contact resistance between the macroporous layer and catalyst layer.[115] Thinner carbon paper GDLs tend to result in a better battery performance, in terms of more favorable ohmic resistance and mass transfer; but they are quite brittle to handle. On the other hand, thicker carbon cloth GDLs are more mechanically flexible, and thereby can be employed as a robust catalyst layer support of small-scale, flexible zinc-air battery applications. Although these state-of-the-art carbon-based GDLs have been successfully demonstrated in polymer electrolyte membrane fuel cells, their stability towards high oxidation potentials during oxygen evolution (charging) as well as exposure to highly alkaline electrolytes is still an issue. These GDLs are highly susceptible to carbon corrosion, which consequently results in losses of active surface area for electrochemical oxygen reactions, heterogeneous distribution of current throughout the air electrodes, and even severe leakage of electrolytes.[16, 116] It is possible that alkaline electrolytes also can be negatively influenced by dissolved carbonate species resulting from carbon corrosion of the GDLs. For long-term operation, it is thus of utmost importance to prevent GDL corrosion either by the use of highly corrosion-resistant, graphitized carbon materials or by the use of metallic substrates.

Typically, metal-based GDLs are fabricated by casting and pressing a mixture of catalyst, metal powders, and PTFE binder into a porous metallic substrate such as metal foam (**Figure 1-3b**). In general, metal-based GDLs provide a higher electrical conductivity and a better electrochemically oxidative stability (either through a higher reduction potential or surface passivation via formation of a thin oxide/hydroxide layer) over a wider potential range compared to carbon-based GDLs.[117] Metal substrates made of stainless steel mesh, titanium mesh, nickel mesh and nickel/copper foam have been employed as diffusion media and led to comparable performance as carbon-based GDLs in zinc-air batteries.[29, 118-123] Chen *et al.*[117] reported on an integrative air electrode wherein the GDL and catalyst layer were combined in a single layer. The single layer design with different porosity and hydrophobicity made from sintered nickel powder as a base and Co_3O_4 as a bifunctional catalyst was demonstrated in zinc-air batteries. The electrode was fabricated by casting and pressing a mixture of Co_3O_4 catalyst, nickel macroparticles, and PTFE binder into a conductive nickel foam substrate, with a thickness of 150-250 μm. The nickel macroparticles were used to provide a macroporous structure in the single layer, allowing for efficient air diffusion to the active catalysts. In addition, the use of nickel macroparticles and nickel foam instead of carbon materials to form a hierarchical porous framework for air diffusion avoided the issue of carbon corrosion and subsequent mechanical failure and electrolyte leakage. Using this air electrode in zinc-air batteries led to a stable cycling performance of more than 100 cycles at a current rate of 17.6 mA cm^{-2}. Similarly, the active catalysts can be directly sintered on the corrosion-resistant, porous metallic substrate. Brost *et al.*[124] prepared a bifunctional air electrode consisting of nickel foam scaffold with perovskite $La_{0.6}Ca_{0.4}CoO_3$ catalysts chemically bonded to the

conductive scaffold by high-temperature thermal treatment. The porosity of the scaffold was controlled (~80%) to facilitate the flow of air through the electrode. In this electrode, conductive additives such as metal fibers or particles were also used to provide additional current pathways between the catalysts and nickel foam scaffold. This significantly improves the catalytic performance of the active catalyst and efficiency of the batteries due to an increase of surface area and electrical conductivity. It is worth mentioning that the use of plastic binders (e.g. PTFE) is unavoidable in both the cases of carbon- and metal-based GDLs. PTFE is gradually attacked by caustic and oxidizing conditions and consequently degraded over long operation times, resulting in collapse of the porous structure and mechanical failure of the GDLs. Both effects lead not only to the increase of mass transfer resistance at the air electrodes, but also to apparent reduction of long-term battery operation. In regard to the degradation of PTFE, making the distribution of the micropores in the GDLs more uniform can alleviate the negative influence of the porous geometry change.[116]

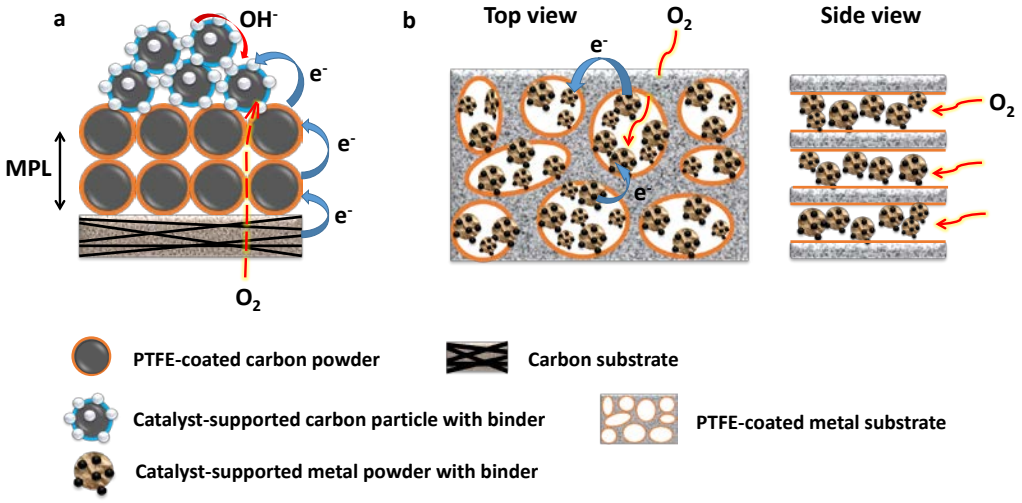

Figure 1-3. Schematic diagram of (a) carbon-based (cross-sectional view), and (b) metal-based GDLs integrated with catalyst. Reproduced from reference 4, with permission from John Wiley and Sons (2016).

1.7 Air electrode integration

Despite all the progress of bifunctional oxygen electrocatalysts, their practical performance in zinc-air batteries suffers from poor integration in the air electrode.[125] That is, there are physical limits to how much catalyst can be deposited on a given air electrode surface without inhibiting charge and mass transport processes. Typically, the fabrication of the bifunctional air electrode involves physical incorporation of the bifunctional catalyst and ancillary additives into the GDL framework, through a variety of methods such as drop-casting, screen-printing, and spray-coating. The ancillary materials are required in these approaches to construct a continuous, porous, and ionic/electrical conductive network in the air electrode, for the sake of electron and charge transfer as well as mass diffusion. They generally include polymeric binders (e.g. Nafion® perfluorinated, Tokuyama AS4 alkaline ionomers) and a conductive catalyst support (e.g. acetylene black). However, the use of these ancillary materials has negative impact on the battery performance. For instance, acetylene black is readily corroded, especially when encountering highly-oxidative electrochemical potentials during charging. The carbon corrosion aggravates aggregation/sintering or even leaching of catalyst, severely reducing overall battery performance. Another issue is associated with detachment of weakly bound catalyst from the electrode surface due to degradation of polymeric binders in the strong caustic and oxidizing environment.[125] This issue results in losses of active materials and large interfacial impedance, giving rise to high overpotentials for discharging and charging reactions. Thus, there exists a need for a novel integrative design of the bifunctional-air electrode for rechargeable zinc-air batteries that overcomes the aforementioned deficiencies. Approaches such as electrodeposition, hydrothermal treatment and chemical vapor deposition

(CVD) were adopted to directly grow nanostructured catalysts on conductive and porous substrates, in order to make carbon-support-free and binder-free bifunctional air electrodes.[16, 80, 125-130] Without additional carbon supports and binders, these advanced air electrodes also can provide a high accessibility of the catalytic sites and a low interfacial contact resistance. Additionally, such integrative bifunctional air electrodes as a whole are directly synthesized with the current collector (conductive substrates), and are free of the conventional complex preparation processes, which would be of great benefit to large-scale fabrication. To realize flexible integrative air electrodes, physically-robust or bendable substrates (e.g. carbon cloth or metal meshes/foams) are strongly demanded. **Table 1-1** presents a summary of some of the recently reported integrative bifunctional air electrode designs for rechargeable zinc-air batteries. To access the overall air-electrode performance, the voltage gap between the discharge and charge, the power density, and the cycle stability are compared.

Table 1-1. Summary of recently reported binder-free, assembly of bifunctional oxygen electrocatalysts. Reproduced from reference 4, with permission from John Wiley and Sons (2016).

Reference	Bifunctional air electrode	Synthesis method	Feature	Cell configuration	Power density & durability
16	Co_3O_4 on stainless steel	Hydrothermal	Flexible	Zinc plate/6M KOH+0.2 M zinc acetate/air	40 mW cm^{-2} @65mA cm^{-2}; ~600 h @ 50 mA for 6 h per cycle
126	RuO_2 on CNT	Dip coating	Flexible	Zinc wire/gelled PVA&PEO alkaline electrolyte/air	NA; ~30 h @ 1 A g^{-1} for 1 h per cycle

127	AgCu on nickel foam	Pulsed laser deposition	Rigid	Zinc plate/6M KOH+0.1 M zinc acetate/air	86.3 mW cm^{-2} @100 mA cm^{-2}; ~50 h @ 20 mA cm^{-2} for 15 min per cycle
129	Co_4N/intertwined carbon fibers on carbon cloth	Electrodeposition/ carbonization	Flexible	Zinc plate/6M KOH /air	174 mW cm^{-2} @260 mA cm^{-2}; ~136 h @ 10 mA cm^{-2} for 30 min per cycle
130	a-MnO_2 on carbon paper	Immersion process	Rigid	Zinc plate/6M KOH+20 g L^{-1} $ZnCl_2$/air	108 mW cm^{-2} @168 mA cm^{-2}; ~125 h @ 15 mA cm^{-2} for 10 min-4 h per cycle
131	Co_3O_4 on carbon nanofiber mat	Electrospinning/ pyrolysis	Rigid	Zinc plate/6M KOH+0.2 M $ZnCl_2$/air	125 mW cm^{-2} @200 mA cm^{-2}; ~55 h @ 20 mA cm^{-2} for 1 h per cycle

1.8 Structure of thesis

The main objectives are to i) design high-performance materials for rechargeable PEMZABs, ii) understand how functional and nanostructured materials influence the properties and electrochemical performance of batteries, and iii) contribute to an innovative solution for the development of next-generation rechargeable zinc-air battery technologies. Therefore, in this thesis work, the design and characterization of different types of polymer electrolytes and bifunctional oxygen electrocatalysts were investigated; their relevant physicochemical and electrochemical properties were optimized, respectively, then combined to fabricate rechargeable PEMZABs. **Figure 1-4** depicts a breakdown of work conducted throughout this thesis.

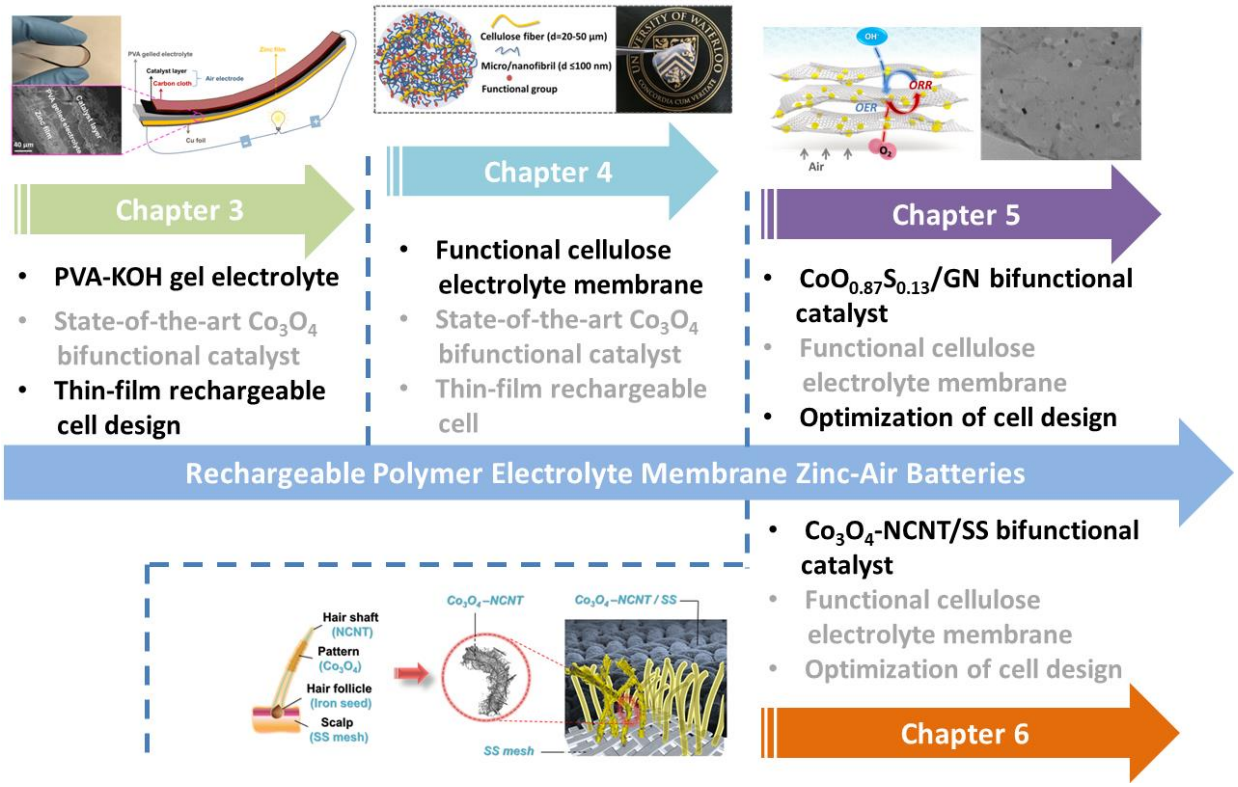

Figure 1-4. Schematic illustration of the research topics throughout this thesis.

This thesis is organized in seven chapters. **Chapter 1** introduces the reader to a general background, motivation, current research progress of zinc-air batteries, and scope of the thesis work. **Chapter 2** presents some key performance measurement techniques used throughout the thesis, with in depth details provided within subsequent Chapters 3 through 6. Four different tasks that have been published are discussed in subsequent Chapters 3-6. **Chapter 3** introduces a proof-of-concept of a film-shaped, rechargeable PEMZAB as a high-energy-density power source for flexible and wearable electronics. **Chapter 4** focuses on the improvement of the polymeric electrolyte, and in particular the synthesis of a highly flexible and hydroxide conductive electrolyte membrane through functionalization of natural cellulose nanofibers. The performance capabilities of the developed electrolyte membrane in the flexible zinc-air battery

are elucidated. **Chapter 5** describes an effort to further improve the battery performance by designing an efficient hybrid bifunctional oxygen electrocatalyst. This hybrid catalyst consists of cobalt oxysulfide nanoparticles and nitrogen-doped graphene nanomeshes ($CoO_{0.87}S_{0.13}$/GN), which have demonstrated electrocatalytic improvements over the existing benchmark catalysts. In addition to the catalyst development, **Chapter 6** highlights the development of a 3D nanostructured assembly of the catalyst/current collector that morphologically emulates a human hair array. Such a design consists of a nanoassembly involving two-dimensional mesoporous Co_3O_4 nanopetals in one-dimensional nitrogen-doped multi-walled carbon nanotubes supported vertically on a flexible stainless-steel mesh. This 3D assembly provides several performance-related advantages over the conventional planar air electrodes. Finally, **Chapter 7** summarizes the important results and some discussion on the future direction that the work may take.

Chapter 2 Key performance measurement techniques

2.1 Overview

In this work, the polymer electrolytes described in Chapters 3 and 4 were fabricated via solution-casting and vacuum-filtration techniques. The bifunctional oxygen catalysts described in Chapters 5 and 6 were synthesized in different ways, including the solvothermal method, high-temperature pyrolysis, chemical vapor deposition, and electrodeposition. The detailed experimental procedures, characterization and evaluation of each developed material are provided within the proceeding chapters. This chapter presents some key performance measurement techniques related to the evaluation of polymer electrolyte membranes, bifunctional electrocatalysts, and zinc-air batteries.

2.2 Four-probe alternating current impedance technique

A four-probe alternating current impedance technique can be used to measure the ionic conductivity of an electrolyte membrane.[132] A fully hydrated membrane was sandwiched in a Teflon^{TM} conductivity cell (**Figure 2-1a**) equipped with four Pt electrodes (wires). The four Pt electrodes are the working electrode (WE), the counter electrode (CE), and two reference electrodes (RE), as shown in **Figure 2-1b**. The four-probe conductivity cell can monitor the potential drop across the membrane by using an alternating current impedance technique, where the alternating current frequency was scanned from 100 kHz to 0.1 Hz at a voltage amplitude of 100 mV. The ohimic resistance (R_s) of the membrane can be determined from the Nyquist impedance plot (Figure 2-1b). The semicircular arc is related to the capacitive impedance (C

and R_i) of the electrode-membrane interface. The hydroxide conductivity at controlled humidity and temperature can be calculated using the equation (**Equation 6**).

$$\sigma = {}^{L}/_{RA} \qquad (6)$$

where σ is the ionic conductivity, L is the distance between two reference electrodes, R_s is the ohmic resistance of the electrolyte membrane, and A is the cross-sectional area of the membrane. Furthermore, the hydroxide conduction behavior of the membrane can be elucidated by the relationship between the conductivity and the temperature derived from the Arrhenius equation (**Equation 7**).

$$ln\sigma = ln\sigma_0 - \frac{E_a}{RT} \qquad (7)$$

where E_a is the apparent activation energy for hydroxide conduction , R is the gas constant, T is the absolute temperature, and is σ_0 the frequency factor.

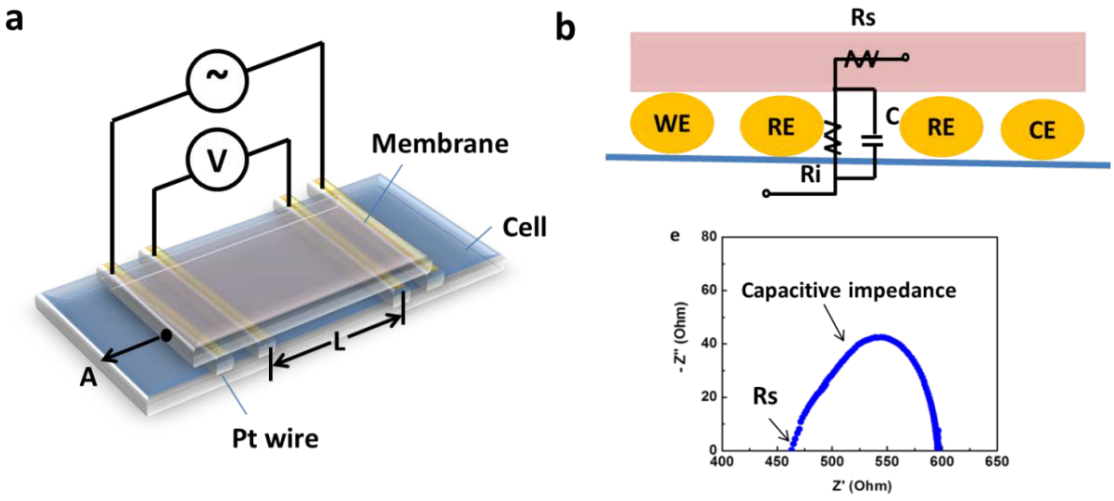

Figure 2-1. a) Schematic of a four-probe conductivity cell. b) The equivalent circuit for the impedance of an electrolyte membrane with the corresponding Nyquist plot.

2.3 Rotating disc voltammetry

Rotating disc voltammetry is a well-established technique to provide quantitative information on electrochemical reaction kinetics of catalyst materials, by taking advantage of the steady-state laminar flow conditions during rotating. The electrochemical measurements are conducted in a three-electrode electrochemical cell (**Figure 2-2a**), comprising a working electrode, a reference electrode, a counter electrode and an aqueous electrolyte (e.g., 0.1 M KOH solution throughout this study). The cell potential can be measured across the reference and working electrodes with negligible current, while the cell current is controlled across the counter and working electrodes. The working electrode is typically a glassy carbon disc electrode, on which the catalyst materials are deposited (**Figure 2-2b**); this electrode can be rotated to mitigate mass transport losses, which allows to measure the electrode reaction kinetics. The counter electrode is generally a graphite rod for non-platinum catalyst system, and the reference electrode used in this study was a reversible hydrogen electrode (RHE).

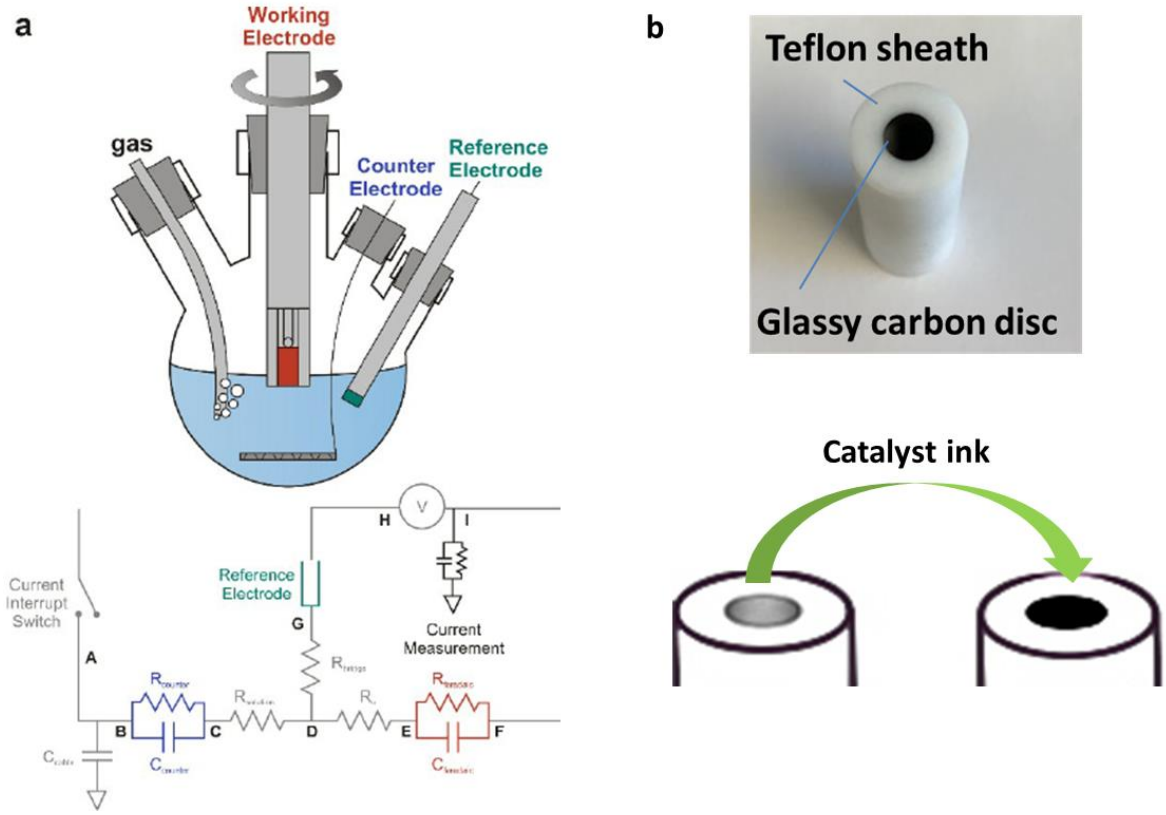

Figure 2-2. a) Schematic of a typical three-electrode electrochemical cell, reprinted from 133, with permission from the Royal Society of Chemistry. b) Glassy carbon disc electrode on which the catalyst material is deposited.

In this work, the catalyst's activity with respect to both the oxygen reduction (ORR) and oxygen evolution (OER) are investigated by using cyclic voltammetry (CV) and linear sweep voltammetry (LSV) methods. LSV refers to a method where the electrode potential is swept from an initial value to a final value at a constant scanning rate and a certain rotation speed, while CV involves sweeping repeatedly the electrode potential back-and-forth between two extremes. In a typical measurement of the ORR activity, the electrode potential is swept from 1.0 to 0.1 V vs. RHE with a scan rate of 5 mV s^{-1} while measuring the cell current in an oxygen-saturated 0.1 M KOH solution at a certain rotation speed (e.g., 1600 rpm). During this

linear sweep voltammetry experiment, current versus potential data is plotted, as shown in **Figure 2-3a** (blue curve). The observed current is the result of electrons flowing into the electrode, and is controlled by mass transport. At a rotating electrode, the impact of mass transport (i.e. limiting current) on the ORR kinetics can be determined by the Levich equation.[133] However, the Levich equation only applies to the limiting current, which is not the case in a half-reaction limited by a combination of sluggish kinetics and mass transport; in this case, it is possible to use an alternative the Koutecky-Levich equation to elucidate both the kinetic and mass-transport parameters. The general approach is to measure a set of voltammograms at different rotation speeds (i.e. conduct a Levich study, the inset of **Figure 2-3b**), and then plot the reciprocal current based on a Koutecky-Levich study (**Figure 2-3b**). The linear portion of the data on a Koutecky-Levich plot is based on the Koutecky-Levich equation shown as follows (**Equation 3**):

$$\frac{1}{i} = \frac{1}{i_k} + \left(\frac{1}{0.620nFAD^{2/3}\nu^{-1/6}C}\right)\omega^{-1/2} \qquad (3)$$

where i is the disc current density, i_k is the kinetic current density, n is the overall electron transfer number, F is the Faraday constant (96 485 C mol^{-1}), A is the electrode surface area (cm^2), D is the oxygen diffusion coefficient (1.9 x 10^{-5} cm^2 s^{-1}) in 0.1 M KOH, ν is the kinematic viscosity of in 0.1 M KOH solution (0.01 cm^2 s^{-1}), C is the concentration of dissolved oxygen (1.1 x 10^{-6} mol cm^{-3}) in 0.1 M KOH, and ω is the angular rate of rotation (rad s^{-1}).

In a typical measurement of the OER activity, the electrode potential is swept from 1.0 to 1.8 V vs. RHE with a scan rate of 5 mV s^{-1}, while measuring the cell current under a nitrogen-saturated 0.1 M KOH solution. The rotation speed should be sufficiently fast (e.g.,

1600 rpm) to aid in oxygen removal during OER at the electrode surface. An example rotating disc voltammogram of Co_3O_4 nanoparticles in 0.1 M KOH solution is shown in **Figure 2-3a** (red curve). An efficient bifunctional electrocatalyst should minimize the overpotential for both the ORR and OER, allowing for an ideal reversible oxygen electrode.

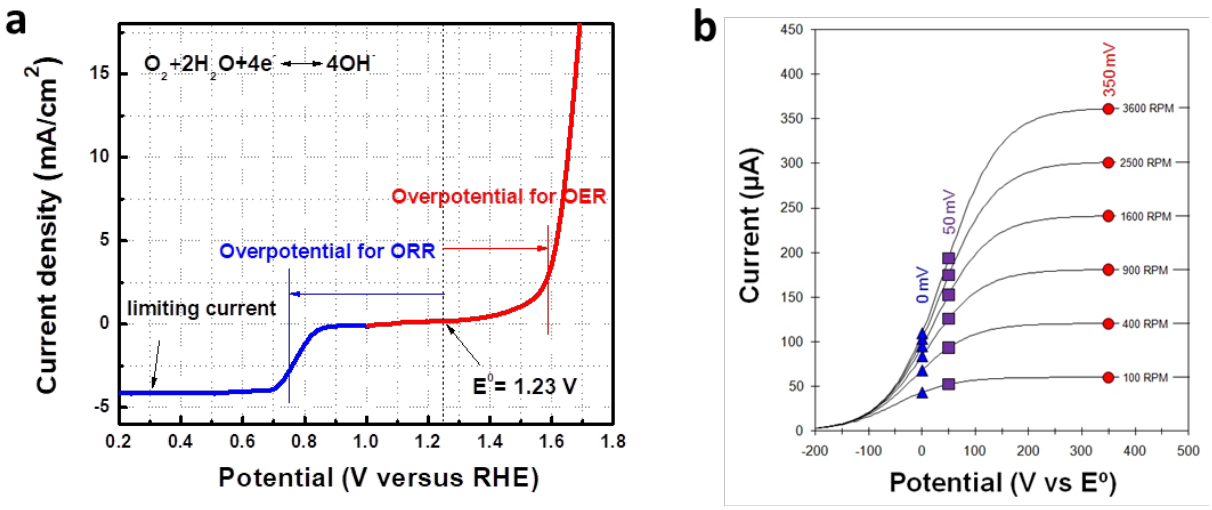

Figure 2-3. a) Linear sweep voltammetry for the ORR and OER in 0.1 M KOH solution by Co_3O_4 nanoparticles. b) Koutecky-Levich plot with a set of voltammograms at different rotation rates, reprinted from reference 134.

2.4 Battery performance evaluation

This section provides an overview of the variety of experimental testing techniques that may be used to evaluate the performance of zinc-air batteries. Factors such as open-circuit voltage (OCV), operating voltage, energy efficiency, specific capacity, energy density, power density, and cyclic stability are essential parameters that should be evaluated in the investigation of novel solid-state zinc-air batteries. These parameters can be revealed with galvanodynamic polarization and galvanostatic techniques. In addition, individual resistance,

capacitance, and electrode polarization values can aid in the understanding of electrolyte-electrode interfacial behavior by using electrochemical impedance spectroscopy.

2.4.1 Galvanodynamic polarization

The galvanodynamic polarization technique is used to evaluate the degree of departure of a battery's operating voltage from its OCV in response to discharging and charging currents. The technique is generally carried out by applying negative (discharging) or positive (charging) currents with progressively higher magnitudes to the battery electrodes. The potential responses are recorded as a function of current, yielding discharge and charge polarization curves. **Figure 2-4** shows a typical example of discharge and charge polarization plots (black and brown solid lines, respectively) of a rechargeable zinc–air battery obtained by the galvanodynamic polarization method. The difference between the operating voltage and the OCV (i.e., discharge or charge overpotential) directly represents the sum of the voltage losses associated with activation and mass-transfer polarization at each electrode, in addition to the ohmic resistance of every component of the electrochemical circuit. Taking the discharge polarization curve as an example, the steep initial voltage drop is mostly caused by the energy barrier for the electron-transfer reactions occurring at the electrodes (referred to as activation polarization). The oxygen reactions at the air electrode constitute the majority of activation losses in zinc-air batteries. When the current is further increased, additional voltage losses are dominated by ohmic polarization, and thus the voltage decreases almost linearly with the current density. In this ohmic region, the voltage loss mostly comes from the internal resistance of the electrolyte to ionic flow and the interfacial resistances between the electrodes and the electrolyte; this is the desirable operating regime for the zinc-air battery. Both the activation (influenced mainly

by catalyst activity) and ohmic resistances (influenced mainly by the electrolyte properties) are key power performance drivers of zinc-air batteries. The sharp voltage drop at the end is associated with the limited mass transfer of reactants (i.e., oxygen or OH^-) to the electrodes, referred to as mass-transfer polarization. The power density (blue solid line) of the zinc-air battery can be plotted as a function of current density by multiplying the discharge voltage by the applied current density, allowing determination of the peak power density (and corresponding current density). In addition, the zinc-air battery's energy efficiency (red solid line) can also be determined at a certain current density by simply dividing the discharge voltage by the charge voltage. In this example, at the peak power output, the battery energy efficiency is 31.5%, indicating that almost 70% of the energy put into the battery is lost to the discharge and charge overpotentials (this assumes the battery is charged and discharged at the same current density).

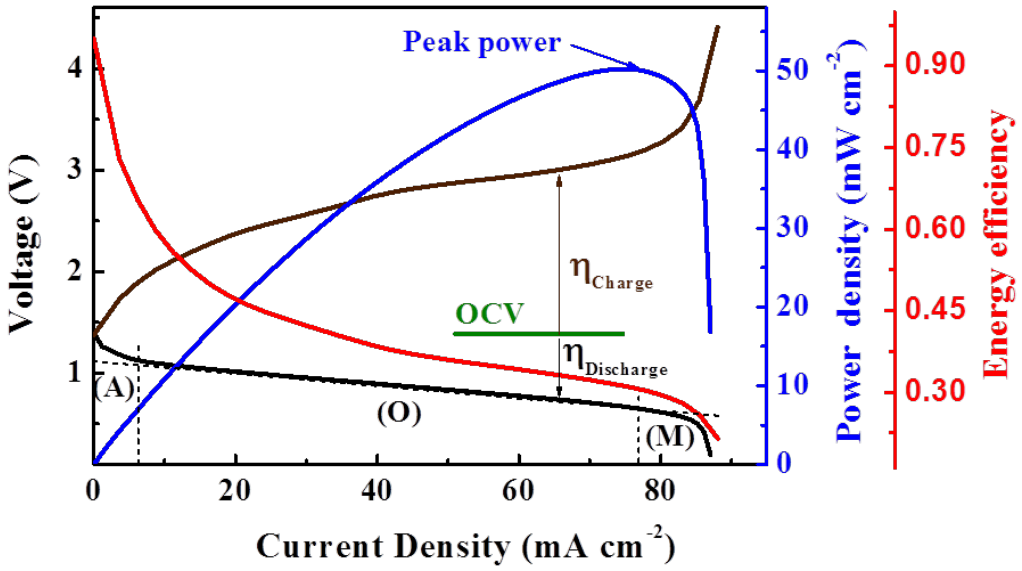

Figure 2-4. Typical discharge and charge polarization curves for the rechargeable zinc-air battery, as well as the power density and energy efficiency. The activation (A), ohmic (O) and

mass transfer (M) polariation regions are identified on the discharge curve by black dashed lines. Reproduced from reference 4, with permission from John Wiley and Sons (2016).

2.4.2 Galvanostatic full-discharge

The galvanostatic full-discharge test determines the capacity of the zinc-air battery by applying a fixed discharge current until a defined cut-off voltage is reached. Since a zinc-air battery's capacity is dictated by the zinc electrode, the capacity is often normalized by the mass of the zinc electrode or the mass of zinc within the zinc electrode; this enables a relative comparison to the theoretical specific zinc capacity of 820 mAh g^{-1}. In addition, a specific energy density normalized to the consumed mass of zinc (Wh g^{-1}) can be obtained by simply multiplying the specific capacity and an average discharge voltage over the applied discharge period. Discharge curves for a flexible zinc-air battery are shown in **Figure 2-5**. In this case, the discharge curves are extremely flat, meaning little ohmic polarization of the battery. Note that the "knee" (the sharp voltage inflection) of the voltage at the end of discharge curves indicates a full passivation of ZnO at the zinc-electrode surface. Moreover, increasing the current density in a full discharge test often results in a slightly lower attained capacity. This may be attributed to the increased rate of $Zn(OH)_4^{2-}$ ion production at the zinc-electrode surface. This results in a more severe $Zn(OH)_4^{2-}$ concentration gradient, causing earlier precipitation of ZnO at the electrode surface, and thus passivation at an earlier stage.

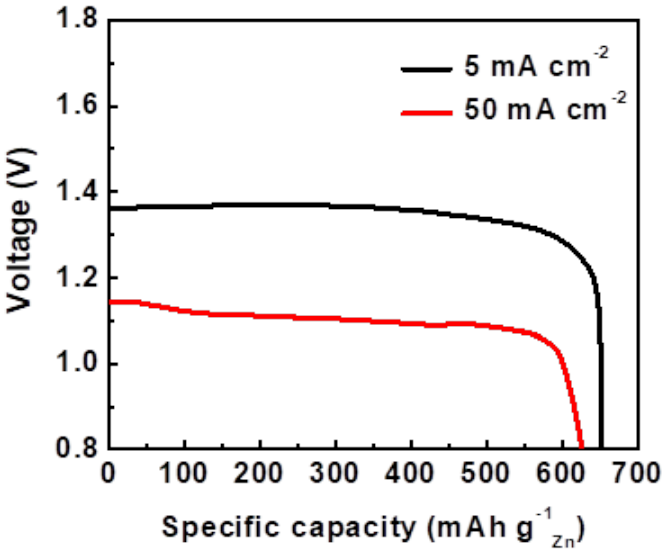

Figure 2-5. Typical specific capacity curves of the zinc-air battery under different current densities. Reproduced from reference 135, with permission from John Wiley and Sons (2016).

2.4.3 Galvanostatic cycling

Galvanostatic cycling is an accelerated testing technique for investigating the electrochemical durability of zinc-air batteries. The galvanostatic discharge/charge cycling test is performed by alternately applying fixed negative and positive currents while the corresponding discharge and charge voltages are recorded. A typical plot obtained from this test is presented in **Figure 2-6**. In comparison to galvanodynamic polarization testing, the galvanostatic cycling test involves the choice of more test conditions, including discharge/charge current density, the number of cycles, and the time length and/or cut-off voltage for each cycle; each of these parameters will affect the test results. Cycling tests for zinc-air batteries can be broadly divided into two different categories, the first of which uses a large number of cycles with short time lengths for each cycle (i.e., pulse cycling test). In this

method, the cycling durability is most likely to be limited by the air electrode, since the zinc electrode is usually only discharged to a small fraction of its total capacity in each cycle. In contrast, the second category involves a shorter number of cycles with longer time lengths. This testing method is more suitable for evaluating the real recharge capacity retention of the zinc-air battery rather than the pulse cycling method. This is because the time length of each cycle is typically long enough to utilize a significant portion of the zinc electrode's capacity. Another advantage of using longer cycling times is that more realistic voltage values are likely to be obtained, as opposed to cycling times that are too short to allow the voltages to reach a stable value. However, since the two different cycling methods provide uniquely useful information, it is recommended to conduct both types of experiments in investigations of zinc-air batteries.

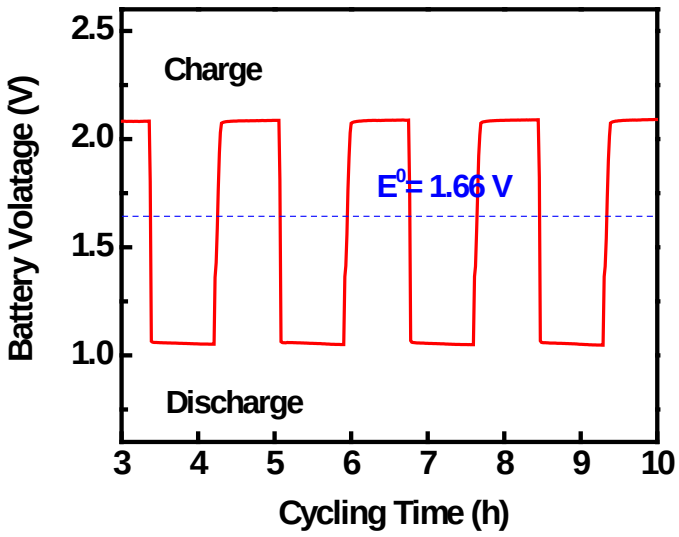

Figure 2-7. Typical galvanostatic discharge/charge battery cycling test. Commercial Co_3O_4 nanoparticles are tested. 10 mA cm^{-1} and 1h are applied as the current density and length of a cycle, respectively.

2.4.4 Electrochemical Impedance Spectroscopy

Electrochemical impedance spectroscopy (EIS) can reveal individual resistances and capacitances within a zinc-air battery, enabling a better understanding of the major limiting factors. Typically, EIS of rechargeable zinc-air batteries is conducted with respect to the discharge and recharge processes at a fixed overpotential. Typical EIS spectra (i.e., Nyquist plots) of batteries using different catalysts, as well as the corresponding equivalent circuit, are shown in **Figure 2-7**. The two semicircles in the Nyquist plot are modeled by the provided equivalent circuit including five elements: R_s, R_{int}, R_{ct}, Q_{int}, and Q_{dl}.[76] R_s and R_{int} signify the electrolyte resistance and the electrode-electrolyte interfacial resistance, respectively. R_{ct} represents the charge-transfer resistance of the air electrode during the electrochemical reaction, which is directly related to the electrocatalytic activity of the air electrode. The constant phase elements, Q_{int} and Q_{dl}, are characteristic capacitances from the interface between the electrode and electrolyte. In terms of general analysis of the results, a smaller charge-transfer resistance indicates higher ORR catalytic activities (the same trend is applied to OER activity during charging), leading to a higher discharge voltage.[136] In addition, smaller R_s and R_{int} imply lower internal resistances from the electrolyte and at the interfacial contacts, respectively, in the zinc-air battery. Interfacial resistance values are particularly important to quantify for solid-state electrolytes, due their relatively poor wetting characteristics compared to conventional aqueous electrolytes.

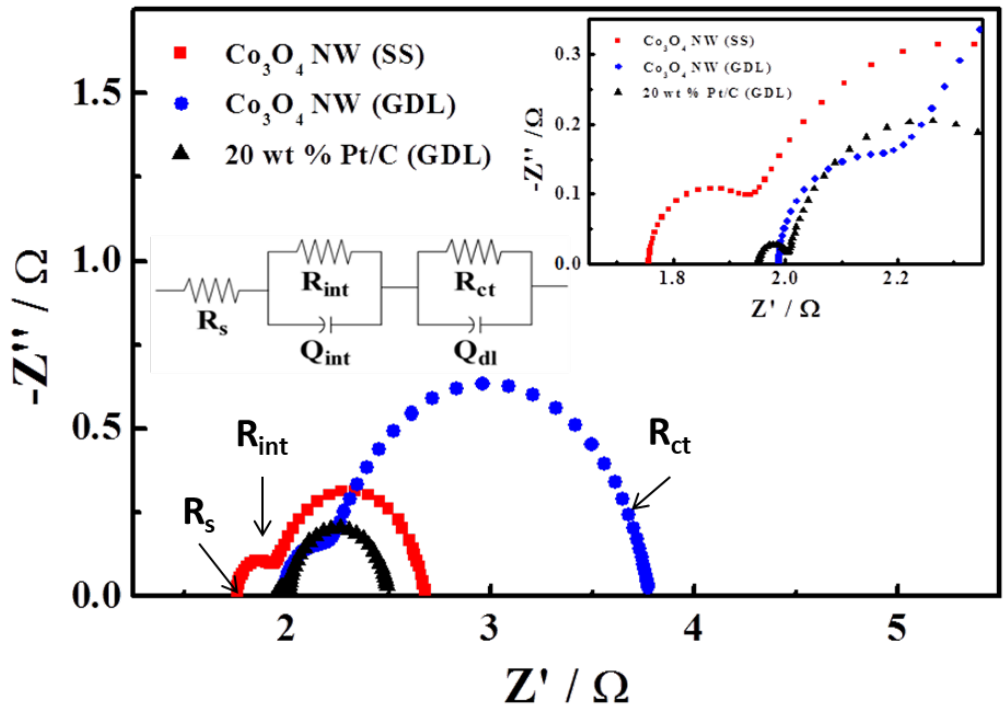

Figure 2-8. Nyquist plots obtained by EIS using air under ambient conditions of Co_3O_4 nanowires grown on stainless steel mesh (red square), Co_3O_4 nanowires sprayed on GDL (blue circle), and Pt/C sprayed on GDL (black triangle). Inset: High frequency range of the Nyquist plot, and the equivalent circuit. Reproduced from reference[137], with permission from the John Wiley and Sons.

Chapter 3 Gel polymer electrolyte-based rechargeable zinc-air batteries

3.1 Introduction

Technological improvement that enables batteries with high energy-density, flexibility and safety is being driven by an ever-increasing demand for many new applications. From portable/flexible electronics to electric vehicles, rechargeable zinc-air batteries hold great promise as environmentally-benign, reliable, and high-energy-density power sources. The majority of zinc-air battery technologies to date have utilized aqueous alkaline electrolytes, which are not suitable for integrating into flexible devices.[4] In order to realize their flexible applications, transitioning from aqueous electrolytes to shape-conformable polymeric electrolytes is of primary importance. Polymeric electrolytes can function as both aqueous electrolytes, providing ion conduction, and as separators preventing battery internal short-circuits, thus greatly simplifying the design and fabrication process of batteries.

This chapter investigates the design of a quasi-solid-state rechargeable zinc-air based on an alkaline gel polymer electrolyte. This alkaline gel polymer electrolyte retains liquid-like hydroxide-ion transport properties, but can serve as a structural component to physically separate electrodes. Zinc-air batteries were fabricated by laminating a KOH-doped poly(vinyl alcohol) (PVA) gel electrolyte with a porous zinc film and an air electrode film that uses commercial Co_3O_4 nanoparticles as the bifunctional oxygen catalyst. PVA-KOH gel electrolytes have been developed for alkaline membrane fuel cells and alkaline Zn-MnO_2 batteries, but their use in rechargeable zinc-air batteries has not yet been reported.[138-141] In the next sections, the design and characterization of the electrolyte and electrode materials are

described; the PVA-KOH gel electrolyte's compatibility with electrodes is determined in a reversible quasi-solid-state system; the electrochemical performance and stability of a device built on a flexible substrate, with different bending conditions, is examined; and the adaptability of the proposed battery for serial/parallel combinations is also demonstrated.

3.2 Experimental section

3.2.1 Gel polymer electrolyte preparation

A gel polymer electrolyte membrane was prepared by a phase inversion technique. Poly(vinyl alcohol) (PVA) (99% hydrolyzed, average Mw 146,000-186,000, Sigma Aldrich) was fully dissolved in water under mechanical stirring at 90 ^{o}C to make a 5 wt% solution. After cooling down to room temperature, the 5 wt% PVA solution was casted onto a glass plate. Then the membrane was immersed immediately in an acetone (AR >99.5%, Sigma Aldrich) coagulation bath for 10 min, followed by freeze drying for 24 h. The resulting porous membrane was then cross-linked in 10 wt% glutaraldehyde solution (25% in H_2O, Sigma Aldrich) at 30°C for 10 min. The cross-linking proceeded between the -OH group of PVA and the –CHO group of glutaraldehyde in the membrane was due to an acid-catalyzed reaction by the addition of 100 µl HCl (reagent grade, 37%, Sigma Aldrich). After washing with distilled de-ionized water, the resulting membrane was soaked in a mixture of KOH/PVA (35/2 wt%) and equilibrated for 24 h. PVA-KOH gel electrolyte membrane with thickness ranges of 20 to 50 µm was thereby obtained.

3.2.2 Electrodes and zinc-air battery fabrication

A zinc anode material is consisted of (wt%) 88% zinc (purum powder <10 μm, Sigma Aldrich), 3 % Carbon nanofiber (CNF) (Pyrograf III, Pyrograf Products Inc.), 1% carbon black (CB) (Vulcan XC 72R) and 8% poly(vinylidene fluoride-co-hexafluoropropene) (PVDF-HFP) (average Mw 455,000, Sigma Aldrich) polymer binder. The CNF and CB were added to improve electrical conductivity of the electrode. The PVDF-HFP was well dissolved in acetone (AR >99.5%, Sigma Aldrich) to make 10% w/w solution. The mixture of the active materials and binder solution was magnetically stirred for 2 hours. The resulting slurry was spread by doctor blading on a glass substrate, and was first left at room temperature for 1 min. The free-standing zinc electrode was peeled off from the substrate and further dried in vacuum at 60 ^{o}C for 5 min. The thickness of the obtained zinc film ranged from 20 to 60 μm. A catalyst-carbon layer of the cathode comprising electroactive particles, carbon black and anionic polymer binder (AS-4 ionomer, Tokuyama Inc.) was coated on a carbon cloth as the gas diffusion layer (Fuel Cell Technology) with a catalyst loading of 1.0 mg $cm^{-2.}$ The as-received Co_3O_4 nanoparticles (<50 nm particle size, Sigma Aldrich) and the as-prepared core-corona structured $LaNiO_3$/NCNT were both used as the bi-functional electroactive material. The quasi-solid-state zinc air battery was fabricated through a layer-by-layer method in which the electrodes were placed face-to-face with PVA gelled membrane. The assembled device was pressed under a pressure of 5 MPa for 3 min with a sheeting press to enhance the integrity of the laminated structure.

3.2.3 Characterization and electrochemical measurement

Scanning electron microscopy (SEM) (LEO FESEM 1530) and transmission electron microscopy (TEM) (Bruker AXS D8 Advance) were utilized to observe the morphology of the electrode materials and the membrane. Electrochemical impedance spectroscopy (EIS) was conducted by operating the battery at a constant potential (e.g., 1.0 V) for the single cell and the tandem device, respectively, to evaluate the electrochemical process under discharging and charging conditions. Alternating current (AC) amplitude of 20 mV was applied with its frequency ranging from 100 kHz to 0.1 Hz. The in-plane ionic conductivity of the membrane was measured by a four-electrode system with the frequency ranging between 100 kHz to 1 Hz a with perturbation voltage amplitude of 100 mV. The electrocatalytic activity of Co_3O_4 nanoparticles and $LaNiO_3$/NCNT were evaluated by rotating disc electrode voltammetry using a potentiostat (CH Instrument 760D) and rotation speed controller (Pine Instrument Co., AFMSRCE). The polarization data were measured by a galvanodynamic method at a scan rate of 1.0 mA s^{-1} with a cut-off voltage of 0.5 V for the single cell and the two-cell in parallel assembly, and 1.0 V for the two-cell in series assembly. Charge-discharge pulse cycling was conducted by a recurrent galvanic pulse method with a constant current density of 250 A L^{-1} (50 A kg^{-1}), with each cycle consisting of 10 min for discharge followed by a 10 min charge.

3.3 Results and discussion

The laminar structure of the rechargeable zinc-air battery is illustrated schematically in **Figure 3-1**. The left part of **Figure 3-1** shows an optical photograph and cross-sectional scanning electron microscopy (SEM) image of the battery. The battery is fabricated by laminating a KOH-doped PVA gel electrolyte membrane between an air electrode comprising a

bifunctional oxygen catalyst loaded carbon cloth and a zinc film electrode. Cold-rolled copper (Cu) foil as a substrate is attached to the zinc electrode to ensure good electrical contact. The dimensions of the as-prepared thin-film battery shown in **Figure 3-1** are 1.2 cm × 4.0 cm, with a total thickness of 0.5 mm.

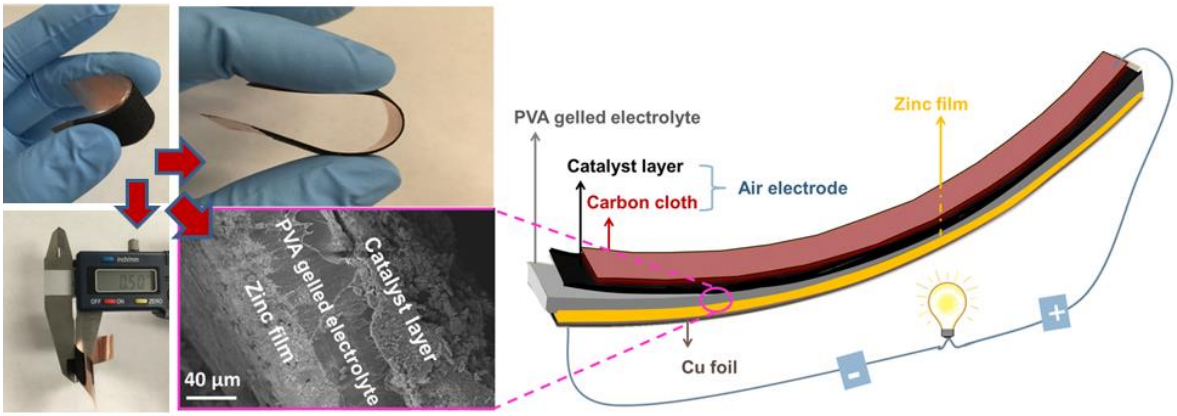

Figure 3-1. An illustration and images of the thin-film rechargeable zinc-air battery. (Left top: photos showing the physical flexibility of the cell; left bottom: the cross-sectional SEM image of the laminated structure of the battery).

Initially, a zinc electrode film (**Figure 3-2a**), a bifunctional catalytic air electrode film (**Figure 3-2b**) and a KOH-doped PVA gel electrolyte membrane (**Figure 3-2c**) were prepared, respectively. The SEM image of the zinc eletrode (**Figure 3-2d**) shows well distributed zinc particles, which are reinforced by an electrical conducting network of carbon nanofiber (CNF) additives. Additionally, the interfacial contact between zinc particles and CNF is further improved by poly(vinylidene fluoride-hexafluoropropylene) (PVDF-HFP) polymer binder. As illustrated in **Figure 3-2e**, the resulting free-standing zinc film is mechanically robust, and can be freely rolled, twisted and folded without any mechanical damage. The overall excellent mechanical robustness of the zinc film is attributed to the excellent distribution of zinc particles

through building up a three-dimensional (3D) interconnected network with CNF, carbon black and the binder, where the CNF and carbon black help to enhance the electrical conductivity of the 3D zinc film electrode. It is also worth mentioning that the PVDF-HFP/acetone binder system employed in this approach can not only ensure a short curing time (5 min) of the zinc film, but also avoid the oxidation of zinc particles during the electrode preparation. In this way, it provides advantages over other binder systems in aqueous medium,[142, 143] thus simplifying the fabrication of the zinc electrode. The as-prepared perovskite lanthanum nickel oxide/nitrogen-doped carbon nanotubes ($LaNiO_3$/NCNT) with unique core-corona morphology (**Figure 3-2f**) and the as-received cobalt oxide nanoparticles (Co_3O_4 NP) (**Figure 3-2g**) were both used as bifunctional catalysts. They were coated on a flexible carbon cloth substrate and then used as the air electrode. The transparent, porous PVA gel membrane, used as both the electrolyte and separator, was formed through the phase inversion method followed by cross-linking and doping of functional groups (hydroxide ion). The porous PVA matrix (**Figure 3-2h**) possesses both micro- and nano-sized pores that are robust enough to accommodate the electrolyte by capillary forces. This facilitates hydroxide ion transfer in quasi-solid state by the cross-linking process, which has been verified by studies published recently.[144, 145] The gel electrolyte exhibits excellent flexibility after doping with KOH and can provide a high ionic conductivity of 0.015 S cm^{-1} (**Figure 3-2i**).

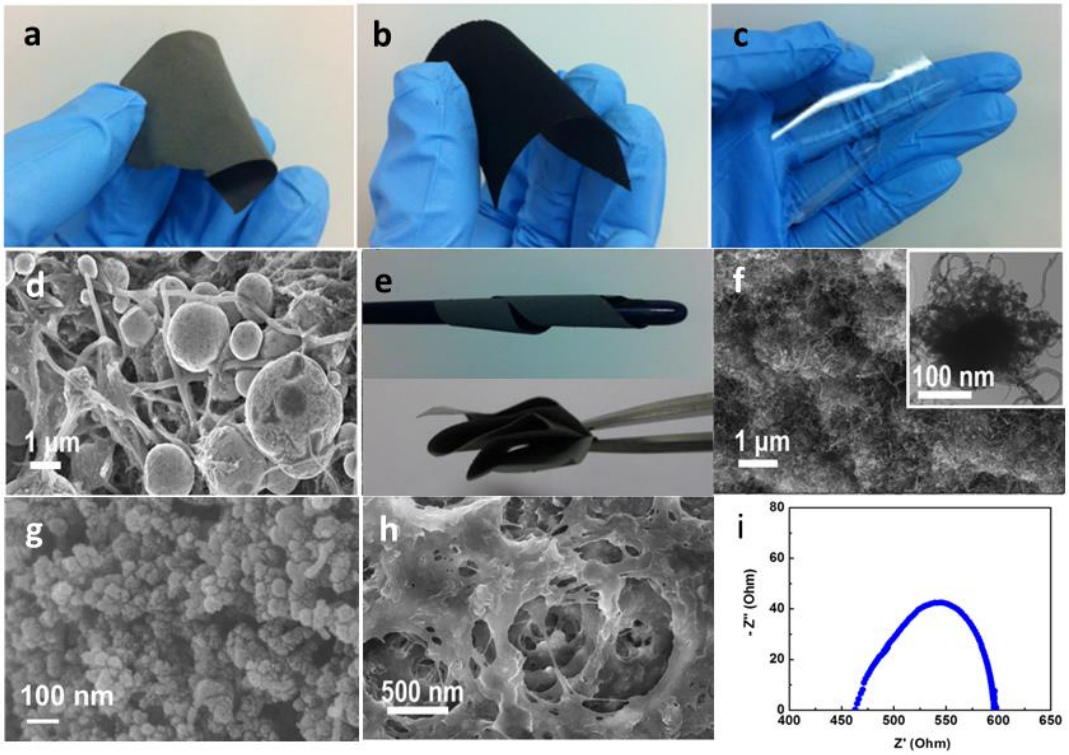

Figure 3-2. The optical pictures of a) the free-standing zinc electrode film, b) the bifunctional catalytic air electrode film using $LaNiO_3$/NCNT and c) the porous PVA gel electrolyte membrane. d) The SEM image of the porous zinc film. e) The digital pictures of the zinc film under rolled up and folded state. f, g) The SEM images of the bifunctional catalysts (the inset of f illustrates the core-corona structured $LaNiO_3$ nanoparticle and intertwined nitrogen-doped carbon nanotubes). h) The SEM image of the porous PVA gel electrolyte membrane. i) Nyquist plot of the impedance of the PVA gel electrolyte obtained at room temperature.

The development of multifunctional pliable electronics requires power sources that are physically flexible and have a stable performance. The battery fabricated in this study was bent towards the zinc film under a constant mechanical stress at different bending angles (**Figure 3-3a**). At each different angle, its galvanostatic charge-discharge cycling performance was investigated under ambient conditions using atmospheric air. The pulse cycling test was conducted at a constant current density of 250 A L^{-1} (50 A kg^{-1}) with each cycle being 20 min

(10 min discharge followed by 10 min charge). **Figure 3-3b** shows that, at any given bending angles, the cell exhibits excellent rechargeability and cycling stability for over 120 cycles without any significant degradation of performance. The discharge and charge potentials under a flat condition (0^o bending angle) remain virtually unchanged during the overall cycles. Similar characteristics of voltage retention for both charge and discharge are obtained at 90^o, 150^o and even 180^o bending angles, which are indicative of superior rechargeability and performance durability. This superior cycling stability and rechargeability of the cell could be attributed to its highly flexible components along with structural integrity between the electrodes and the gel membrane (**Figure 3-3c**). Compared with the potential of the flat cell over the duration of 120 cycles, only minuscule changes for both the charge and discharge potentials are observed even under extreme bending of 180^o. Nyquist plots of the cell impedance measured after the 120^{th} cycle at a potential of 1.0 V under different bending conditions (**Figure 3-3d**) show that the charge-transfer resistances (R_{ct}) are almost identical (*ca*. 12 ohm) under various bending conditions, whereas the interfacial resistances (R_{int}) shifted up by *ca*. 2 ohm at 180^o bending angle. The results indicate that the observed potential changes could be due to the delamination of the zinc electrode and the KOH-PVA gel electrolyte membrane at the folded region (**Figure 3-3c,** the inset), where the electrolyte is less accessible to the electrodes. At this region, the zinc electrode undergoes the highest compressive strain, meanwhile the air electrode suffers from the highest tensile stress.[50, 142]

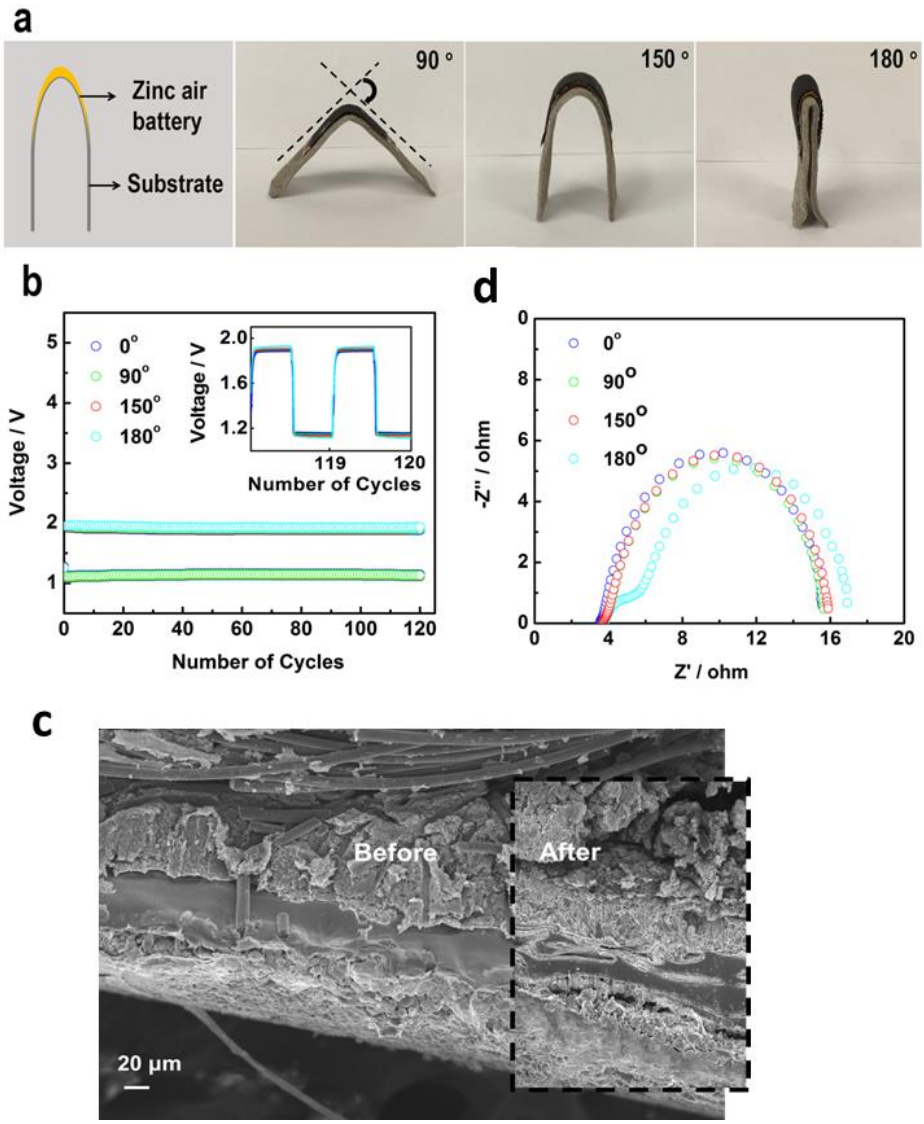

Figure 3-3. a) A schematic and optical pictures of the zinc-air battery under stress with different bending angles. b) Galvanostatic charge-discharge pulse cycling as a function of bending angles at a current density of 250 A L^{-1} (50 A kg^{-1}) with each cycle being 20 min (10 min discharge followed by 10 min charge). c) Cross-sectional SEM image of the zinc-air battery before and after (the square region outlined in black) cycling at a constant current density of 250 A L^{-1} (50 A kg^{-1}) with each cycle being 20 min (10 min discharge followed by 10 min charge). d) Nyquist plots of the impedance of the zinc-air battery as a function of bending angles at a potential of 1.0 V.

To further evaluate the performance of the zinc-air battery for use as a high-energy-density electrochemical energy storage, $LaNiO_3$/NCNT composite was utilized to measure the volumetric and gravimetric energy densities as a function of the charge-discharge current density (**Figure 3-4 a,b**). Compared to the battery prepared with as-received Co_3O_4 NP, the cell using $LaNiO_3$/NCNT shows both significantly higher gravimetric and volumetric energy densities, with more moderate decrease in energy density with increasing current densities. The enhanced performance can be attributed to improved catalytic activities during the oxygen reactions due to very strong synergy between $LaNiO_3$ and NCNT species (**Figure 3-4c**).[146] A high volumetric energy density of 2905 Wh L^{-1} (based on the zinc film volume) corresponding to a gravimetric energy density of 581 Wh kg^{-1} (based on the zinc film mass) can be achieved at a current density of 125 A L^{-1} (25 A kg^{-1}). One should emphasize that a higher practical energy density can be easily achieved by using even further active catalysts for the oxygen reactions. Moreover, to meet high-energy needs for some electronics, the thickness of active zinc mass can be easily increased for our battery. The effect of various zinc film thicknesses of the battery's specific capacity performance was examined using commercial Co_3O_4 NP as the bifunctional catalyst. **Figure 3-4d** compares the specific capacities among different thicknesses of the zinc film at a current density of 250 A L^{-1} (50 A kg^{-1}). One potential issue of increasing the film thickness is that it results in less accessible active surface area of zinc particles with the electrolyte. This deficiency consequently leads to higher diffusion resistances and polarization of the battery, resulting in energy density losses. However, **Figure 3-4d** shows that the batteries with different thicknesses of zinc film exhibit almost identical characteristics of potential and specific capacity up to 80% of full discharge. The thicker zinc films exhibit a small capacity

loss in terms of voltage decrease when completely discharging the batteries. This is because the internal resistance of the zinc film increases as more zinc oxide is generated during discharge. Nevertheless, the capacity obtained with the zinc film thickness of 60 µm is almost 3 times the one obtained with 20 µm zinc film (**Figure 3-4d**, inset). The highly achieved uniformity between different zinc film thicknesses indicates that both the 3D electrical-conducting network structure of the zinc electrode and the porous structure of the PVA gel electrolyte membrane help facilitate the electrolyte accessibility within the zinc electrode, thereby mitigating the polarization effect of diffusion and maintaining the specific capacity with a miniscule drop.

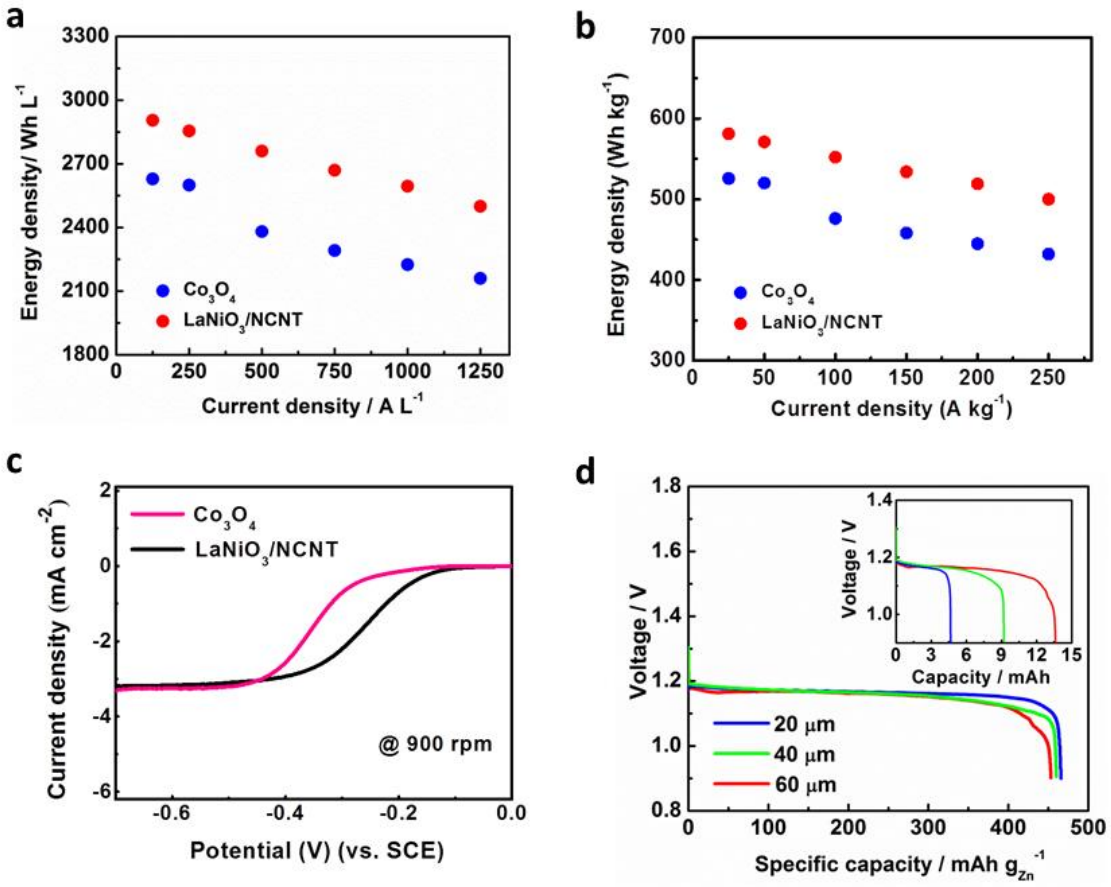

Figure 3-4. a) A comparison between volumetric energy densities of the thin-film zinc-air battery using Co_3O_4 and $LaNiO_3$/NCNT as a bifunctional catalyst for the air electrode. b) A

comparison between gravimetric energy densities of the thin-film zinc-air battery using Co_3O_4 and $LaNiO_3$/NCNT as the bifunctional catalyst for the air electrode. The gravimetric energy density calculation is based on the zinc electrode. c) ORR polarization curves obtained at rotation speed of 900 rpm with 10 mV s^{-1} scan rates of Co_3O_4 and $LaNiO_3$/NCNT. d) Typical specific capacity curves of the battery with different thicknesses of zinc film at a current density of 250 A L^{-1} (50 A kg^{-1}) with the inset view of the corresponding capacities. The gravimetric energy density and specific capacity calculation are based on the mass of zinc electrode.

It is known that a typical operating voltage range of rechargeable zinc-air batteries is between 1.2 V to 1.3 V, which is relatively lower than that of commercial Zn-MnO_2 batteries (*ca.* 1.5 V) and much less than that of lithium-ion batteries.[148] This inherently low working voltage of zinc-air batteries can be easily improved by stacking the batteries in series, in parallel, or in combination of the two to obtain high-voltage energy and power delivery.[149] The thin-film and flexible properties of the battery are amenable to these designs, allowing for less complex cell combinations and more compatibility to available space within electronics. However, cell-to-cell variations of the performance will result in low charge and discharge efficiency of the battery pack. To examine the feasibility of various combinations of our battery under real conditions for flexible energy storage, the energy and the power performance have been analyzed by connecting two 1-cm^2-area cells in series and parallel settings (**Figure 3-5a**) using as-received Co_3O_4 NP to prepare the air electrode. The as-assembled two single batteries show high uniformity of performance (**Figure 3-5b, c**). **Figure 3-5d** displays the discharge polarization curves in the configurations of the two cells in series. Compared with the single cell, the series connection shows almost two times higher discharge voltage when operating under the same current. This highly consistent voltage efficiency indicates that the output

power in the series connection can be extended to twice that of the single device with minimal power losses, which is confirmed by the result shown in **Figure 3-5d**, the inset. For example, the tandem device delivers a peak power of 56.1 mW with no significant power loss, corresponding to two times that of the single cell (28.2 mW).

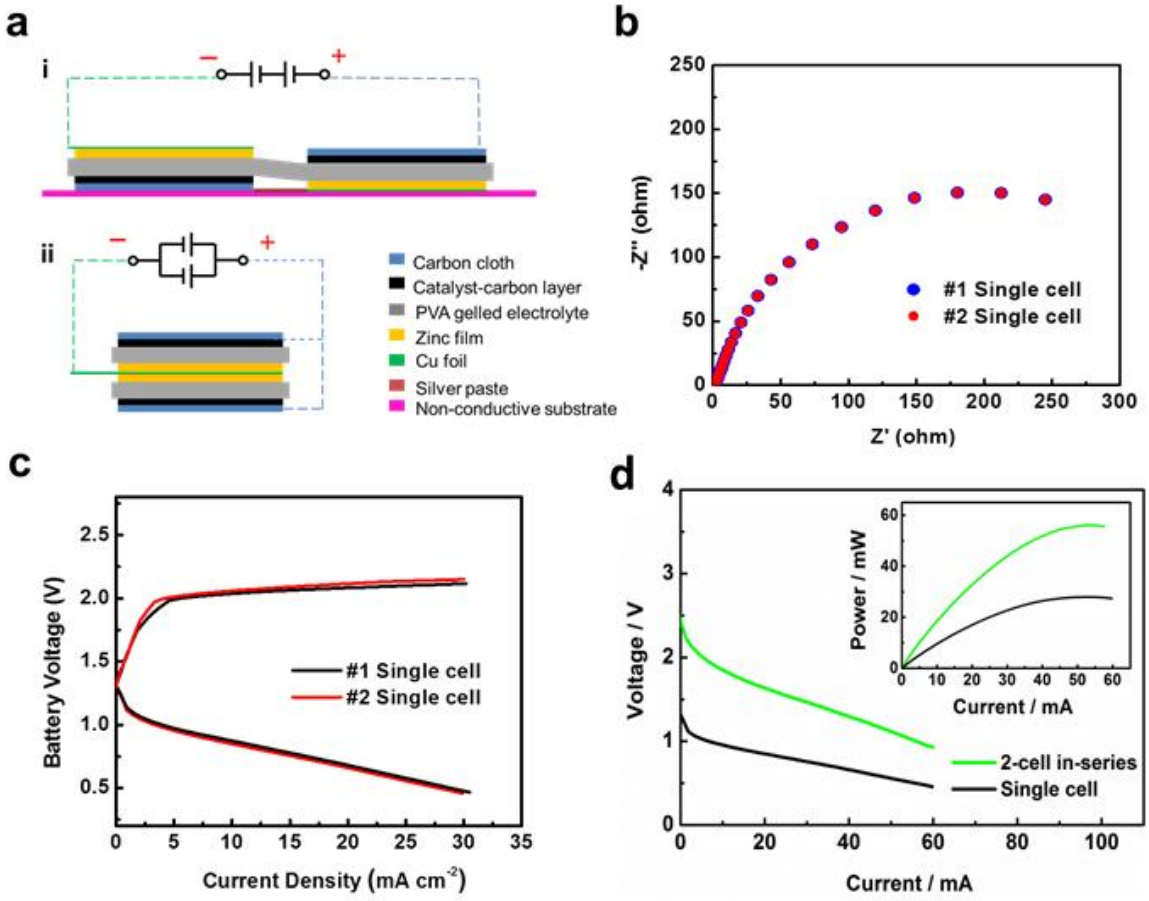

Figure 3-5. a) Schematic drawings of as-assembled devices in serial (i) and parallel (ii) configurations. b) Nyquist plots of the impedance (vs. OCV) of two single batteries. c) The charge-discharge polarization curves of two single batteries. d) The polarization curves of a single and tandem device connected in series. The corresponding power plot comparing with the tandem device with the single cell is shown on the top of inset.

The tandem device proportionally extended the output voltage for both the discharge and the charge by a factor of 2 compared to these of the single device. Two 1-cm^2-area batteries have also been stacked in parallel to investigate the device performance, as shown in **Figure 3-6a**. Compared to the single cell device, the output current has been increased by a factor of 2 at the same discharge voltage. As expected, the parallel assembly is capable of generating 28.1 mAh of capacity, which almost doubles that of the single device (14.4 mAh) at the same discharge rate of 1.0 mA (**Figure 3-6a**, the inset). These results, based on stacking cells in series and parallel, highlight the capability to improve overall device performance without much increase in the physical dimensions of the overall battery due to the flexible and thin form factor of the present all-solid-state zinc air battery. Its practical application has been further demonstrated by embedding a customized zinc air battery within an integrated freeform device. Two single batteries (size 1.5 cm × 5.0 cm) were connected in a series using a silver paste to make an external circuit connection, placed on a bracelet-shape plastic substrate (corresponding to 60^o bending angle) and covered with plastic wrap (**Figure 3-6b**, inset). This prototype can deliver a constant current of 15 mA at a voltage of 2.3 V, sufficient to power a red LED, which operates at a minimum voltage of 1.8 V. The prospect of wearable and portable application of the device was illustrated by applying it to a human wrist followed by lighting a red LED (**Figure 3-6b**). Electrochemical behaviors of the devices in both the serial and the parallel connection were further analyzed by electrochemical impedance spectroscopy (EIS) at a potential of 1.0 V with the frequency ranging from 100 kHz to 0.1 Hz. Nyquist plots of the impedance are shown in **Figure 3-6c,** with the equivalent circuit and an expanded view for the high-frequency region provided in the inset. The single, tandem and parallel devices all display

similar electrochemical characteristics, comprising a small incomplete arc in the high-frequency region and a semicircle in the intermediate-low frequency region. The value of the first interception, at the high-frequency end, mainly represents the sum of ohmic resistances (R_{ohm}) of the gel electrolyte membrane and the electrodes, and the contact resistance of the device with an external circuit. The incomplete arc, at the high-frequency range, mainly reflects an interfacial resistance (R_{int}) and capacitance (C_{int}) behavior between the electrodes and the electrolyte. The intermediate-low frequency part corresponding to the second semicircle is associated with a charge-transfer resistance (R_{ct}), coupled with an interfacial capacitance (C_{dl}). As indicated by the impedance of the serial configuration in **Figure 3-6d**, both the R_{int} and the C_{int} do not vary with potential, deriving from the effect of physical processes. However, the R_{ct} and the C_{dl} are strongly potential-dependent, indicating a trend whereby the diameter of the loops reduces as the potential decreases due to the increased driving force of higher overpotential. The R_{ohm}, R_{int}, R_{ct} and the total resistance of the devices have been quantified, respectively, on the basis of the equivalent circuit model (**Figure 3-6c**, inset and **Table 3-1**). In this case, the combinations stacked either in series or in parallel, have no significant effect on the R_{ct}. The R_{ct} for series and parallel connections are almost identical to twice and nearly half that of the single cell, respectively. Slight increases in the total resistance of the series assembly (by 1.6 ohm) and the parallel assembly (by 1.5 ohm) are observed compared to that of the single cell (23.6 ohm). The resistance increase can be attributed to the contact resistance of the cell combinations with the external circuit. Because of the low resistances demonstrated by series and parallel devices, a high performance battery in terms of energy and power can be

achieved with minimal performances losses, which are also consistent with the performance exhibited in **Figure 3-5d and 3-6a**.

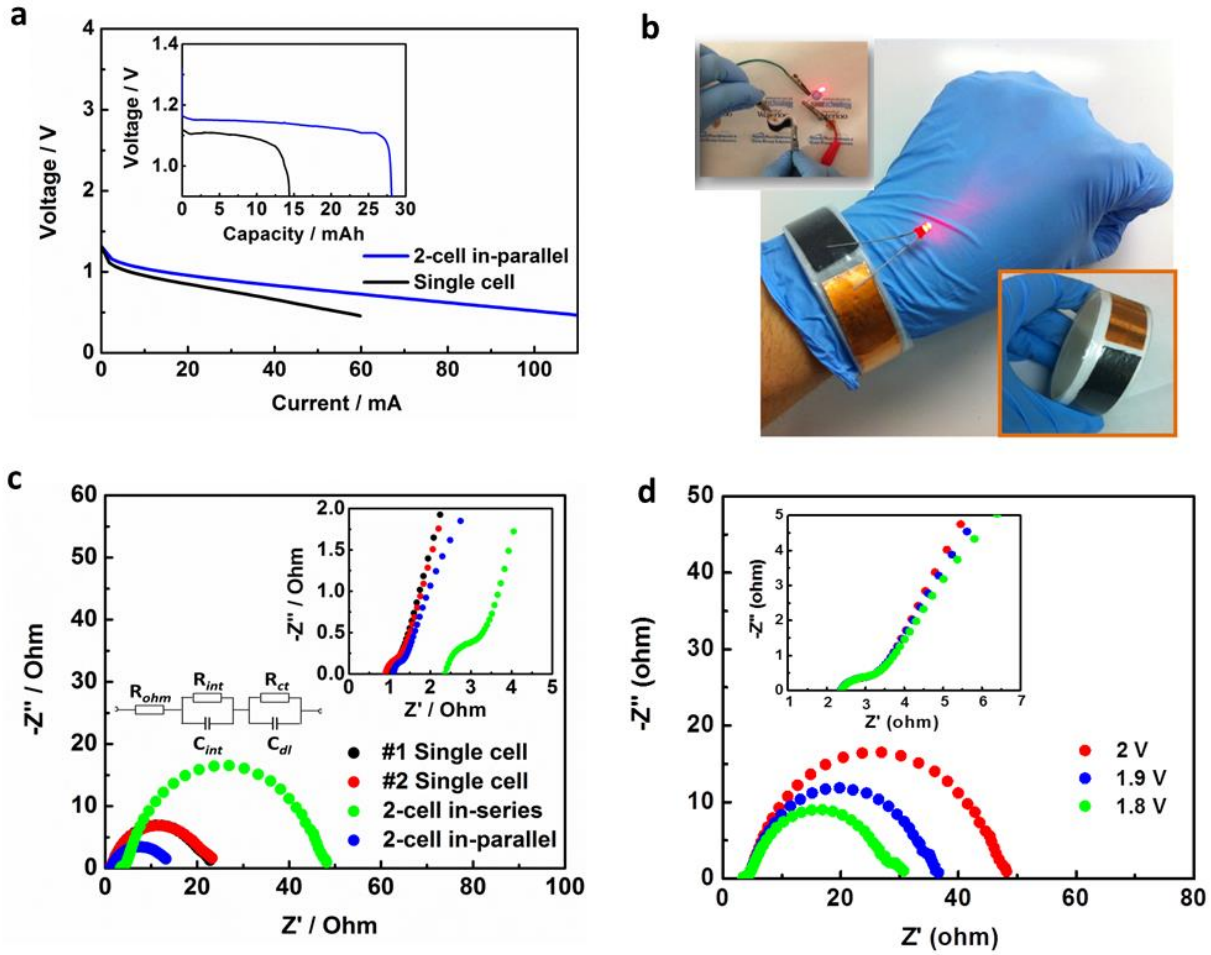

Figure 3-6. a) The polarization curves of the single and the device in parallel. The corresponding capacity curve comparing with the single cell is shown on the top of inset. b) A demonstration of wearable prototype integrated with a tandem device to power a red LED under bent condition. c) Nyquist plots of the impedance of two single cells and the devices connected in a series and in a parallel at a potential of 1.0 V, with a magnification of the high-frequency region in the inset. d) Nyquist plots of the impedance of the tandem device as a function of potential, with a magnification of the high-frequency region in the inset.

Table 3-1. The values of the equivalent circuit elements based on the EIS analysis of the single cells and the batteries connected in series and in parallel.

	R_{ohm} [a] (ohm)	R_{int} [b] (ohm)	R_{ct} [c] (ohm)	R_t [d] (ohm)
#1 Single cell	1.0	0.5	22.1	23.6
#2 Single cell	0.9	0.5	22.2	23.6
2-cell in series	2.4	1.5	44.9	48.8
2-cell in parallel	1.1	0.6	11.6	13.3

[a]Ohmic resistance. [b]Interfacial resistance. [c]Charge-transfer resistance. [d]Total resistance.

3.4 Conclusions

A proof-of-concept application of KOH-doped PVA gel electrolyte to quasi-solid-state rechargeable zinc-air batteries was demonstrated by layer-by-layer fabrication. The battery has a high volumetric energy density of 2905 Wh L^{-1} and gravimetric energy density of 581 Wh kg^{-1}. The advantage of the fabrication approach is that the battery components can be casted or printed as sheets of customized shape and size to fit space and energy needs for a variety of applications. The flexibility of increasing energy and power performance of this device was also demonstrated by stacking cells in series/parallel or in combinations of the two, as well as using an improved bifunctional catalyst. The direct bonding of electrodes with gel electrolyte enables the assembled batteries to attain good cycle stability over 120 cycles at a charge-discharge rate of 250 A L^{-1} (50 A kg^{-1}) under different bending conditions.

Chapter 4 Hydroxide ion-conductive electrolyte membrane based on highly quaternized cellulose nanofibers for PEMZAB

4.1 Introduction

The aforementioned work in Chapter 3 reveals that a KOH-doped PVA gel can serve as a good quasi-solid polymer electrolyte to provide hydroxide ion conduction for rechargeable zinc-air batteries. However, one issue associated with this gel electrolyte is the progressive loss of its ionic conductivity as water and doped KOH are released from the porous PVA matrix during the formation of carbonate/bicarbonates, when the battery is operated under ambient atmosphere containing CO_2. Such a loss of gel electrolyte conductivity will cause a large ohmic polarization during the course of battery operation, which severely damages battery power, energy performance and cycling stability. Moreover, the gel membrane does not possess hydroxide-ion selectivity, causing crossover of zincate ions from the zinc electrode to the air electrode driven by their concentration gradient in the battery. This crossover gives rise to ZnO deposition on the air electrode surface, therefore reducing capacity retention during discharge and charge cycling.

To address these issues, this chapter focuses on the design and characterization of an efficient hydroxide ion-conductive, nanofibrous cellulose electrolyte membrane with improved hydroxide ion-conductivity, chemical stability and water retention. Being the most earth-abundant and renewable polymer material on the earth, natural cellulose fibers play a critically important role in addressing future energy and environmental challenges.[150-153] Cellulose nanofibres are particularly interesting due to their appealing characteristics, such as large specific surface area rich in hydroxyl groups, high mechanical strength, high surface-to-volume

ratio and light weight,[154-156] offering the possibility of being solid-state electrolytes for lightweight and flexible energy storage devices. By taking advantage of these unique properties of cellulose nanofibres, a thin and robust nanofibrous membrane with high water retention can be prepared. Meanwhile, hydroxide ion-conductive cellulose nanofibres were designed through a surface-quaternization of these nanofibres. Particularly, a self-crosslinking occurs among these quaternized nanofibers at mild temperature (60 ^{o}C), which can further enhance the dimensional stability of the membrane. The promise of enhancing the intrinsic physical and chemical properties of cellulose nanofibers leads to appreciable improvements in both the hydroxide ion conductivity and chemical stability of the nanofibrous membrane for the use in zinc-air batteries.

4.2 Experimental section

4.2.1 Preparation of cellulose nanofibers

The cellulose nanofibres were produced from Northern Bleached Softwood Kraft pulp (New Brunswick, Canada) through pre-refining, enzymatic processing and nano-refining. The disintegrated pulp was pre-refined using a Noram PFI mill (Quebec, Canada) with a revolution speed of 30000. To gain a uniform pulp suspension, an enzyme treatment of the refined pulp was conducted by using a mixture of two enzymes (i.e., Mannanase and Xylanase) from Novozymes (Franklinton, USA). The enzyme treated pulp was thoroughly washed with DDI water to remove any soluble residues and was charged into the PFI mill with an increased rotation speed of 30000 to produce cellulose micro/nanofibrils.

4.2.2 Fabrication of hydroxide ion-conductive nanocellulose membrane

Dimethyloctadecyl[3-(trimethoxysilyl)propyl]ammonium chloride (DMOAP) (42 wt. % in methanol, Sigma Aldrich) was used as the precursor for functionalizing cellulose nanofibers. First, the cellulose nanofibres were dispersed and stirred in DDI water to get a uniform cellulose fiber suspension. DMOAP precursor was diluted with methanol solution to a concentration of 10% and then was added into the cellulose fibre suspension. The amount of DMOAP varied from 100 to 300 mol % with respect to the cellulose repeating glucose unit. The mixture of cellulose fibres and DMOAP was stirred at room temperature for 12 h. Then, the resulting solution was centrifuged and washed several times with ethanol and DDI water to remove any unreacted traces of DMOAP. The quaternary ammonium functionalized cellulose membranes were fabricated by vacuum filtration and dried at room temperature for 6 h and then was cross linked at 60 ^{o}C under vacuum for another 24 h. The resulting membrane with a thickness of 30 μm was hydroxide-exchanged from Cl- form to OH- form in 1M KOH solution for 24 h. Finally, the hydroxide-exchanged membrane was washed and soaked in DDI water. The 1M KOH-doped pristine cellulose (KOH-PC) membrane was prepared by soaking the pristine cellulose membrane in 1M KOH solution for 24 h without washing by DDI water.

4.2.3 Fabrication of the PEMZAB

A flexible zinc electrode, consisted of zinc powder (purum powder, Sigma Aldrich), carbon nanofiber, carbon black and poly(vinylidene fluoride-co-hexafluoropropene) polymer binder,[135] was prepared for the battery testing. The mass of the zinc electrode as prepared was 40 mg. As-received Co_3O_4 nanoparticles (<50 nm particle size, Sigma Aldrich) were used as the bi-functional electroactive material to fabricate the air electrode. Catalyst ink consisted of

Co_3O_4, ionomer (AS-4, Tokuyama Inc.) and 1-propanol (anhydrous, 99.7%, Sigma Aldrich) was sprayed onto a carbon cloth (Fuel Cell Technology) as the gas diffusion layer with a catalyst loading of 1.0 mg cm^{-2}. The in-house battery prototype was fabricated through the layer-by-layer casting by which the electrodes were placed face-to-face with the membrane. All the tested membranes were pre-wetted with 1M KOH solution before battery assembly.

4.2.4 Characterization and electrochemical measurements

X-Ray Diffraction (XRD) (INEL XRG 3000), Fourier transform infrared spectra (FTIR) (Avatar 320) and X-ray photoelectron spectroscopy (XPS) (Thermo Scientific Al K-Alpha X-ray source) were conducted to characterize crystal structure and the surface chemistry of the functionalized cellulose membranes. Scanning electron microscopy (SEM) (LEO FESEM 1530) and transmission electron microscopy (TEM) (Bruker AXS D8 Advance) were utilized to observe the morphology of the cellulose nanofibers and the membrane. Pore size distribution of the membrane was characterized by atomic force microscopy (AFM) (Vecco Dimension 3000). Electrochemical impedance spectroscopy (EIS) (VersaSTAT MC potentiostat) was carried out in the frequency ranging from 100 kHz to 0.05 Hz with potential amplitude of 20 mV. Electrochemical evaluations were conducted under atmospheric air. Polarization data was collected using the galvanodynamic method at a scan rate of 1.0 mA s^{-1} with a cut-off voltage of 0.5 V for discharge and 2.5 V for charge. Galvanostatic discharge was tested at various constant current densities using a battery tester (Neware BTS3000). Discharge and charge cycling was conducted by a recurrent galvanic pulse method at a constant current density of 250 mA g^{-1} with each cycle consisting of 30 min. for discharge followed by a 30 min. charge.

4.3 Results and Discussion

The quaternary ammonia-functionalized nanocellulose (QAFC) membrane was fabricated through a filtration process. The QAFC membrane contains numerous cellulose fibres including micron-sized fibre bundles and micro/nanofibrils, which result in a translucent membrane (**Figure 4-1a**). The structure of the PEMZAB using the QAFC membrane was illustrated in **Figure 4-1b**. During discharge, generated hydroxide ions can migrate from the reaction sites at the air electrode to the zinc electrode forming zinc oxide. During charging, the QAFC membrane can transport hydroxide ions produced at the zinc electrode to the air electrode, at which the oxygen evolution reaction takes place.

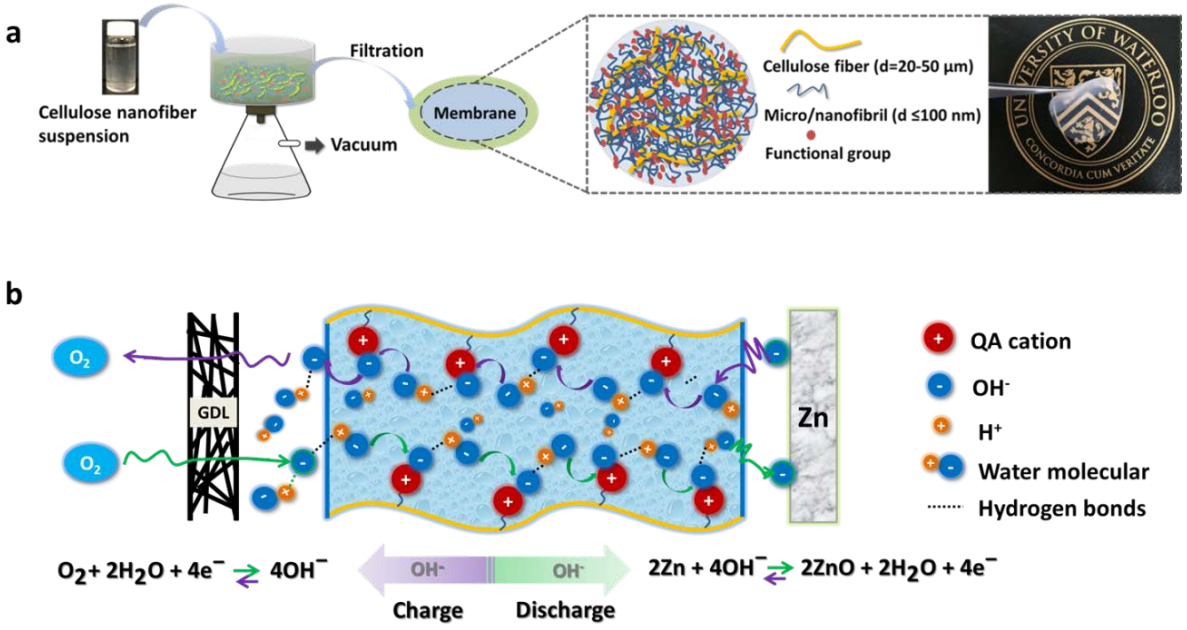

Figure 4-1. a) The procedure for the preparation of the quaternary ammonia-functionalized nanocellulose (QAFC) membrane. b) Schematic diagram of the PEMZAB using the

functionalized nanocellulose membrane. (GDL: gas diffusion layer; QA: quaternary ammonium)

Chemical structure changes at the surface of the functionalized cellulose nanofibers are illustrated in **Figure 4-2a**. Dimethyloctadecyl [3-(trimethoxysilyl) propyl] ammonium chloride (DMOAP) was utilized as the functional precursor containing quaternary ammonia (QA) moieties. First, DMOAP initiated the quaternarization of cellulose nanofibers (**Figure 4-2a**, Step 1) through the formation of hydrolyzed silanol intermediates and the adsorption of these intermediates onto the cellulose surface by hydrogen bonding (**Figure 4-2b**).[157] Subsequent thermal treatment, namely, crosslinking (**Figure 4-2a**, Step 2), allowed these hydrolyzed functional moieties to further react with the hydroxyl groups of cellulose by forming interfacial covalent bonds (Si-O-C). Additionally, the hydroxyl groups of the functional moieties can undergo self-crosslinking and form siloxane bonds (Si-O-Si). As a result, a covalent cross-linking bonding-network (**Figure 4-2c**), formed between the functional moieties and the cellulose nanofibres, is considered to enhance the dimensional stability of the membrane.[158-160] The functional groups as attached were further alkaline exchanged (**Figure 4-2a**, Step 3) and thus the membrane became hydroxide (OH^-) conductive.

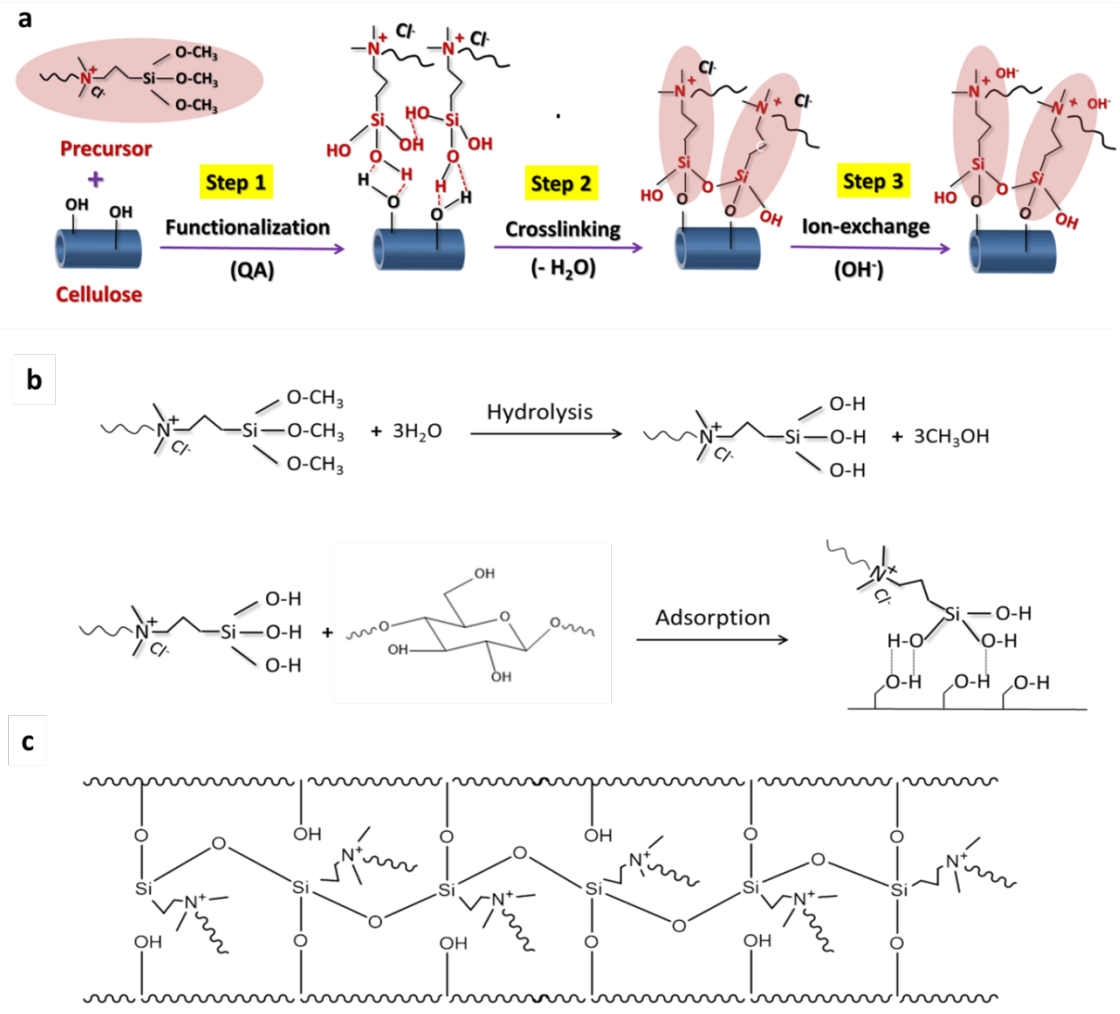

Figure 4-2. a) The chemical structure evolution of the cellulose nanofibre surface after functionalization, crosslinking and hydroxide-exchange. b) Proposed reaction mechanism for cellulose surface-functionalization with DMOAP. c) The covalent cross-linking bonding-network of the QAFC membrane.

The crystalline structure of the membrane made of the pristine cellulose nanofibres (PC membrane) and QAFC membranes were studied by XRD (**Figure 4-3a**). The cellulose nanofibres modified with 100 mol%, 200 mol% and 300 mol% concentration of DMOAP are denoted as 1-QAFC, 2-QAFC and 3-QAFC, respectively. The PC

membrane displayed a typical profile of cellulose I crystalline form with three characteristic peaks corresponding to crystalline planes (101), (002) and (040).[161] However, strong reductions of all the three characteristic peaks for the QAFC membranes were detected after functionalization. Specifically, with an increased concentration of DMOAP in the reaction, more pronounced decreases at the (002) plane were observed for the 2-QAFC and 3-QAFC samples, indicating that a significant portion of the cellulose I crystalline structure had transformed into the amorphous phase. This result suggests that the flexibility of cellulose nanofibers can be improved after the functionalization, which is due probably to the increase of the amorphous regions in the QAFC membranes. Moreover, the local hydrophilic domain near the hydroxide-ion charges will increase accordingly with the increased amorphousness in the membrane, making ion transport become easier through these hydrated regions.[162]

FTIR spectra of the PC membrane and QAFC membranes are compared in **Figure 4-3b**. The peak at ~3360 cm^{-1} corresponds to the O-H stretch vibration of intramolecular and intermolecular hydrogen bonds in the PC membrane. The fact that the peak tended to broaden for the QAFC membranes in the region 3480-3220 cm^{-1} could be associated with a large quantity of absorbed water in the more amorphous domain in the QAFC membranes.[163] Additionally, the increase in the absorption intensity at 1640 cm^{-1}, assigned to the water bending vibration in the amorphous regions, implies a higher amount of the bound water in the QAFC membranes.[164] The new peaks at ~2350 cm^{-1}, assigned to the O=C=O stretching vibration mode, are correlated with the carbonate species formed in the QAFC membranes. The presence of carbonate species is due to the

dissociated hydroxide ions in the QAFC membranes that can be converted into carbonates by the adsorption of CO_2 from the air.[165] Particularly, this peak intensity increased accordingly with increasing the concentration of DMOAP in the reaction; a trend which is consistent with the degree of QA functionalization. Additionally, although there is an overlap of Si-O-Si, Si-O-C and C-O stretching in the band region of 1000-1250 cm^{-1} in the PC and QAFC membranes,[166] the intensity of the broad peak at 1055 cm^{-1} (Si-O-Si) increased with the degree of QA functionalization, confirming the successful functionalization of cellulose nanofibers. XPS was carried out to further investigate the changes in surface chemistry resulting from the functionalization of cellulose nanofibers. The XPS survey spectra of the PC and 2-QAFC membranes are displayed in **Figure 4-3c**. Compared to the O/C atomic ratio of the PC membrane (0.69), the value of the 2-QAFC membrane decreased toward 0.51, indicative of a relative increase in carbon atoms at the cellulose surface due to the long alkyl chains of the attached QA functional groups. Three new peaks of the 2-QAFC membrane at binding energies of 103.1 eV, 154.1 eV and 401.4 eV were assigned to Si 2p, Si 2s and N 1s, respectively, whereas the presence of N and Si was not detected in the PC membrane. Additionally, the nitrogen bonding states of the 2-QAFC membrane are distinctive from the high-resolution N 1s spectrum in **Figure 4-3d**. The strong peak at 401.3 eV (92.9 atomic %) was attributed to quaternary-N species in 2-QAFC,[167] while the small peak at 403.9 eV (7.1 atomic %) was related to quaternary-N^+-O^- species.[159] The result reveals that quaternary ammonium is the dominant nitrogen species in the 2-QAFC membrane.

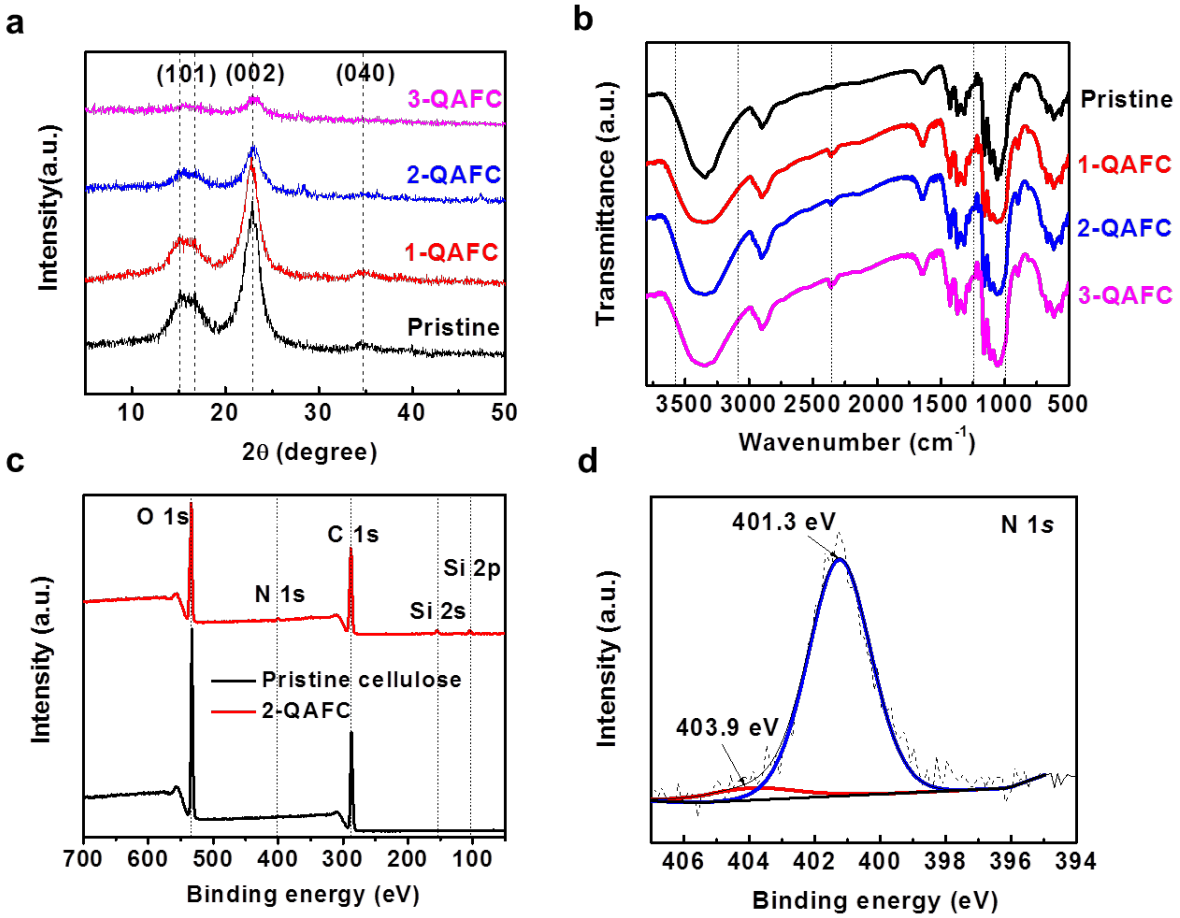

Figure 4-3. a) X-ray diffraction and b) FT-IR spectra of the PC and QAFC membranes. c) XPS survey spectra of the PC and 2-QAFC membranes, and d) deconvolution of N 1s peak of the 2-QAFC membrane.

The as-prepared cellulose nanofibers are composed of a variety of micron-sized cellulose fibres and fine fibrils with lengths of over several hundred microns (**Figure 4-4a**). **Figure 4-4b** exhibits that the fine fibrils unravelled from the micron-sized fibre fragment have a greatly expanded surface area. TEM images (**Figure 4-4c, d**) further identify that the diameters of these fine fibrils range from 10-30 nm for nanofibrils up to several hundred nanometers for microfibrils. These isolated nanofibers

(micro/nanofibrils) tend to construct smaller a porous structure with a higher surface area in the fibrous membrane than the micron-sized fibres. The surface morphology of the 2-QAFC membrane was further characterized by SEM. The membrane surface appears as a homogenous and dense nanofiber network intertwined with the micron-sized fibres functioning as the strong "scaffold" (**Figure 4-4e**). A high resolution SEM image (**Figure 4-4f**) reveals that the membrane possesses a porous structure in the nanoscale with a significant amount of pores throughout the nanofiber network. The nanosized pores and nanofibres in the membrane are smaller than the wavelengths of visible light, making the membrane translucent (**Figure 4-4g**).[154] In addition, the large contact area and covalent cross-linking bonds among functionalized nanofibres within the nanofibre network, along with the high strength of individual nanofibres give the membrane a very high tensile strength.[168] A microscopic view of a knotted 2-QAFC membrane in **Figure 4-4h** reveals its excellent flexibility without discernible physical fracture.

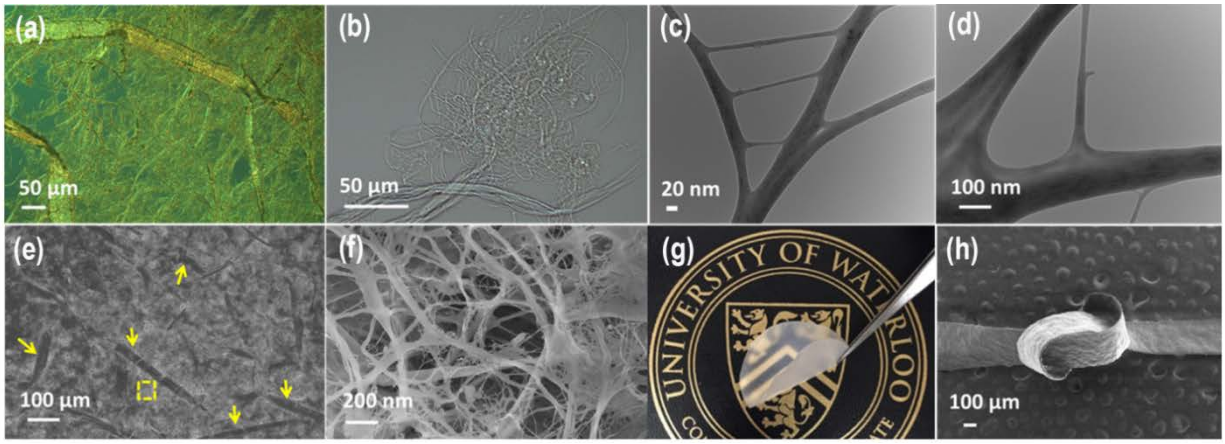

Figure 4-4. a) and b) Optical images of the cellulose fibre bundles with unraveled fine fibrils. c) and (d) TEM images of the micro/nanofibrils. e) A SEM image (surface view) of the 2-

QAFC membrane. Yellow arrows point to the micron-sized cellulose fibre bundles. f) A high magnification SEM image from the square region of e) outlined in yellow. g) A photograph of the 2-QAFC membrane having a translucent appearance. h) A SEM image of a knotted 2-QAFC membrane showing excellent flexibility.

In addition to outstanding flexibility, the interconnected nanoporous structure of the 2-QAFC membrane plays an important role in absorbing and retaining water as well as maintaining dimensional stability in the water-swollen state of the membrane. It is apparent that high water uptake would be favourable for ionic conductivity, benefiting from the hydrated ion-transport channels throughout the membrane.[162] For the purpose of comparison, the water uptake and swelling behaviour of the commercial AAEM (A201, Tokuyama Corporation, Japan), 2-QAFC and PC membranes were measured (**Table 4-1**). The PC membrane showed more than 2 times higher water uptake than that of the A201 membrane, owing to the excellent hydrophilic nature of cellulose and the large internal surface area of cellulose nanofibres within the nanoporous structure. Compared to the PC membrane, the 2-QAFC membrane showed a slightly higher water uptake but pronounced lower through-plane and in-plane swelling ratios. The result suggests that the covalent cross-linking bonding-network formed between the functionalized cellulose nanofibres in the 2-QAFC membrane is strong enough to allow the membrane to hold a significant amount of water with lower bulk volume expansion.[154] The ratio of through-plane swelling to in-plane swelling is often used to depict the extent of swelling anisotropy of membranes.[169] Compared to the A201 membrane, the fully hydrated PC membrane exhibited a much lower anisotropic swelling degree (**Table 4-1**). In addition, this anisotropic swelling behaviour is even less

affected by the functionalization. It was found that the 2-QAFC membrane showed only moderate anisotropic swelling as its anisotropy degree (1.1) was even lower than that of the PC membrane (2.8). This result demonstrates that the surface-functionalization of cellulose nanofibers enhances the dimensional integrity of the membrane by decreasing the swelling of both the in-plane and through-plane direction. The strong dimensional integrity of the membrane is particularly desirable for long-term battery cycling operation.

Table 4-1. Physical properties of the PC, 2-QAFC and A201 membranes.

Membrane	PC	2-QAFC	A201
Thickness (μm)	30	30	28
Water uptake (%)	95.4	95.6	44.3
In-plane swelling ratio (%)	17.8	13.6	8.2
Through-plane swelling ratio (%)	50.2	14.6	35.7
Anisotropic swelling degree	2.8	1.1	4.4

The ionic conductivities (σ) of the PC and QAFC membranes were measured using a four-probe alternating current (AC) impedance spectroscopy method. As shown in **Figure 4-5a**, the ionic conductivities of the QAFC membranes were significantly improved compared to that of the PC membrane. The marked improvement in the ionic conductivity is ascribed to the hydroxide ions disassociated from the QA functional groups in the hydrated regions. It also should be noted that the chemical and nanoporous structure of the QAFC membranes can trap extra alkali during the hydroxide exchange process. The excess "free" (physically absorbed and hydrogen bonded) alkali will result in an improvement of the ionic conductivity.[138, 170, 171] **Figure 4-5b** shows the ionic

conductivity of the 2-QAFC membrane soaked in distilled de-ionized (DDI) water as a function of time. While a decline in conductivity was observed at an initial stage, the conductivity of the 2-QAFC membrane did not show further decrease after 80 h. The initial decrease of the conductivity is mainly due to the excess "free" alkali which was gradually leached out in water. Regardless of the release of alkali, the 2-QAFC membrane exhibited a high ionic conductivity of 21.2 mS cm^{-1}, benefiting from the dissociated hydroxide ions from QA functional groups in the membrane. To better understand the ion transport mechanism of the 2-QAFC membrane, the temperature dependence of the ionic conductivity was evaluated in the range of 30 ^{o}C to 70 ^{o}C. Ionic conductivity of a commercial A201 membrane was also plotted for comparison. As shown in **Figure 4-5c**, the 2-QAFC membrane exhibited a similar positive temperature-conductivity linear relationship to the A201 membrane, indicating the transport of hydroxide charge (OH^-) in the 2-QAFC membrane results from the Grotthuss hopping mechanism.[47, 48] The activation energies (E_a) can be evaluated from the slope of the ln(σ) *vs.* (1000/T) plot using the Arrhenius equation. The E_a of the A201 membrane is 11.26 kJ mol^{-1}, in agreement with that reported in the literature,[172] whereas the E_a of the 2-QAFC membrane (8.76 kJ mol^{-1}) is considerably smaller than that of the A201 membrane with a higher hydroxide ion-conductivity of 40 mS cm^{-1}. The lower E_a suggests that the 2-QAFC membrane facilitates the hydroxide ion hopping in polymer chains compared to the A201 membrane as the temperature increases. It is likely that the nanoporous structure of the 2-QAFC membrane provides a significant amount of free

volume, which leads to relatively high segmental motions of cellulose chains in the amorphous phase.

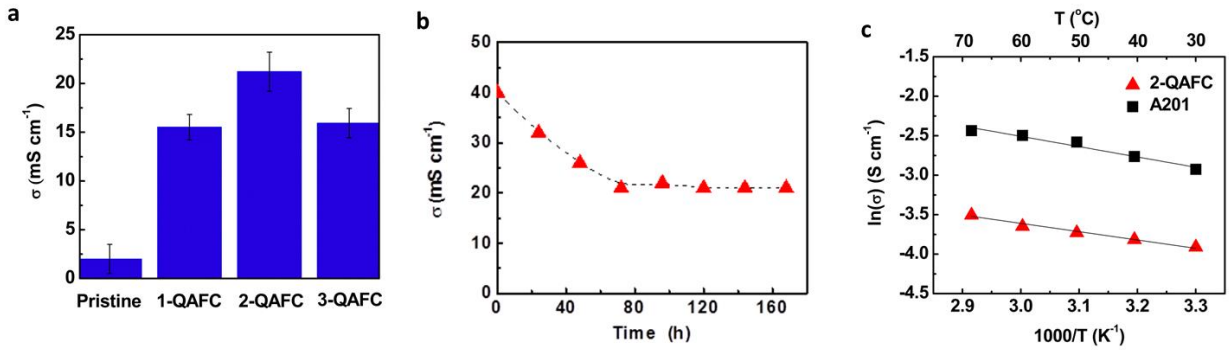

Figure 4-5. a) Ionic conductivity of the PC and QAFC membranes. b) Ionic conductivity of the 2-QAFC membrane as a function of time. c) Arrhenius plot of ionic conductivity of the 2-QAFC and A201 membranes as a function of temperature.

Compared to aqueous alkaline electrolytes in conventional zinc-air batteries, the hydration degree of the polymeric electrolyte membranes is one of the key factors that influence the cell performance such as power output, capacity and cycle life. High water content of membranes can facilitate the conduction of hydroxide-ions and the resulting reaction kinetics of batteries. Additionally, a certain amount of residual water in membranes is necessary to support sustained hydroxide-ion transport during battery operation because water also participates as the reactant in the oxygen reduction reaction during discharge. To construct the PEMZAB, I used commercial Co_3O_4 nanoparticles loaded on a carbon cloth to prepare the bifunctional air electrode and paired it with a porous zinc electrode. The 2-QAFC membrane was sandwiched between the two electrodes. A battery using the A201 membrane was also fabricated for comparison. **Figure 4-6a** shows the glavanostatic discharge performance of the solid-state zinc-air

batteries using the 2-QAFC, A201 and KOH-PC (1M KOH-doped pristine cellulose) membranes. The measurement were carried out at a constant current of 25 mA g^{-1} under atmospheric air. Although the A201 battery initially had a higher discharge voltage, the 2-QAFC battery quickly surpassed the A201 battery, having a ~180 mV higher voltage plateau and significantly higher discharge capacity (longer discharge time) after 25 min. While the KOH-PC battery shared a similar capacity with the 2-QAFC battery, the 2-QAFC battery displayed a higher discharge plateau, indicating a higher energy density than the 2-QAFC battery. The specific capacity of the battery using the 2-QAFC membrane normalized to the mass of zinc electrode was 492 mAh g^{-1}, which is superior to the values reported on polymer-based Zn-air and Zn-MnO_2 batteries.[6, 49-51] The battery as fabricated also showed a high-power density of 2362 mW g^{-1} at a large current density of 4650 mA g^{-1} (**Figure 4-6b**). The rapid voltage and capacity loss of the A201 membrane is due to a progressive loss of water and ionic conductivity in the membrane during the constant current discharge. It should be noted that simply wetting the A201 membrane with DDI water could regenerate the battery performance for subsequent runs with the same battery configuration. The gradual voltage decay of the battery using the KOH-PC membrane especially after 500 min is related to the continuous depletion of the alkali absorbed in the porous structure, which increased the overall resistance of the battery. On the other hand, the battery using the 2-QAFC membrane showed a steady decline from 1.3 V to 0.9 V after 500 min, and remained at this voltage over 1000 min. The steady performance can be attributed by the presence of high levels of bound water in the 2-QAFC membrane, thereby mitigating the ohmic polarization of the battery due

to minimal loss of ionic conductivity. As a result, the 2-QAFC membrane exhibited a higher discharge capacity with a more stable voltage character in comparison to the commercial A201 membrane and the KOH-PC membrane.

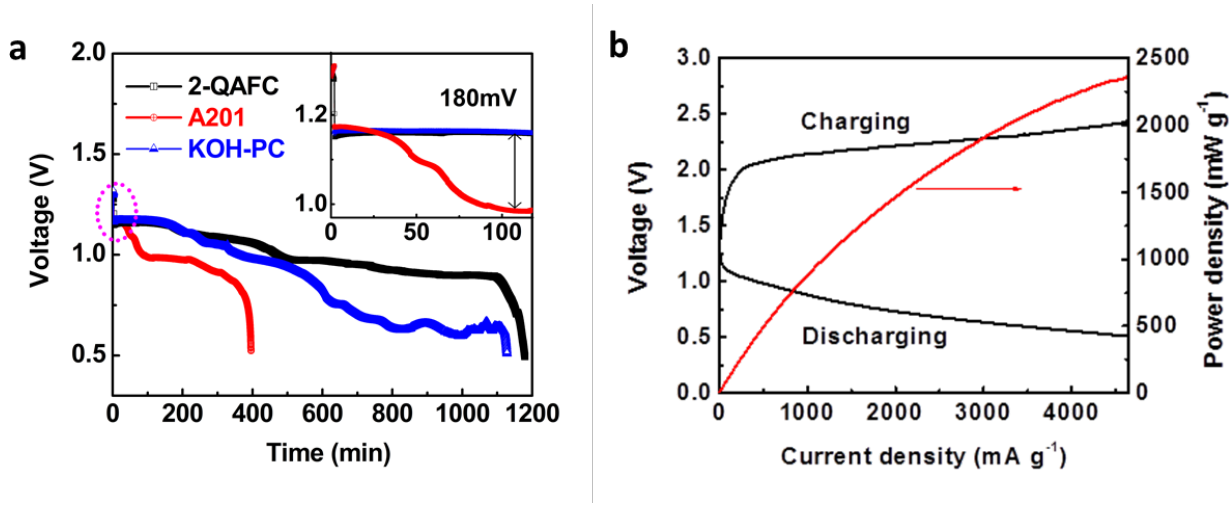

Figure 4-6. a) Galvanostatic discharge of the PEMZAB using the 2-QAFC, A201 and KOH-PC membranes at a current density of 25 mA g^{-1}. Inset shows an extended view of the red circle region at an initial 110 min. b) Charge and discharge polarization curves and corresponding power density plot of the battery using the 2-QAFC membrane.

Figure 4-7a further reveals the importance of bound water in affecting the battery cycling performance. During discharge, the membrane shrinks as water is consumed by the oxygen reduction reaction. Meanwhile, the membrane may undergo stress and deformation from the volume expansion of the zinc electrode due to the formation of oxidized zinc species. During charge, the membrane is gradually swollen as water is generated for the oxygen evolution reaction. In addition, the internal pressure caused by the generated oxygen bubbles and the formed zinc dendrites will lead to mechanical failure of the membrane. To further verify the overall physical and ion-transport properties of the QAFC membranes, galvanostatic charge and discharge cycling of the

batteries using the 2-QAFC and A201 membranes were conducted. The battery was cycled at a high current of 250 mA g^{-1} with each cycle being 60 min (25% depth of discharge) under atmospheric air. **Figure 4-7a** shows that the 2-QAFC membrane exhibited much longer cycle times with lower discharge and charge polarization than the commercial A201 membrane. The battery using the A201 membrane deteriorated noticeably after 720 min, showing large discharge and charge polarizations, whereas the battery using the 2-QAFC membrane exhibited much better cycling stability without the loss of performance in both the charge and discharge over 2100 min. This superior cycling stability indicates that the 2-QAFC membrane, holding a larger amount of water as well as a smaller anisotropic swelling, can tolerate the periodic stress and dehydration during the discharge and charge process, and thus facilitates hydroxide-ion access to the electrodes. This assumption was confirmed by similarity in electrochemical impedance spectroscopy (EIS) results of the 2-QAFC battery in the duration of each 60 min-cycle segment, where no significant changes in impedances was observed at designated intervals (10 min) for both the discharge and charge process (**Figure 4-7b, c**).

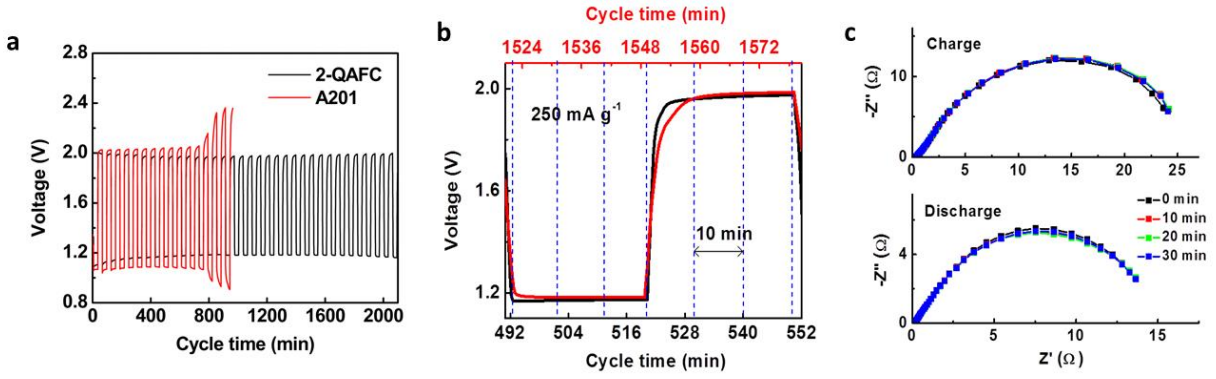

Figure 4-7. a) Galvanostatic charge and discharge cycling of the 2-QAFC and A201 membranes at a current density of 250 mA g-1 with a 60 min per cycle period. b) The

galvanostatic cycling plots of the 2-QAFC battery under a current density of 250 mA g-1, taken at two different 60 min-cycle segments and c) corresponding EIS spectra at designated time intervals (10 min).

Additionally, the uninhibited hydroxide-ion availability to the electrodes is evident from the good reversibility of the zinc electrode during repeated cycles, where the absence of a compact passivation layer of oxidized zinc species on the zinc electrode surface was observed (**Figure 4-8**). An SEM image of a zinc electrode prior to the cycling showing that it has a porous structure, in which zinc particles are well-distributed (**Figure 4-8a**). **Figure 4-8b** exhibits the morphology of the cycled zinc electrode. It shows that hollow, rod-shaped nanograins, with an average diameter of ~100 nm and about ~1 um in length, are partially deposited on the surface of zinc particles (**Figure 4-8c**). This observation is contrary to the well-known compact passivation layer of zinc oxide species, which prevent direct contact of hydroxide ions with remaining active zinc species, indicative of a good reversibility of a zinc electrode. The cycled zinc electrode was further identified by XRD (**Figure 4-8d**), as containing zinc, zinc hydroxide and zinc oxide species (Zn (JCPDS 04-0831); $Zn(OH)_2$ (JCPDS 38-0385); ZnO (JCPDS 036-1451)).

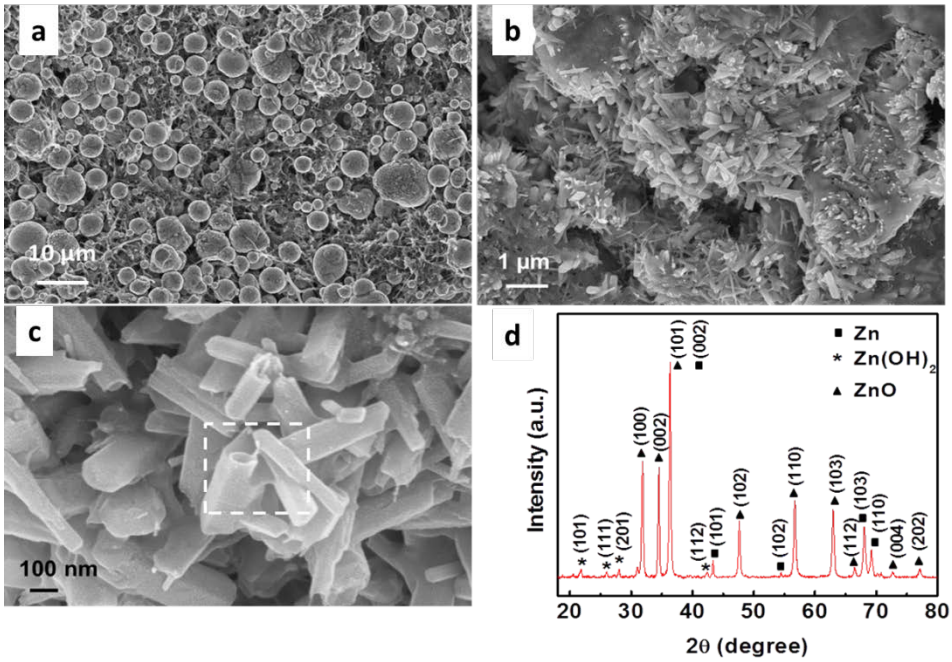

Figure 4-8. a) Fresh zinc electrode and b) cycled zinc electrode (finished by discharge). c) The high magnification SEM image of the square region of b, outlined in white. d) XRD pattern of the cycled zinc electrode. The battery using the 2-QAFC membrane was cycled at a current density of 250 mA g^{-1} with a 60 min per cycle period.

CO_2 contained in the air stream leads to the carbonation of the 2-QAFC membrane on reaction of the OH^- with CO_2. FTIR results (**Figure 4-3b**) also reveal the presence of carbonate in the 2-QAFC membrane. The effect of CO_2 on the cycling performance of the 2-QAFC battery was investigated. The galvanostatic discharge and charge of the 2-QAFC battery were performed using pure oxygen as reference, and the oxygen gas containing 20,000 ppm CO_2. The high CO_2 concentration (~50 times higher than that of air) in the mixture gas was used to enhance potential effects of the CO_2. The 2-QAFC batteries were initially operated at an open-circuit-voltage for two hours with flowing pure O_2 and 20,000 ppm CO_2 contaminated gas, respectively; then they were cycled under a current density of 250 mA g^{-1}. The galvanostatic cycling results under different

gas conditions are shown in **Figure 4-9a**. Compared to the pure O_2 condition, the initial higher polarization in the presence of CO_2 is likely related to increased ion (OH^- and CO_3^{2-}) transport resistances of the membrane. This effect correlates with the result that the membrane in CO_3^{2-} form has a smaller conductivity compared to that of the membrane in OH^- form (**Table 4-2**). Interestingly, for the first 420 minutes, the battery polarization was progressively smaller with each passing cycle (**Figure 4-9a**, inset). Additionally, after cycling over 420 min, only a slightly higher polarization was observed, compared to that of the battery cycled under pure O_2. The results suggest that the residual carbonate content in the 2-QAFC membrane was decreasing, and thus, the observed similarity in battery performance between the case of pure O_2 and CO_2/O_2 mixture after 420 min. It is possible that a high level of in situ "self-purging" process,[52] which has been previously reported in alkaline fuel cells, tends to occur at the air electrode, where OH^- anions are continuously generated through the oxygen reduction reaction under high current densities. Additionally, the increased pH environment will be beneficial for the reaction kinetics, which further improves the battery performance. EIS results (**Figure 4-9b**) reveal that the charge-transfer resistance (polarization resistance) of the battery, in the present of CO_2, decreased after 420 min (i.e., 2010th min) compared to that at the initial stage (i.e., 90th min). The drop in resistance, caused by continuous generation of OH^- with self-purging, indicates an improvement of the charge-transfer kinetics and a decrease of the resultant battery polarization.

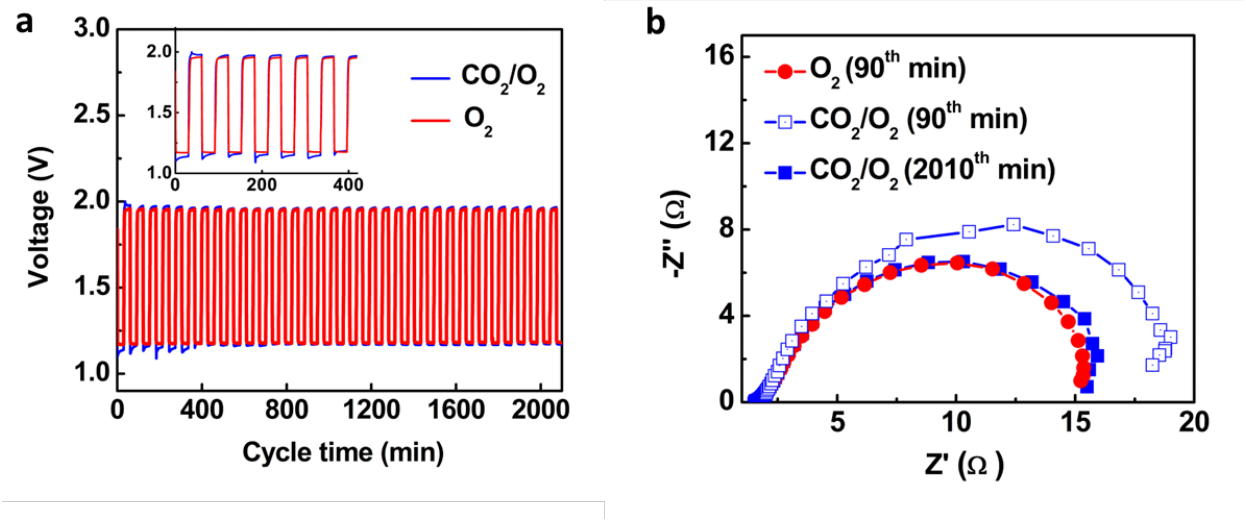

Figure 4-9. a) Galvanostatic charge and discharge cycling of the battery using pure oxygen and 20,000 ppm CO_2 contaminated gas reactants, respectively, at a current density of 250 mA g^{-1} with a 60 min per cycle period, b) corresponding Nyquist plots of the impedance of the battery at designated time segments. The inset of (e) showing an extended view of the first 420 min.

Table 4-2. Properties of the 2-QAFC membrane.

Anion type	Thickness [μm]	Water uptake [%]	σ [mS cm^{-1}]
OH^-	30	96.5	21.2
CO_3^{2-} [a)]	30	96.2	18.7

[a)] The membranes were exchanged to the CO_3^{2-} form by their immersion in a large excess of aqueous 1M K_2CO_3, and were thoroughly washed by water to remove the excess K_2CO_3.

A flexible device using the 2-QAFC membrane was demonstrated for a simple proof-of-concept (**Figure 4-10a**). Two flexible single cells (size 0.8 cm × 2.5 cm) were connected in series using a silver paste as an external circuit connection and fixed on the back side of a bandage. Here the bandage was used as a flexible and air-permeable substrate. As shown in **Figure 4-10b**, the device as prepared was thin and flexible

enough to be wrapped around a finger. Meanwhile, this device remained functional to power a red LED (light-emitting diode) when bent. To further understand the overall flexibility of the device, a single-cell device (size 1.0 cm × 2 cm) was fabricated onto a bendable nickel foam substrate to afford various bending conditions (**Figure 4-10c**). **Figure 4-10d** exhibits the output power density of the device as a function of current density under different angles. At any given angles, the power densities of the battery remained virtually unchanged under each different current density. Particularly, no significant power decay was detected even at an angle up to 120^{o} at a high current density of 3000 mA g^{-1}. The result indicates a robust physical property and high hydration level of the 2-QAFC membrane. The water can be held strongly by hydrogen bonds and capillary forces in hydrophilic nanopores of the 2-QAFC membrane, which does not restrict the hydroxide-ion conduction when the membrane was bended. The impedances of the 2-QAFC battery were further measured under atmospheric air within the frequency range from 0.05 Hz to 100 kHz. EIS spectra (Nyquist plots) of the 2-QAFC battery under various bending angles at a current density of 3000 mA g^{-1} are presented in **Figure 4-10e**. The battery resistance consists of three components: (1) a high-frequency incomplete arc mainly corresponds to OH^- transport behaviour (R_{int}) at the interface of the membrane and electrodes; (2) a medium-frequency semicircle represents a charge-transfer resistance (R_{ct}) in parallel to the electrode double layer capacitance; (3) a low-frequency tail is attributed to the mass transport limitations of reactants (i.e., oxygen, water, zinc species). The values of R_{int} exhibited minuscule changes even bending towards large angles (**Table 4-3**), indicating uninhibited OH^-

transport process between the membrane and the electrodes. Additionally, the R_{ct} values did not show significant variation with changes in bending angles (**Table 4-3**), which again reveals that the 2-QAFC membrane possesses high flexibility to precede the oxygen reduction reaction by strongly holding a large amount of water within its nanofibrous structure.

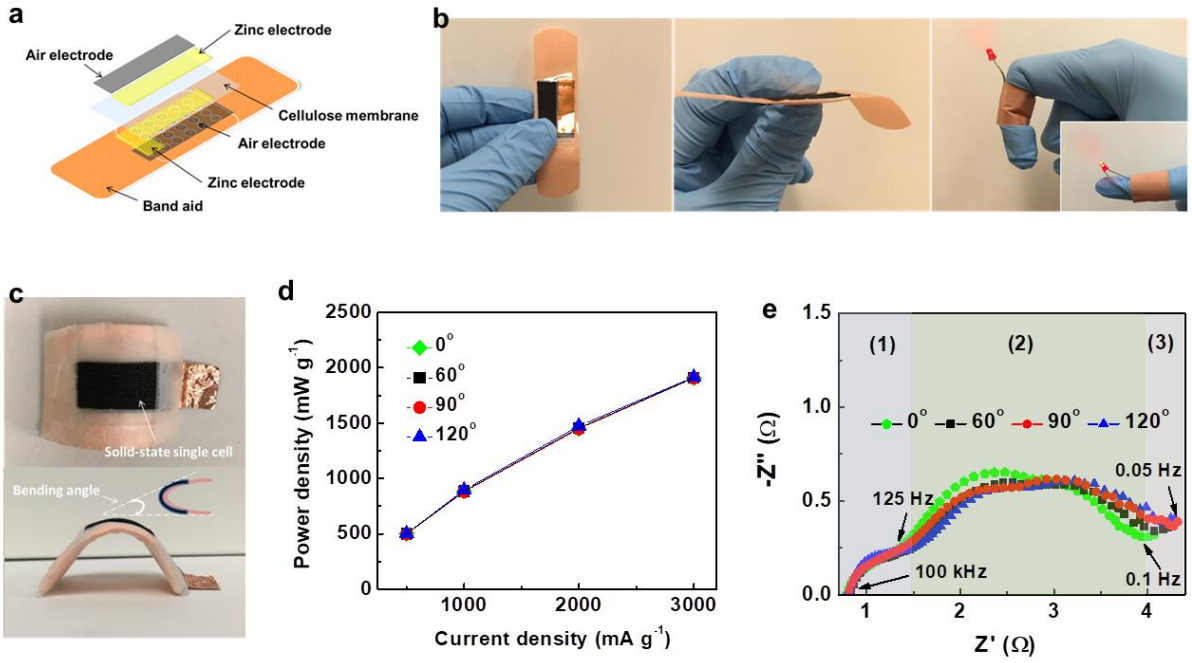

Figure 4-10. a) Schematic diagram of a flexible zinc-air battery device integrated with a bandage. b) A demonstration of the flexible device wrapped around an index finger to power a red LED under bending condition. c) Photographs of a single zinc-air cell device under the bending condition. d) Power densities of the single flexible cell as a function of current density at different bending angles. e) Nyquist plots of the battery measured at a current density of 3000 mA g^{-1} under different bending angles, within the frequency range from 0.05 Hz to 100 kHz.

Table 4-3. The values of the equivalent circuit [d)] elements based on the EIS analysis of the zinc-air battery.

Bending angle (^{o})	R_{ohm} [a)] (ohm)	R_{int} [b)] (ohm)	R_{ct} [c)] (ohm)
0	0.77	1.66	2.08
60	0.76	1.68	2.19
90	0.77	1.66	2.28
120	0.77	1.67	2.27

[a)]Ohmic resistance. [b)]Interfacial resistance. [c)]Charge-transfer resistance. [d)]The equivalent circuit of the battery during the discharge and charge process.

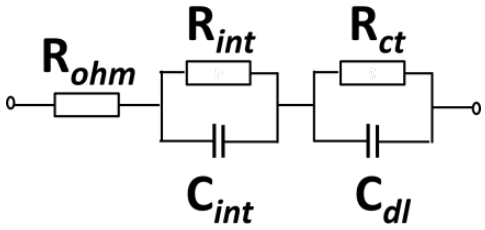

[d)]Equivalent circuit

4.4 Conclusions

In summary, a highly flexible and hydroxide ion-conductive electrolyte membrane, made of the functionalized cellulose nanofibres, was fabricated and utilized as both an electrolyte and a separator for the rechargeable PEMZAB. The superior ion conductive property and water retention within the nanoporous structure of the membrane as well as low anisotropic swelling boosted the specific capacity and improved the cycling stability of the battery, compared to the commercial alkaline anion-exchange membrane (A201). A flexible zinc-air battery device was created and further demonstrated the outstanding

electrochemical and mechanical performance of the membrane, where virtually no power density fading nor polarization of the battery were observed for the discharge and the charge process under bending conditions. With successful implementation of the QAFC electrolyte membrane, design of a high-performance bifunctional oxygen electrocatalyst that replaces the state-of-the-art Co_3O_4 nanoparticles will be examined in the next chapter.

Chapter 5 Bifunctional oxygen electrocatalyst based on a hybrid of cobalt oxysulfide nanocrystals and nitrogen-doped graphene nanomeshes

5.1 Introduction

A critical bottleneck limiting the performance of rechargeable zinc-air batteries lies in inefficient bifunctional electrocatalysts for oxygen reduction and evolution reactions at air electrodes. Currently, the best-known catalysts for oxygen electrocatalysis in alkaline solutions are platinum (Pt) group metals for ORR and iridium (Ir) group metal for OER.[135] Unfortunately, the widespread adoption of these noble metal catalysts is inevitably hindered by their insufficient catalytic-bifunctionality, little elemental abundance, and great cost.[173] The pursuit of low-cost alternatives based on earth-abundant transition metals is heading in a promising direction, enabling scalable implementation of zinc-air batteries.[82, 84] Among the various transition metal compounds, it is mainly the oxides that have been identified as potential bifunctional catalysts due to their chemical versatility and general stability under both ORR and OER conditions.[48, 133] Commonly, engineering the cationic metal composition of oxide electrocatalysts, such as spinel (*e.g.* $Co_xMn_{3-x}O_4$ [174] and $Mn_xCu_{1-x}Co_2O_4$[175]), pyrochlore (*e.g.* $Pb_2Ru_2O_{6.5}$[176]) and perovskite oxides (*e.g.* $Ba_{0.5}Sr_{0.5}Co_{0.8}Fe_{0.2}O_{3-\delta}$[177]), allows researchers to tune a balance between the catalytic activities for ORR and OER. Still, chemical instability of these oxides due to impurities, additive cation segregation and phase precipitation at the surface limits their electrochemical performance and stability.[178] In viewing of the extensive works on metal-oxide-based bifunctional electrocatalyst, engineering the anion chemistry of metal oxides to control their physicochemical properties and electrochemical performance has been less explored.[179-182] In this regard, partial oxygen (O) substitution of metal oxides with the same

chalcogen family of varying electronegativity and atomic radius to favorable defective structures would be an attractive solution to efficient oxygen electrocatalysis. Among the chalcogens, the combined size and electronegativity effects of the O and sulfur (S) are expected to be more significant to induce proper distorted structures and O defects, while still preserving the stability of the defective crystal form of oxides. Such effects make S appealing for the partial O substitution in altering the electronic structures and chemical properties of metal oxides and thus influencing their reactivity and stability for ORR and OER.

Furthermore, despite intensive work on optimizing catalytic activities, the actual performance of these developed powdery metal oxide catalysts become limited by their electrical conductivity, along with ineffective assembly on the air electrode.[183] In the case of the routine fabrication methods, powdery metal oxide catalysts must be loaded with carbon supports and polymer binders to retain the integrity of the air electrode and to improve the charge transfer during ORR on discharge and OER upon charging.[137, 184] However, the addition of binders within the air electrode would cause an inefficient utilization of the catalysts due to increased interfacial ohimic resistances of the electrode, thus driving the need for further advanced catalyst development to realize binder-free implementation for high-performance zinc-air battery applications.

In this chapter, I show an effective strategy combining of anion substitution, defect engineering and dopant effect to address the above two critical issues. I demonstrate this strategy on a hybrid catalyst consisting of cobalt oxysulfide single crystals and nitrogen-doped graphene nanomeshes ($CoO_{0.87}S_{0.13}$/GN). The defect chemistries of both oxygen-vacancy-rich, nonstoichiometric cobalt oxysulfides and edge-nitrogen-rich graphene nanomeshes lead to a

remarkable improvement in electrocatalytic performance, where $CoO_{0.87}S_{0.13}$/GN exhibits strongly comparable catalytic activity and much better stability to the best-known benchmark noble metal catalysts. Moreover, I demonstrate a simple, water-based filtration method for a direct assembly of the $CoO_{0.87}S_{0.13}$/GN catalyst and the QAFC electrolyte membrane, and investigate their performance on the PEMZAB.

5.2 Experimental Methods

5.2.1 Synthesis of $CoO_xS_{1.097}$/G

Graphene oxide (GO) was prepared by modified Hummer's method as described in my previous study.[8] In a typical synthesis, 50 mg of GO, 300 mg of thiourea and 24.8 mg of cobalt acetate tetrahydrate were well-dispersed in 10 mL of *N*, *N*-Dimethylformamide and 2 mL of deionized water through stirring and ultrasonication. The mixture was then transferred to a 23 mL Teflon-lined autoclave and the solvothermal synthesis was carried out by heating the mixture to 120 ^oC for holding 10 h, followed by another 10 h-heating at 220 ^oC. After 20 h, the as-synthesized product was thoroughly washed using acetone and deionized water and collected after lyophilization.

5.2.2 Synthesis of $CoO_{0.87}S_{0.13}$/GN, $CoOS_{600}$, $CoOS_{800}$, and GN

The conversion of $CoO_xS_{1.097}$/G into $CoO_{0.87}S_{0.13}$/GN, $CoOS_{600}$ or $CoOS_{800}$ was accomplished by ammonolysis at 700, 600 or 800 ^oC, respectively. In a typical synthesis of $CoO_{0.87}S_{0.13}$/GN, the as-prepared $CoO_xS_{1.097}$/G was annealed under NH_3 flow at 700 ^oC for 30 min with a heating rate of 3 $^oC\ min^{-1}$, yielding the final product of $CoO_{0.87}S_{0.13}$/GN. The

graphene nanomeshes (GN) were obtained from the acid-leaching of $CoO_{0.87}S_{0.13}$/GN in 2.0 M HCl at 80 ^{o}C for 8 h, followed by moderate thermal activation under argon at 700 ^{o}C for 10 min.

5.2.3 Fabrication of the PEMZAB

The preparations of the porous zinc film and nanoporous cellulose membrane were described in our previous work.[58] The binder-free and Nafion^{TM}-based $CoO_{0.87}S_{0.13}$/GN-coated cellulose membrane assembly (CMA) were fabricated by the filtration and spray-coating methods, respectively. For binder-free CMA, 4.0 mg of $CoO_{0.87}S_{0.13}$/GN was well-dispersed in 200 mL of deionized water, and the homogenous suspension was coated on a surface of the cellulose membrane (2.0 cm^{-2}), with a catalyst loading of 2.0 mg cm^{-2} by the filtration. For Nafion^{TM}-based CMA, catalyst ink comprised of $CoO_{0.87}S_{0.13}$/GN, Nafion^{TM} ionomer and ethanol was sprayed onto the surface of the cellulose membrane with the same active surface of 2.0 cm^{-2} and a catalyst loading of 2.0 mg cm^{-2}. For the freestanding catalyst film shown in Figure 1a, 3.0 mg of $CoO_{0.87}S_{0.13}$/GN and 1.0 mg of multi-wall carbon nanotubes (Timesnano, MFG Code M3/50107) were well-dispersed in 200 mL of deionized water, and the mixture was filtered using a Nylon membrane (0.2 μm pore size, Whatman). The solid-state zinc-air battery was fabricated through layer-by-layer method, where the zinc film and gas diffusion backing layers were placed face-to-face with the CMA. The CMA was pre-wetted by 6 M KOH solution before battery assembly. Stainless steel meshes were used as current collectors for both the zinc and air electrodes.

5.2.4 Material characterizations

The morphology of materials and structure were imaged by transmission electron microscopy (TEM; JEOL, JEM-2010, 200 kV). Electron energy loss spectroscopy (EELS) and electron energy-loss near-edge structure (ELNES) were performed with a FEI Titan 80-300 HB operated at 200 kV. Powder X-ray diffraction (XRD; Bruker AXS D8 Advance) patterns and X-ray photoelectron spectroscopy (XPS; Thermal Scientific K-Alpha XPS spectrometer) were recorded to analyze crystal structure and surface chemistry. A surface area and porosity analyzer (Quantachrome Instruments QuadraSorb SI4) was used to obtain nitrogen adsorption-desorption isotherm to determine Brunauer-Emmett-Teller (BET) surface area, and the Barrett-Joyner-Halenda (BJH) model was used to obtain pore size distribution.

5.2.5 Electrochemical measurements

The electrocatalytic performance of oxygen reduction and evolution reactions was measured by a rotating disc electrode in a three-electrode cell at room temperature. The three-electrode system contains glassy carbon electrode (GC; 5 mm in diameter), graphite rod, and reversible hydrogen electrode (RHE) as the working, counter and reference electrodes, respectively. The catalyst ink was prepared by mixing 4 mg of the catalyst in 980 µL of ethanol containing 20 µL of 2.5 wt% Nafion^{TM} dispersion, followed by ultrasonication for 1 h to obtain a homogeneous ink. Then 20 µL of the as-prepared ink was dropped onto the GC surface to give a catalyst loading of 0.36 mg cm^{-2} for all the developed catalysts. Commercial Pt/C (28.8 wt. % Pt) and Ir/C (20 wt. % Ir) catalysts were used as reference materials and their catalytic performance were optimized with a catalyst loading of 0.2 mg cm^{-2}. All measurements were carried out in a 0.1 M KOH solution, where O_2 and N_2 gas were purged for 20 min before ORR

and OER measurements, respectively. The linear sweep voltammetry measurements were performed from 1.0 to 0.1 V vs. RHE at a different rotation speed for ORR and from 1.0 to 1.8 V vs. RHE at 900 rpm of rotation speed for OER at a scan rate of 5 mV s^{-1}. ORR and OER polarization curves were corrected by IR-compensation in 0.1 M KOH solution, where the resistance (28.5 ohm) is determined from the high-frequency intercept of Nyquist plots acquired from electrochemical impedance spectroscopy (EIS). Capacitive background currents were subtracted for ORR and OER polarization curves during cyclic voltammetry (CV) measurements in N_2-saturated KOH solution. Stability tests were carried out using CV between 0.6 and 1.7 V in O_2-saturated 0.1 M KOH solution at 50 mV s^{-1}. Battery performance was measured under ambient conditions in atmospheric air. Polarization curves were recorded using the galvanodynamic method at a scan rate of 2.0 mA s^{-1}. For specific capacity measurement, galvanostatic discharge was conducted at a current density of 10 mA cm^{-2} with a cut-off voltage of 0.9 V. Galvanostatic discharge and charge cycling was performed by a recurrent galvanic pulse method at a current density of 20 mA cm^{-2} with 1 h cycle. EIS was performed in the frequency range of 100 kHz to 0.1 Hz with a potential amplitude of 50 mV.

5.3 Results and Discussions

I have designed a bifunctional oxygen electrocatalyst comprised of S-deficient cobalt oxysulfide ($CoO_{0.87}S_{0.13}$) single crystals rooted at nitrogen (N)-doped graphene nanomeshes ($CoO_{0.87}S_{0.13}$/GN), which can be readily fabricated into a catalyst film for direct use in the zinc-air battery (**Figure 5-1a**). The hybrid catalyst was derived from a physicochemical evolution of an oxidized $CoS_{1.097}$ nanoparticles/graphene composite using an ammonia-enhanced post treatment. The ammonolysis not only enables the formation of O-vacancy-rich,

nonstoichiometric $CoO_{0.87}S_{0.13}$ nanoparticles without inducing a secondary phase, but also creates edge-nitrogen-rich graphene nanomeshes (GN). The resulting GN play a vital role in not only allowing intimate electronic contact with $CoO_{0.87}S_{0.13}$ nanoparticles but in also providing adequate open space and short diffusion channels for reactants and intermediates during ORR and OER (**Figure 5-1b**). This character could greatly facilitate both rapid charge transfers and mass transport in comparison to non-porous graphene supported catalysts (**Figure 5-1c**), consequently promote reaction kinetics.[185, 186]

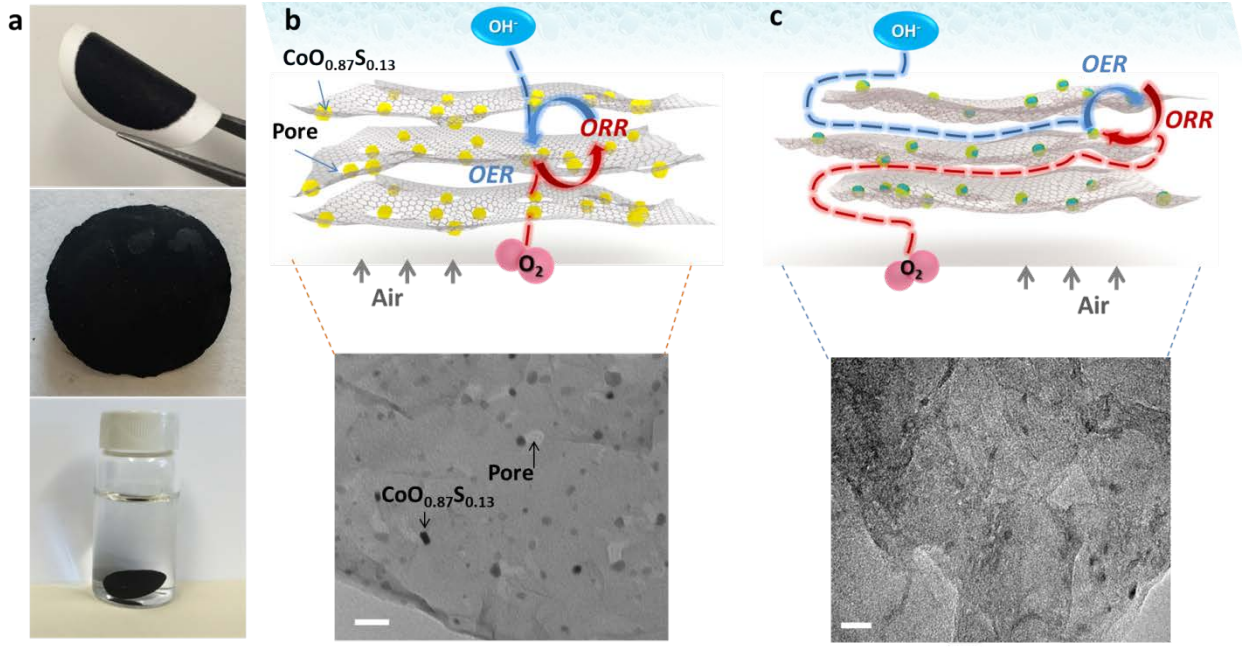

Figure 5-1. a) Photographs of the $CoO_{0.87}S_{0.13}$/GN catalyst film on a Nylon filter membrane and soaked in water. b,c) Schematic of $CoO_{0.87}S_{0.13}$ nanoparticles rooted at porous graphene nanomeshes (b) and non-porous graphene (c) with corresponding TEM images.

$CoO_{0.87}S_{0.13}$/GN was prepared by the ammonolysis of the as-synthesized oxidized cobalt sulfide precursors, as illustrated in **Figure 5-2a**. First, oxidized cobalt sulfide nanoparticles supported on N-doped graphene were synthesized by a solvothermal method. The transmission

electron microscopy (TEM) image in **Figure 5-2b** shows the amorphous like periphery of these cobalt sulfide nanoparticles. The fast Fourier-transformed (FFT) patterns of the marked region (Figure 5-2b inset) disclose the existence of nanocrystalline phases. The FFT pattern of the selected area of an individual particle (**Figure 5-2c**) and the lattice spacing (2.89 Å) of the crystal reveal a hexagonal structure, in accordance with the (204) plane of $CoS_{1.097}$ phase shown in the X-ray diffraction (XRD) analysis (**Figure 5-2d**).

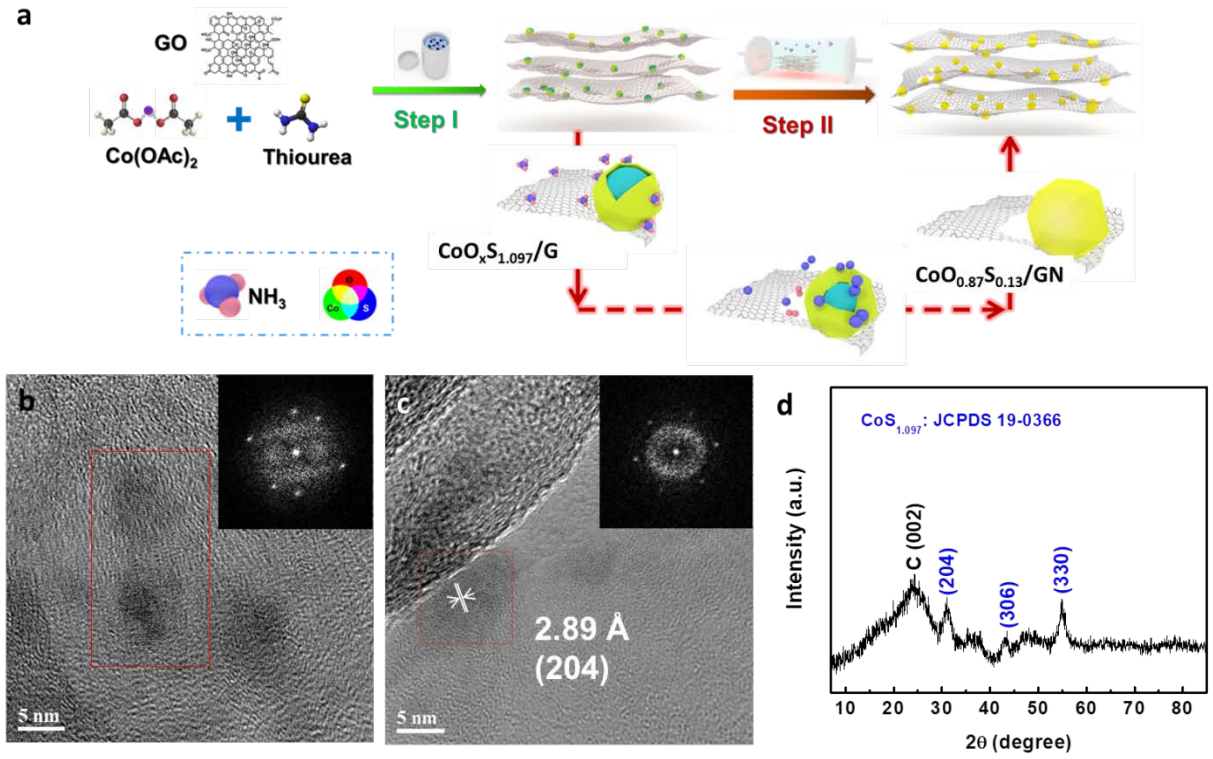

Figure 5-2. a) Schematic illustration of the synthesis of $CoO_{0.87}S_{0.13}$/GN. b) TEM image of $CoO_xS_{1.097}$/G with corresponding FFT diffraction pattern of the selected area. c) High-resolution TEM image of $CoO_xS_{1.097}$/G with corresponding FFT diffraction pattern of the selected area of an individual nanoparticle. d) XRD pattern of $CoO_xS_{1.097}$/G.

Electron energy loss spectroscopy (EELS) elemental maps (**Figure 5-3a**) of a

$CoO_xS_{1.097}$ nanoparticle explicitly reveal a cobalt sulfide core and an oxidized shell. In the second step of the catalyst preparation, the oxidized cobalt sulfide precursor (referred to as $CoO_xS_{1.097}$/G) was converted into $CoO_{0.87}S_{0.13}$/GN under flowing NH_3 gas at 700 ^oC for 30 min. This ammonolysis process induced unprecedented atomic reconstructing in the nanoparticles as well as a new graphene nanostructure. The XRD pattern of $CoO_{0.87}S_{0.13}$/GN reveals the absence of the hexagonal $CoS_{1.097}$ phase (**Figure 5-3b**). Instead, its diffraction pattern can be indexed to the face-centered cubic CoO phase (Joint Committee on Powder Diffraction Standards, JCPDS 70-2855), shifted slightly to lower diffraction angles (**Figure 5-3c**). Such a shift suggests a slight lattice expansion of the crystal lattice, which could result from the incorporation of the larger S element into the CoO structure. EELS spectra of $CoO_{0.87}S_{0.13}$/GN identify the presence of Co, O and S in the nanoparticle in an estimated elemental composition of $CoO_{0.87}S_{0.13}$ (**Figure 5-3d**). Additionally, by considering as elements of interest the Co ($L_{2,3}$-edge), S (L-edge), and O (K-edge), EELS elemental maps of a $CoO_{0.87}S_{0.13}$ nanoparticle (**Figure 5-3e**) and the corresponding line profile (**Figure 5-3f**) clearly demonstrates that S distributes homogeneously throughout the nanoparticle and overlaps with Co and O elements, thus confirming the $CoO_{0.87}S_{0.13}$ nanoparticles consist of a single solid phase.

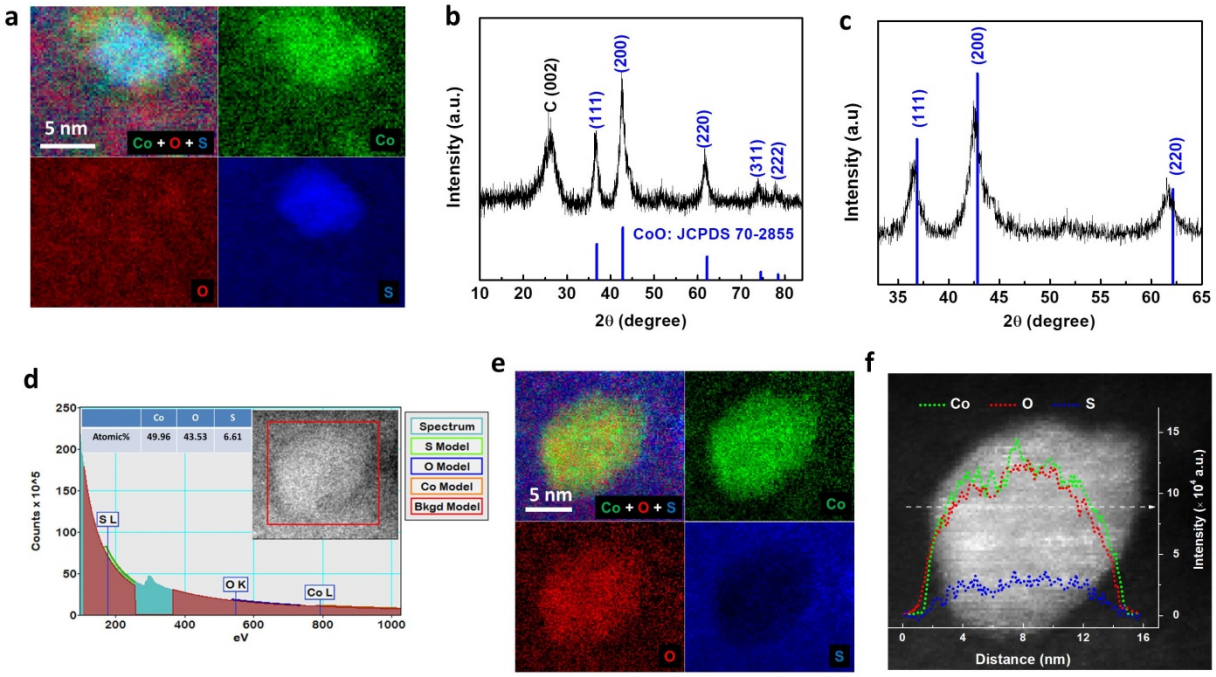

Figure 5-3. a) Aberration-corrected EELS elemental mapping for $CoO_xS_{1.097}$/G. b) XRD pattern of $CoO_{0.87}S_{0.13}$/GN. c) Selected XRD pattern of the (111), (200) and (220) diffraction peaks for $CoO_{0.87}S_{0.13}$/GN. These peaks all shift slightly to lower diffraction angles. d) EELS spectrum for $CoO_{0.87}S_{0.13}$/GN. The atomic composition of Co, O and S is determined by the compositional analysis of the EELS spectrum using Gatan Microscopy Suite Software. e,f) Aberration-corrected EELS elemental mapping (e) and the corresponding EELS line profile (f) of $CoO_{0.87}S_{0.13}$/GN.

Figure 5-4a shows evidence of the formation of pores in the graphene associated with neighboring $CoO_{0.87}S_{0.13}$ nanoparticles. This new feature is further corroborated in the TEM image of the acid-leached $CoO_{0.87}S_{0.13}$/GN (**Figure 5-4b**), appearing as a highly porous nanostructure with an estimated average pore width of 16 nm which can be classified as graphene nanomeshes (GN). Nitrogen sorption isotherms of both $CoO_{0.87}S_{0.13}$/GN and GN exhibit type-IV hysteresis loops (**Figure 5-4c**), confirming the mesoporous structure of graphene. Pore width analysis with the Barrett-Joyner-Halenda (BJH) method discloses that

$CoO_{0.87}S_{0.13}$/GN has a relatively broad mesopore distribution, ranging from 4 to 20 nm. In contrast, the isotherms of $CoO_xS_{1.097}$/G rarely show a distinguishable hysteresis loop due to its non-porous graphene structure. Both $CoO_{0.87}S_{0.13}$/GN and GN have much larger Brunauer-Emmett-Teller (BET) specific-surface-areas of 265.57 and 495.16 $m^2 g^{-1}$, respectively, than that of $CoO_xS_{1.097}$/G (120.64 $m^2 g^{-1}$). Scanning TEM-EELS maps in **Figure 5-4d** exhibit a uniform distribution of N (K-edge) encircling the pore edge of GN, indicative of spontaneous N decoration of pore edges during the ammonolysis. This decoration was verified with X-ray photoelectron spectroscopy (XPS) (**Figure 5-4e**), wherein $CoO_{0.87}S_{0.13}$/GN was observed to accommodate more N dopants (2.59 atomic%) than $CoO_xS_{1.097}$/G (1.47 atomic%). High-resolution N 1*s* XPS spectra (**Figure 5-4f**) further reveal that increases in pyridinic-N (398.2 eV) and graphitic-N (401.6 eV) fractions contribute to the higher content of N-doping in $CoO_{0.87}S_{0.13}$/GN as compared with $CoO_xS_{1.097}$/G. Altogether, the enrichment of topological defects generated by N-doping along the pore edges in graphene is anticipated to boost the catalytic performance of $CoO_{0.87}S_{0.13}$/GN.[78, 187] It is worth pointing out that despite the pore formation, $CoO_{0.87}S_{0.13}$ nanoparticles are firmly rooted at the GN surface through intimate covalent bonds between Co and N (Co-N_x, 399.6 eV),[188, 189] as evident by XPS N 1s spectra (**Figure 5-4g**).

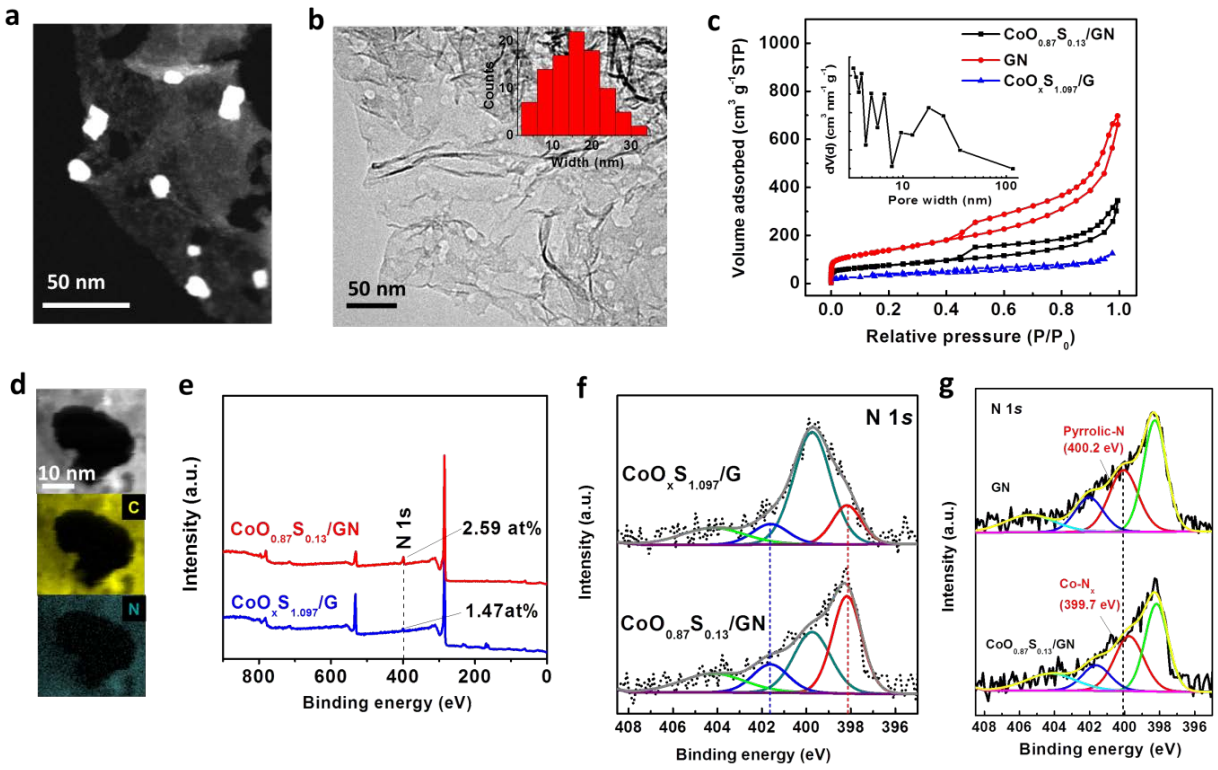

Figure 5-4. a) Scanning TEM image of $CoO_{0.87}S_{0.13}$/GN. b) TEM image of the porous graphene nanomeshes (GN) after acid-leaching $CoO_{0.87}S_{0.13}$ nanoparticles (inset: a histogram of the pore size distribution). c) N_2 adsorption-desorption isotherms and pore-size distribution (the inset) for $CoO_xS_{1.097}$/G, $CoO_{0.87}S_{0.13}$/GN and GN. d) STEM-EELS elemental mapping of the N-decorated pore edge of GN. e) XPS spectra of $CoO_xS_{1.097}$/G and $CoO_{0.87}S_{0.13}$/GN. f) High-resolution XPS N1s spectra of $CoO_xS_{1.097}$/G and $CoO_{0.87}S_{0.13}$/GN. g) XPS N1s spectra for $CoO_{0.87}S_{0.13}$/GN and GN. The peak at 399.7 eV (Co-N_x) disappeared after acid-leaching of $CoO_{0.87}S_{0.13}$ nanoparticles, accompanying by the formation of a new peak at 400.2 eV (pyrrolic-N) in GN.

The formation of $CoO_{0.87}S_{0.13}$/GN with the featured compositional and structural properties was controlled by the homogenous reduction and recrystallization of the starting $CoO_xS_{1.097}$/G material at 700 ^oC for 30 min under NH_3. Indeed, the ammonolysis of $CoO_xS_{1.097}$/G at different temperatures (*i.e.* 600 and 800 ^oC) led to nanoparticles of varying

anion compositions and crystal phases as well as different graphene nanostructures. To trace the physicochemical evolution of $CoO_{0.87}S_{0.13}$/GN, I further characterized the morphology, composition and crystal structure of the 600 ^{o}C (labeled as $CoOS_{600}$), 700 ^{o}C (*i.e.* $CoO_{0.87}S_{0.13}$/GN) and 800 ^{o}C (labeled as $CoOS_{800}$) samples. At 600 ^{o}C, the starting material of $CoO_xS_{1.097}$/G was partially converted to CoO. XRD analysis of the $CoOS_{600}$ sample confirms the coexistence of cubic CoO and hexagonal Co_9S_8 phases (**Figure 5-5a**). High-resolution TEM imaging (**Figure 5-5b,c**) and EELS elemental maps (**Figure 5-5d**) further identify the core-shell structure of the nanoparticle to be composed of a Co_9S_8 core with a CoO shell, consistent with the XRD result.

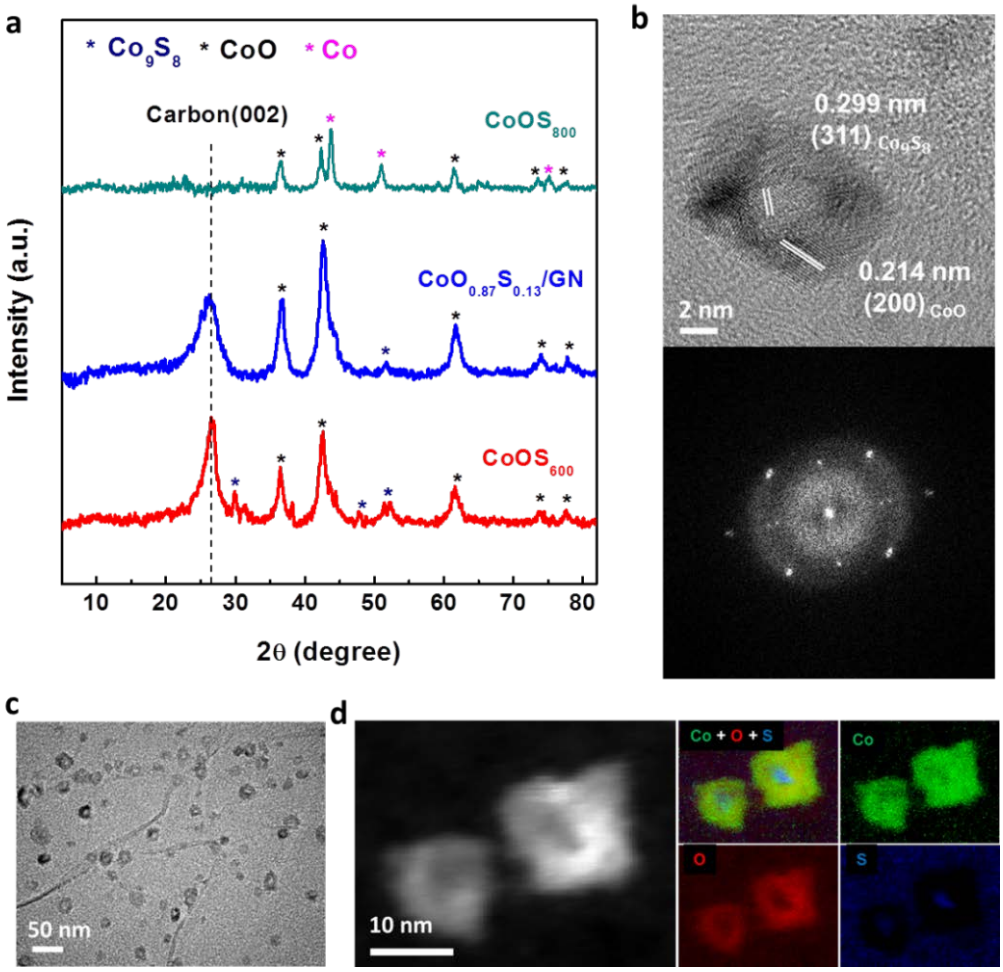

Figure 5-5. a) XRD patterns for $CoOS_{600}$, $CoO_{0.87}S_{0.13}$/GN and $CoOS_{800}$. b) High-resolution TEM image and corresponding FFT patterns of $CoOS_{600}$. c) TEM image of $CoOS_{600}$. d) Scanning TEM-EELS elemental mapping for $CoOS_{600}$.

At a higher temperature of 700 ^{o}C, the absence of the core-shell nanoparticles and etchings of graphene are distinguishable (**Figure 5-6a**). Moreover, the high-resolution TEM image and corresponding fast Fourier transformation (FFT) diffraction pattern indicate single crystallinity of the nanoparticle. The interplanar spacings of the (200) and (111) planes increase to 0.214 and 0.248 nm, respectively, as compared with that of the pure CoO phase (JCPDS 70-2855; 0.211 and 0.244 nm, respectively). The result signals S doping into the lattice structure of

CoO, which is in good agreement with the observation from XRD in **Figure 5-3b**. Additionally, it is worth noting that annealing $CoO_xS_{1.097}$/G under an argon atmosphere at 700 ^oC yields non-porous graphene structure (**Figure 5-6b**). Thus, the pore formation is likely to happen through an *in situ* Co-catalyzed gasification of carbon to methane ($C_{graphene} + NH_3 \rightarrow CH_4 + N_2$) accompanying by NH_3 decomposition.[187] Further elevating the reaction temperature to 800 ^oC results in the coexistence of crystallized CoO and Co phases (**Figure 5-6c** and **Figure 5-5a**) and significantly increases the particle size (**Figure 5-6d**). The particle also appears as a core-shell structure (**Figure 5-6c**). The Co core and the CoO shell structure was determined by EELS elemental mapping (**Figure 5-6e**). On the basis of the above characterizations, I hypothesize that the high reducing environment of NH_3 thermodynamically favors the reduction of $CoO_xS_{1.097}$/G by selectively removing S over O with a subsequent lattice reconstruction to cubic CoO due to its relatively small formation energy.[174, 190] Meanwhile, this reconstruction is presumably accompanied with doping S into the CoO lattice. The substitution can be realized by removal of O from the lattice and diffusion of S to O defective sites during the ammonolysis. It is probable that S dopants in the CoO domain either partially substitute for the lattice O as interstitial defects or occupy the defective O vacancies in the cubic phase, or both. In influencing the local electronic environment of the Co-host structure by the generation of the lattice defects, an optimal S substitution is prone to induce additional catalytic active sites and thus improve the kinetics of ORR and OER.

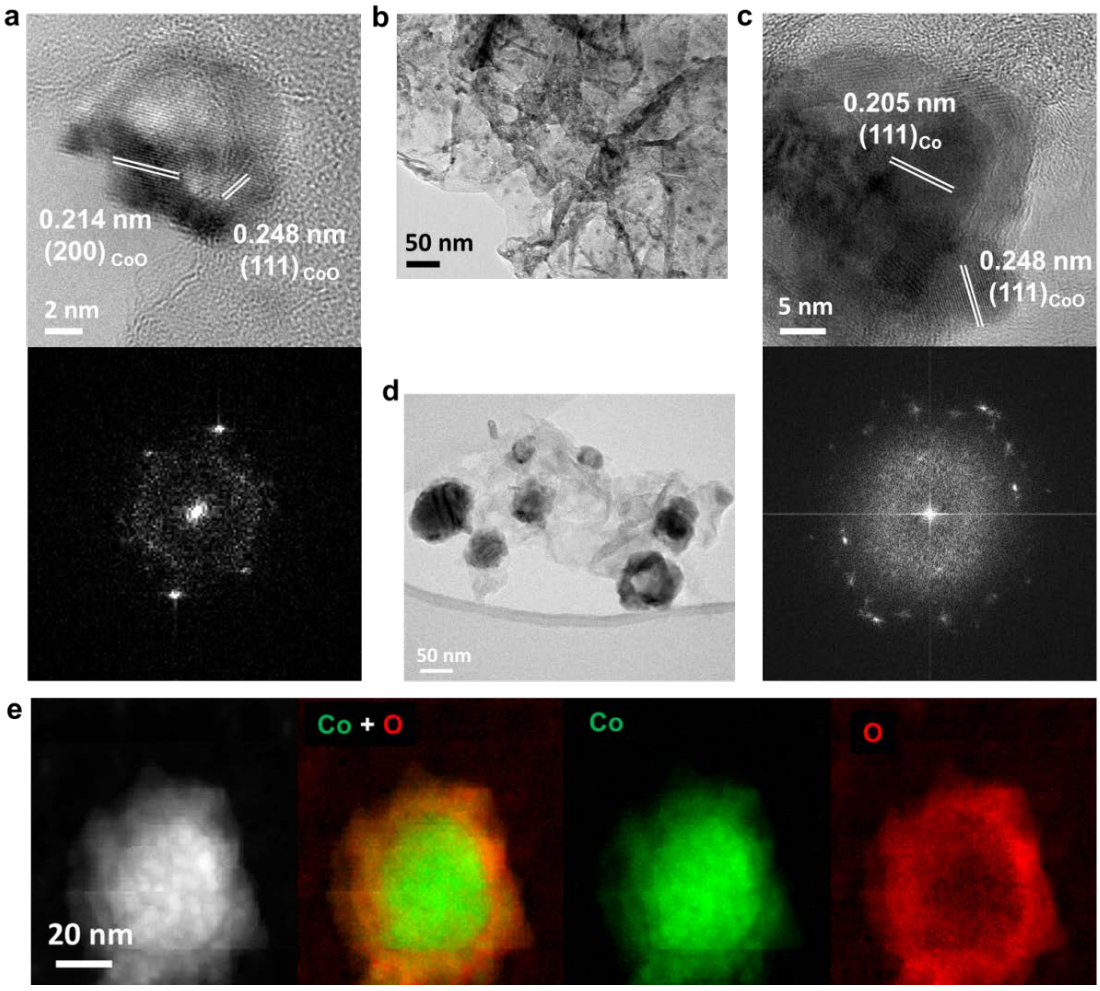

Figure 5-6. a) High-resolution TEM image and corresponding FFT patterns of $CoO_{0.87}S_{0.13}$/GN. b) TEM image of the sample after annealing $CoO_xS_{1.097}$/G under Ar at 700 ^oC for 30 min. c) High-resolution TEM image and corresponding FFT patterns of $CoOS_{800}$. d) TEM image and e) corresponding scanning TEM-EELS elemental mapping for $CoOS_{800}$.

The defective nature of $CoO_{0.87}S_{0.13}$/GN was probed using XPS and electron energy loss near-edge structure (ELNES) spectroscopy. **Figure 5-7a** shows high-resolution XPS O1*s* spectra for $CoOS_{600}$, $CoO_{0.87}S_{0.13}$/GN, and $CoOS_{800}$ samples. The peaks at ~530.1 eV correspond to the lattice O (O^{2-}) arising from Co-O bonds, and the peaks at ~531.2 eV are assigned to the defective O (O_2^{2-}).[191] The peak intensity ratio of the lattice O^{2-} to the defective

O_2^{2-} clearly increases from $CoOS_{600}$ to $CoOS_{800}$ (i.e. peak area ratios are 0.98, 1.07 and 1.29 for $CoOS_{600}$, $CoO_{0.87}S_{0.13}$/GN and $CoOS_{800}$, respectively), indicating diminishing O vacancies in the lattice structure. The relative decrease of O vacancies is further corroborated by the peak shift in Co 2*p* core level XPS spectra towards higher binding energy from $CoOS_{600}$ to $CoOS_{800}$ (**Figure 5-7b**), due to less probability of electron transfer from O vacancies to the Co 3*d* band, which results in a more oxidized Co valence.[192] Additionally, the relative reduction in O vacancies is in line with the lowering of S dopants from $CoOS_{600}$ to $CoOS_{800}$ (**Figure 5-7c**), implying the strong correlation between the negatively charged S dopants and the positively charged O vacancy defects through electrostatic attraction force.[178] This relationship is further evident from the fact that the stronger electrostatic driving force for $CoOS_{600}$ associated with high O vacancies caused the S enrichment and phase separation into core-shell nanoparticles (Co_9S_8/CoO), instead of a single solid phase. Furthermore, core-loss O *K*-edge and Co $L_{2,3}$-edges near-edge spectra acquired from these three samples and the pure CoO are shown in **Figure 5-7d**. In O *K*-edge spectra, two prominent peaks centered at ~530.6 and ~542.2 eV are observed for all the samples. The former corresponds to the pre-edge peak, arising from the O 2*p* in unoccupied states hybridized with Co 3*d* orbitals.[193] The latter is attributed to the O 2*p* character hybridized with the weakly structured Co 4*sp* band.[193, 194] It was previously demonstrated that the pre-edge structure is a sensitive indicator of the O vacancies.[178, 195] From the O *K*-edge spectra, the pre-edge peak becomes more prominent from $CoOS_{600}$ to $CoOS_{800}$, revealing the enhanced Co 3*d*-O 2*p* hybridization (covalency) by a lowering of O vacancies in samples.[196] The Co $L_{2,3}$-edges for the three samples show a similar white line-shape to that of the reference CoO, with an intense L_3 edge assigning to Co2$p_{3/2}$ and a weakened L_2 edge

corresponding to Co2$p_{1/2.}$[197] Comparing the peak positions of Co $L_{2,3}$-edges, however, a small shift of the Co L_3 peak maximum to a higher energy loss (~0.9 eV) is observed as an expected decrease of O vacancies, while the Co L_2 peak maximum remains relatively unchanged in all samples. The Co L_3-edge is more sensitive to the local environment than the Co L_2-edge with the change in the Co valence states and the degree of Co-O hybridization.[196, 198, 199] This shift is in good agreement with the trend observed for O pre-edge features and the peak shift in Co 2*p* core level XPS spectra towards higher binding energy (**Figure 5-7b**). Collectively, the above experimental evidences reveal that both the O vacancies and Co-O hybridization as an effective means for defect engineering are significantly influenced by the degree of S doping.

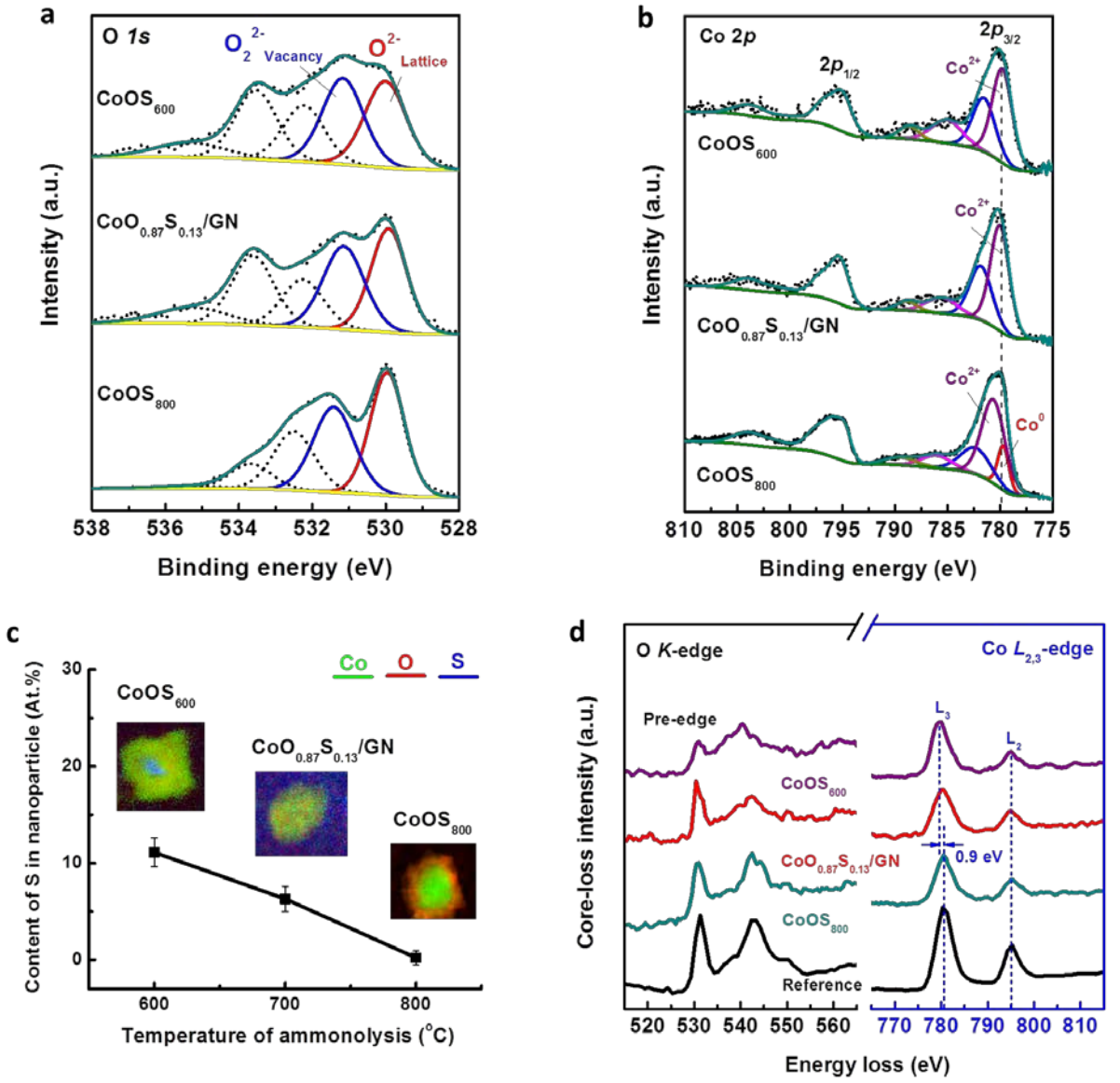

Figure 5-7. a) High-resolution XPS O 1s spectra of $CoOS_{600}$, $CoO_{0.87}S_{0.13}$/GN, and $CoOS_{800}$ samples. b) Co 2p core level XPS spectra for $CoOS_{600}$, $CoO_{0.87}S_{0.13}$/GN and $CoOS_{800}$. c) A comparison of S content for $CoOS_{600}$, $CoO_{0.87}S_{0.13}$/GN and $CoOS_{800}$. d) ELNES of the O K-edge and Co $L_{2,3}$-edges for $CoOS_{600}$, $CoO_{0.87}S_{0.13}$/GN, $CoOS_{800}$, and pure CoO.

One significant effect on oxygen electrocatalysis associated with the O vacancies and covalent mixing of Co-O is the increase of defect states near the Fermi level, which promotes

the injection/extraction of electrons from O_2 and assures fast exchange kinetics of O^{2-}/OH^- for enhanced ORR and OER reactivity.[176, 196] To draw correlations between the defective structures and electrocatalytic performance for ORR and OER, rotating disk electrode voltammetry measurements for $CoO_xS_{1.097}$/G, $CoOS_{600}$, $CoO_{0.87}S_{0.13}$/GN and $CoOS_{800}$ electrodes were performed. **Figure 5-8a** shows *iR*-compensated ORR polarization curves of various electrodes at 900 r.p.m. in an O_2-saturated 0.1 M KOH solution. $CoO_{0.87}S_{0.13}$/GN exhibits a typical sigmoid-shaped wave with a flat mass-transport limiting current plateau in the potential window studied. By comparison, the shapes of the sigmoidal wave for the $CoO_xS_{1.097}$/G, $CoOS_{600}$ and $CoOS_{800}$ electrodes are stretched out towards less positive potentials, indicative of a larger overpotential due to slow ORR kinetics. Evidently, $CoO_{0.87}S_{0.13}$/GN surpasses others in terms of more positive onset potential (E_{onset}; 0.94 V versus reversible hydrogen electrode (RHE), determined as the potential at 0.1 mA cm^{-2}) and half-wave potential ($E_{1/2}$; 0.83 V), as well as larger absolute value of the limiting current at a potential of 0.7 V ($j_{E=0.7}$; 4.12 mA cm^{-2}). **Figure 5-8b** shows six sets of ORR voltammetry curves of $CoO_{0.87}S_{0.13}$/GN at different rotating speeds and the corresponding Koutecky-Levich (K-L) plots (the inset of Figure 4b). The number of electrons transferred per oxygen molecule (*n*) can be estimated from the slopes of linear-fitted K-L plots, in which lower *n* values indicate inferior ORR selectivity. The result (the inset of Figure 5-8b) implies an apparent quasi-four-electron reduction of oxygen to OH^- on $CoO_{0.87}S_{0.13}$/GN. Regarding the OER performance, the overpotential for water electrolyzers at a current density of 10.0 mA cm^{-2} (referred to as $\eta_{j=10}$) is a metric to assess OER activity commonly.[200] **Figure 5-8c** shows *iR*-compensated OER polarization curves of all the electrodes. $CoO_{0.87}S_{0.13}$/GN manifests the highest catalytic activity for OER, requiring the lowest $\eta_{j=10}$ of

357 mV than that of the 600 ^{o}C (390 mV), 800 ^{o}C (431 mV) and $CoO_xS_{1.097}$/G (431 mV) electrodes. Besides, $CoO_{0.87}S_{0.13}$/GN shows the smallest Tafel slope (105 mV dec^{-1}) relative to those of $CoO_xS_{1.097}$/G (263mV dec^{-1}), $CoOS_{600}$ (123 mV dec^{-1}) and $CoOS_{800}$ (246 mV dec^{-1}) (**Figure 5-8d**), indicating that OER kinetics were the fastest on $CoO_{0.87}S_{0.13}$/GN. **Figure 5-8e,f** further show that the $CoO_{0.87}S_{0.13}$ particle can retain its crystal and chemical structures with respect to anodic polarization upon OER, an indication that the cobalt oxysulfide remains an inherent part of the active catalyst for OER. **Figure 5-8e** shows that the particles well retained their crystalline structure with the lattice spacing (2.84 Å), in consistent with the (111) plane of the cubic CoO, while the EELS mappings (**Figure 5-8f**) show that S remained a part of the polarized particle, in addition to Co and O. To further elucidate the bifunctional activity, potential differences between the $E_{1/2}$ of ORR and $E_{j=10}$ of OER ($\Delta E = E_{j=10} - E_{1/2}$) are presented in **Figure 5-8g**. The thermodynamic potential ($E_o(OH^-/O_2)$ =1.23 V) is used as the reference to reflect each overpotential with respect to ORR and OER. $CoO_{0.87}S_{0.13}$/GN exhibits not only the smallest ΔE of 0.76 V but also the lowest overpotential towards both ORR and OER among all the electrodes studied, indicative of the highest catalytic bifunctionality of $CoO_{0.87}S_{0.13}$/GN. The result reveals that $CoO_{0.87}S_{0.13}$/GN provides the most favorable balance between O vacancy defects and Co-O hybridization, whereas neither higher density of O vacancies in $CoOS_{600}$ nor stronger Co-O hybridization in $CoOS_{800}$ leads to the fastest ORR and OER kinetics, consistent with published theoretical predictions and experimental results.[178, 192, 201, 202]

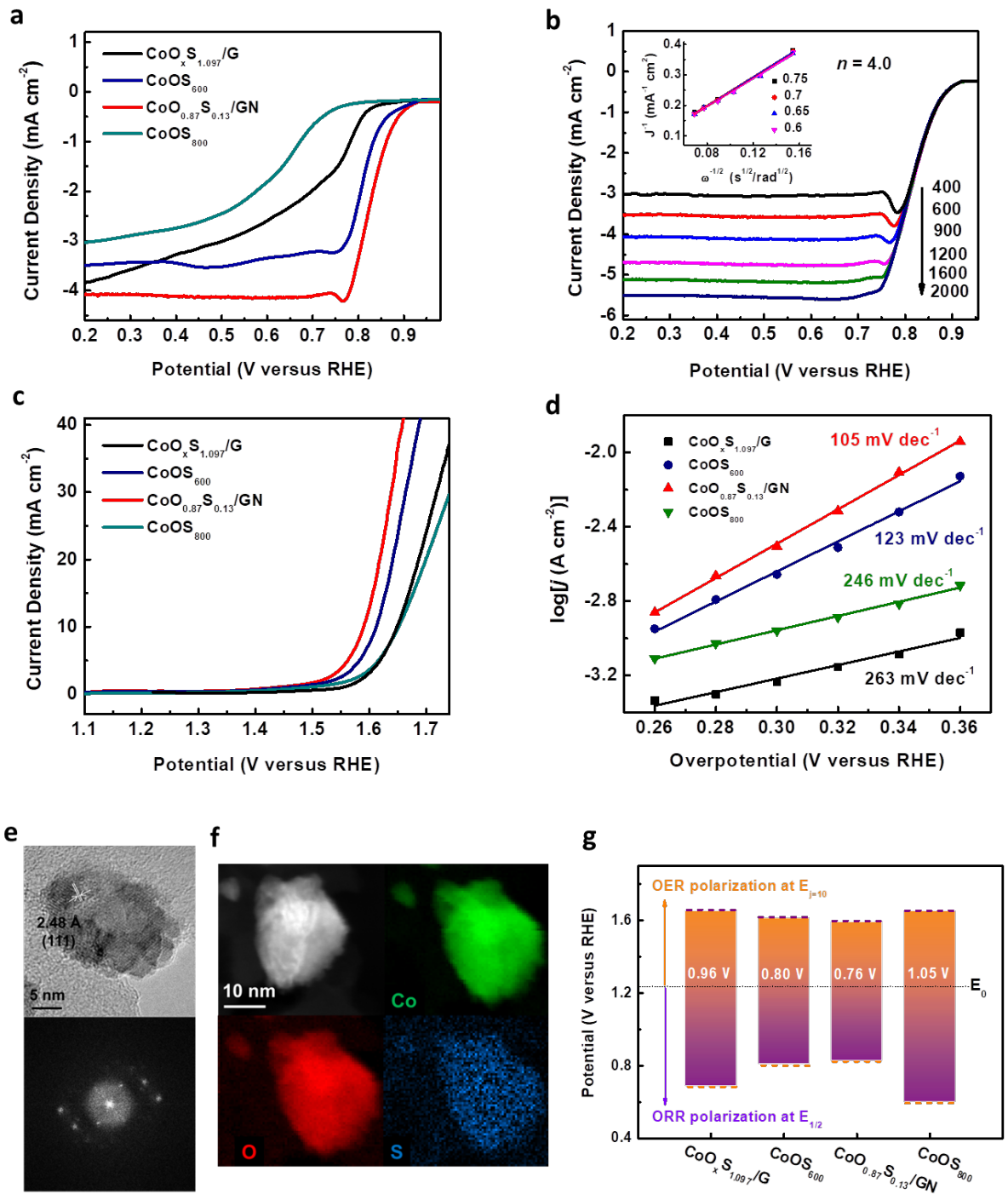

Figure 5-8. a) Linear scan voltammograms (LSV) of ORR for $CoO_xS_{1.097}$/G, $CoOS_{600}$, $CoO_{0.87}S_{0.13}$/GN, and $CoOS_{800}$ electrodes at 900 r.p.m. in O_2-saturated 0.1 M KOH solution

with a scan rate of 5 mV s^{-1}. b) ORR polarization curves for $CoO_{0.87}S_{0.13}$/GN at various rotating speeds (inset: Koutecky-Levich plot obtained at different potentials). c) LSV of OER for $CoO_xS_{1.097}$/G, $CoOS_{600}$, $CoO_{0.87}S_{0.13}$/GN, and $CoOS_{800}$ electrodes at 900 r.p.m. in N_2-saturated 0.1 M KOH solution with a scan rate of 5 mV s^{-1}. d) Tafel plots for OER polarization curves of $CoO_xS_{1.097}$/G, $CoOS_{600}$, $CoO_{0.87}S_{0.13}$/GN and $CoOS_{800}$. e) High-resolution TEM image and the corresponding FFT patterns and f) EELS elemental mapping of the $CoO_{0.87}S_{0.13}$/GN catalyst after anodic polarization at 10 mA cm^{-2} for 3600 s in N_2-saturated 0.1 M KOH solution. g) Potential differences between the $E_{1/2}$ of ORR and $E_{j=10}$ of OER for all electrodes.

As shown in **Figure 5-9a**, when compared to the best-known ORR benchmark catalyst of carbon-supported Pt (Pt/C), $CoO_{0.87}S_{0.13}$/GN performs very similarly regarding E_{onset}, $E_{1/2}$, and the diffusion-limiting current (red and black dash lines). More significantly, $CoO_{0.87}S_{0.13}$/GN shows better ORR stability than the Pt/C catalyst without significant losses in activity after 3000 cycles of cyclic voltammetry between 0.6 and 1.7 V in O_2-saturated 0.1 M KOH solution at 50 mV s^{-1}. Although the OER benchmark catalyst of carbon-supported Ir (Ir/C) shows a small $\eta_{j=10}$ of 330 mV, $CoO_{0.87}S_{0.13}$/GN surpasses the performance of Ir/C with a lower overpotential of 420 mV (versus 468 mV for Ir/C) at a higher current density of 40 mA cm^{-2} (**Figure 5-9b**, red and black dash lines), signaling an enhancement in the apparent reaction rates for OER. After 3000 cycles Ir/C exhibits a remarkable increase in $\eta_{j=10}$ (363 mV), whereas $CoO_{0.87}S_{0.13}$/GN largely retains its OER activity with little change in $\eta_{j=10}$ (357 mV). These results highlight the outstanding performance of $CoO_{0.87}S_{0.13}$/GN on both activity and stability as compared to the benchmark catalysts. I infer that the origin of the remarkable stability is related to the covalency-reinforced structure of the single crystalline $CoO_{0.87}S_{0.13}$ nanoparticles (*i.e.* Co-O hybridization) and their coupling with N-doped GN, which plays a crucial role in the structural stability of $CoO_{0.87}S_{0.13}$/GN towards ORR and OER. I infer that the salient durability

of the $CoO_{0.87}S_{0.13}$/GN catalyst can be related to the covalency-reinforced hybrid structure of the catalyst as well as the structural stability of $CoO_{0.87}S_{0.13}$ nanoparticles. Such hybrid structure, where the $CoO_{0.87}S_{0.13}$ nanoparticles are embedded into an N-doped porous graphene support through the strong covalent coupling (i.e. Co-N bonds) between them, could alleviate aggregation of the $CoO_{0.87}S_{0.13}$ nanoparticles and thus result in better structural stability and performance durability than Pt/C or Ir/C catalyst. Apart from the strong coupling effect between $CoO_{0.87}S_{0.13}$ and NG, the stable crystal and chemical structures of the $CoO_{0.87}S_{0.13}$ particles, especially upon highly oxidative OER conditions, would also contribute to the improved durability of the hybrid catalyst.

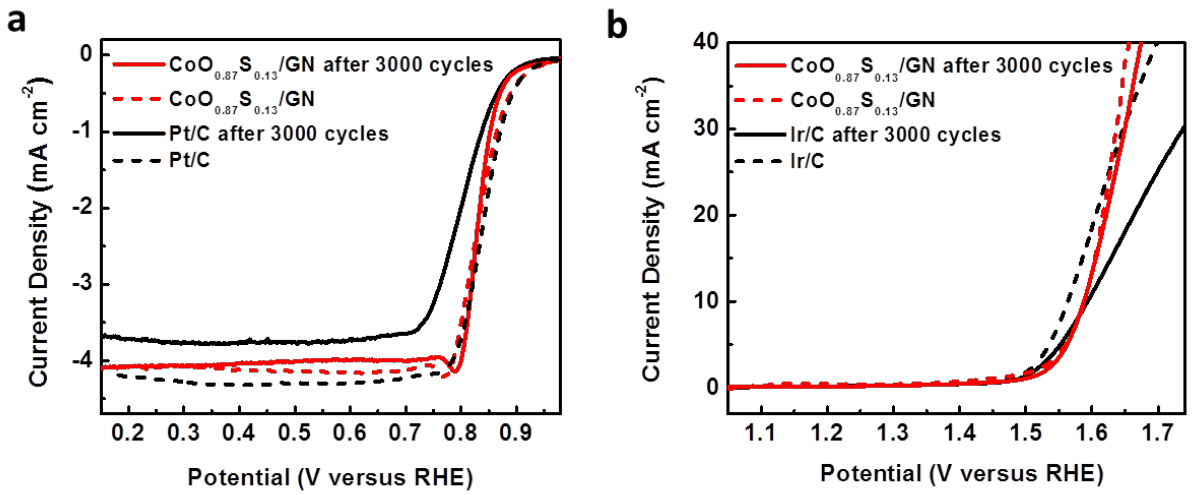

Figure 5-9. a) Comparative ORR activities of $CoO_{0.87}S_{0.13}$/GN and Pt/C before and after 3,000 cycles of cyclic voltammetry (CV) between 0.6 and 1.7 V in O_2-saturated 0.1 M KOH solution at 50 mV s^{-1}. b) Comparative OER activities of $CoO_{0.87}S_{0.13}$/GN and Ir/C before and after 3,000 cycles of CV between 0.6 and 1.7 V in O_2-saturated 0.1 M KOH solution at 50 mV s^{-1}.

Energy dense zinc-air batteries attract considerable attention to grid storage, electric vehicles and mobile electronics applications. Specifically, emerging flexible electronics would

benefit from the zinc-air battery solutions that are solid state while still being able to maintain high energy and power densities. Such use cases place strong requirements on the direct integration of bifunctional catalysts with the solid-state zinc-air battery, relevant to the interfacial and charge- and mass-transport properties of the catalyst assembly. A proof-of-concept of the rechargeable zinc-air battery with direct assembly of the $CoO_{0.87}S_{0.13}$/GN bifunctional catalyst with the QAFC membrane is depicted in **Figure 5-10a**. The solid-state zinc-air battery configuration consists of a zinc film, a $CoO_{0.87}S_{0.13}$/GN-coated cellulose membrane assembly (CMA) and a gas diffusion backing layer (GDL). To elucidate the practical benefit of $CoO_{0.87}S_{0.13}$/GN as the binder-free catalyst assembly, I prepared the CMA with an active catalyst surface area of 2.0 cm^2 via a simple filtration method (**Figure 5-10b**). The resulting CMA with a catalyst loading of 2.0 mg cm^{-2} was directly used for the zinc-air battery (the battery is referred to as ZAB). For comparison, a control battery was fabricated using an ink-based CMA, where the catalyst slurry composed of Nafion^{TM} binders and $CoO_{0.87}S_{0.13}$/GN was sprayed on the cellulose membrane (the battery is referred to as ZAB/Nafion). **Figure 5-10c** compares discharge and charge polarization curves of two batteries operated under ambient conditions, where ZAB and ZAB/Nafion exhibit a very similar open circuit voltage (1.43 V for ZAB versus 1.42 V for ZAB/Nafion). The negligible difference in the open circuit voltage reveals a similar catalytic activation loss between them. However, the polarization curve observed upon charging for ZAB/Nafion is wavy due to vigorous oxygen bubble coalescence at high current densities, whereas there is no substantial fluctuation seen for ZAB. Such stable charging performance arises from the quick removal of O_2 bubbles due to the O_2 transfer being more favorable in the binder-free CMA of ZAB. Moreover, with increasing

polarization, ZAB demonstrates an apparently lower overpotential during both discharge and charge processes than ZAB/Nafion with the voltage gap being more significant at higher current densities. The smaller voltage gap in ZAB underscores the advantage of the binder-free $CoO_{0.87}S_{0.13}$/GN assembly, which assures efficient charge transfer and diffusion of electrolyte and O_2 to the active sites. This is supported by electrochemical impedance spectroscopy (EIS) in **Figure 5-10d**, where ZAB exhibits both smaller ohmic (1.6 ohm) and charge transfer (1.4 ohm) resistances than ZAB/Nafion (1.8 and 3.5 ohm, respectively). Battery energy efficiency and power density plots for the two batteries are shown in **Figure 5-10e**. The energy efficiency can be determined by dividing the discharge potential by the charge potential at a certain current density.[203] The performances of ZAB using the binder-free CMA is substantially higher than that in ZAB/Nafion, owing to its uncomplicated access of the reactants to the catalytic sites (*i.e.* efficient utilization of the catalyst). For example, the energy efficiency and power density at a current density of 100 mA cm^{-2} for ZAB increase by a factor of 1.9 and 1.6, respectively, as compared with those of ZAB/Nafion. The specific capacity acquired from ZAB at 10 mA cm^{-2} is 709 mAh g_{Zn}^{-1} (**Figure 5-10f**), corresponding to a higher energy density of 857.9 Wh kg^{-1} than that of ZAB/Nafion (784.1 Wh kg^{-1}).

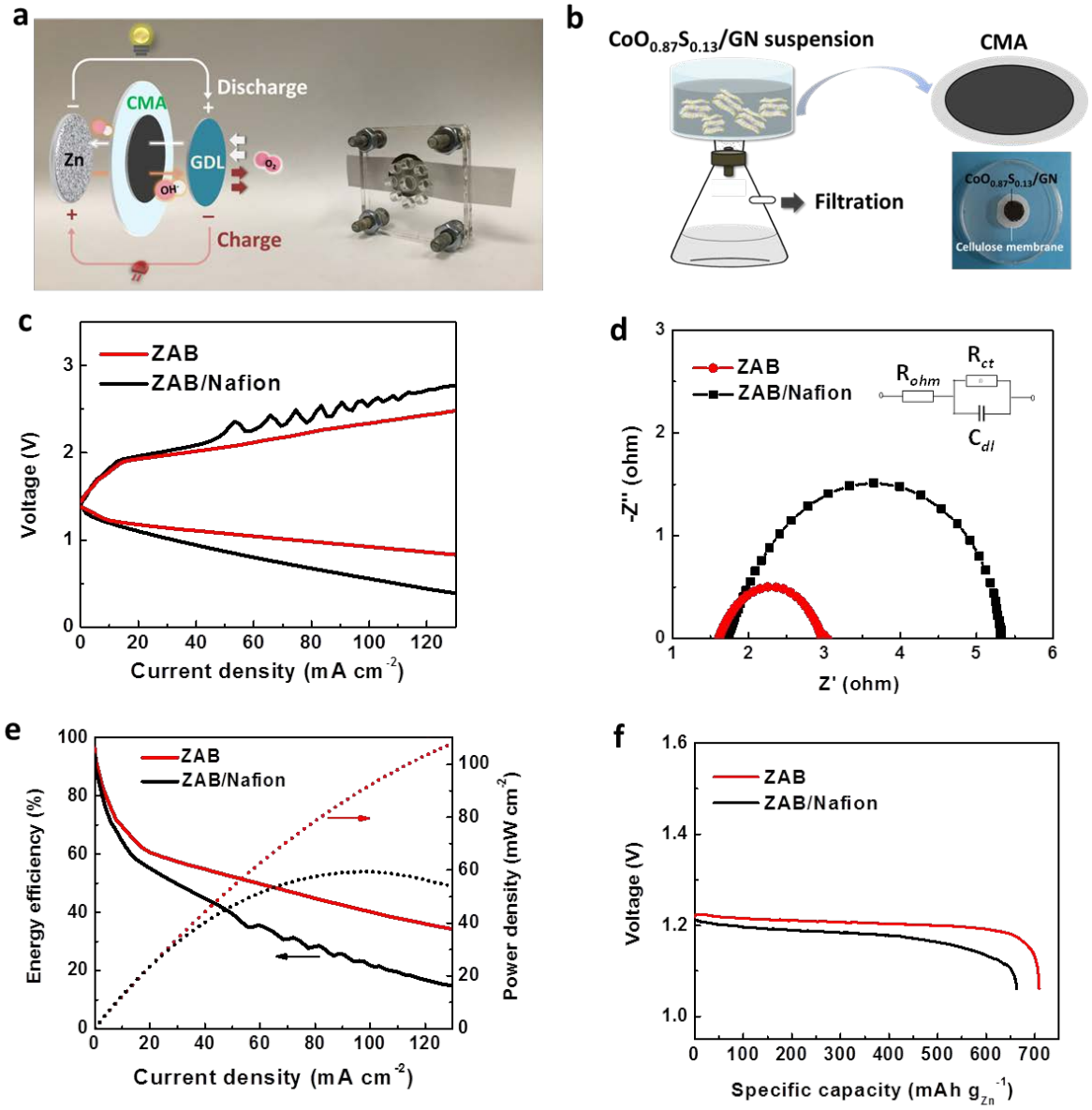

Figure 5-10. a) Schematic illustration of the solid-state zinc-air battery configuration. b) Fabrication procedure and a photograph of the binder-free $CoO_{0.87}S_{0.13}$/GN catalyst-coated cellulose membrane assembly (CMA) with an active surface area of 2.0 cm^2. c) Galvanodynamic discharge and charge polarization curves of ZAB and ZAB/Nafion. d) Nyquist plots and, e) energy efficiency and power density curves for ZAB and ZAB/Nafion. f) Typical specific capacity (normalized to the mass of zinc electrode) curves of the batteries using $CoO_{0.87}S_{0.13}$/GN and Nafion/ $CoO_{0.87}S_{0.13}$/GN at 10 mA cm^{-2}.

Furthermore, to examine battery stability, ZAB was cycled at a current density of 20 mA cm^{-2} with each cycle being 1 h. As shown in **Figure 5-11a**, the initial discharge-charge voltage gap is only 0.76 V, contributing to an energy efficiency of 60.4%. After 300 cycles (300 h of operation time), both the voltage gap and energy efficiency remain nearly unchanged (0.77 V and 60.0 %), indicating the superior stability of $CoO_{0.87}S_{0.13}$/GN in ZAB. As a comparison, the battery using the Pt/C+Ir/C mixture catalyst was examined under the same test conditions. Despite the similar initial performance (the initial voltage gap of 0.75 V), the energy efficiency of the battery using Pt/C+Ir/C decreases much faster than that of $CoO_{0.87}S_{0.13}$/GN after 50 cycles from 61.0 % to 40.2%, and the battery continues to degrade over the time (**Figure 5-11b**).

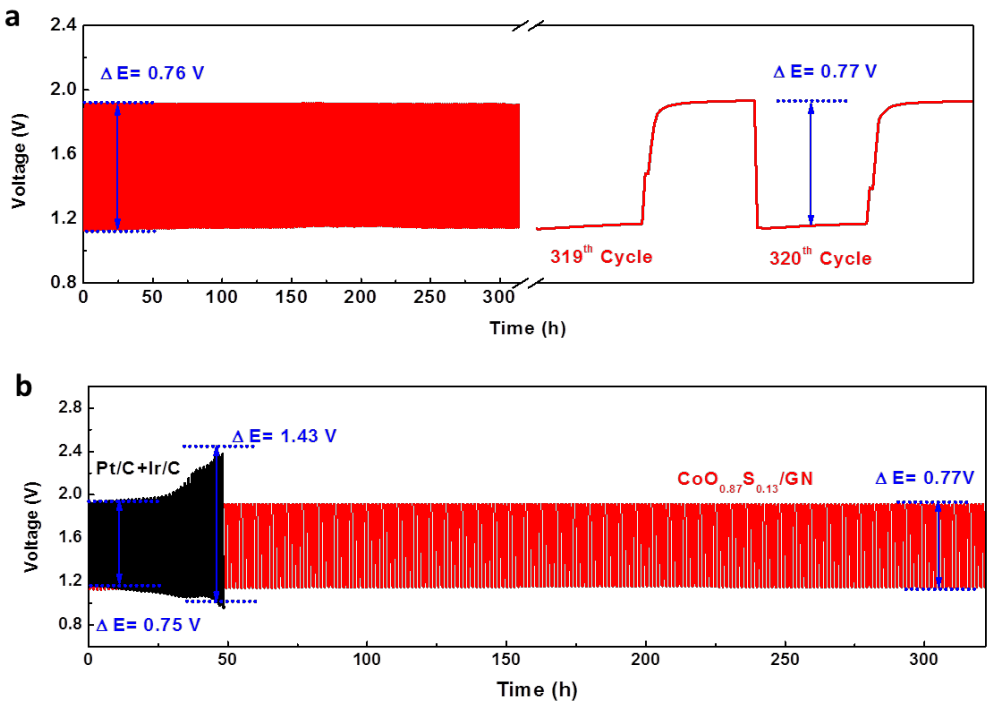

Figure 5-11. a) Galvanostatic discharge and charge cycling stability of ZAB using the binder-free $CoO_{0.87}S_{0.13}$/GN at a current density of 20 mA cm^{-2} with each cycle being 1 h. b) Long-

term galvanostatic cycling performances of the batteries using $CoO_{0.87}S_{0.13}$/GN and Pt/C+Ir/C catalysts, respectively, at 20 mA cm^{-2} with a cycle period of 1 h.

5.4 Conclusions

$CoO_{0.87}S_{0.13}$/GN serves as an efficient bifunctional catalyst to be used in PEMZAB. The synthesis of $CoO_{0.87}S_{0.13}$/GN with unique physicochemical properties and a defective nature was accomplished by the ammonolysis. The methodology realized simultaneous generation of the defect-rich (i.e. O vacancies and N-doped pores) and covalency-reinforced (i.e. Co-O hybridization and Co-N bonding) hybrid structure. The optimal balance between active defects and stable covalent-network-structure was found for $CoO_{0.87}S_{0.13}$/GN, which manifested significant catalytic activity and stability for ORR and OER. Moreover, a binderless catalyst film can be formed by filtering of the $CoO_{0.87}S_{0.13}$/GN catalyst suspension through the QAFC membrane. This catalyst film, combining with the QAFC electrolyte membrane, was then used in the rechargeable zinc-air battery to achieve a long cycling stability over 300 h at 20 mA cm^{-2}.

Chapter 6 Direct assembly of bifunctional oxygen catalysts with a conductive substrate in a three-dimensional porous architecture

6.1 Introduction

Chapter 5 describes a rational catalyst design that aims to increase the catalytic activity of the improved $CoO_{0.87}S_{0.13}$/GN bifunctional catalyst for both the ORR and OER. Despite the activity improvement, the air electrode assembly requires the catalysts be intimately bound to a porous, conductive current collector (e.g., carbon fiber paper). However, the conventional fabrication methods using polymer binders often lead to undesirable interfaces that are unfavorable for electron transfer between the catalysts and the conductive substrate.[184] Moreover, continuous oxygen gas evolution during the battery charging would detach the catalysts from the substrate, which greatly impairs their catalytic activity and lifetime.[204] To address these issues, one strategy would be to construct three-dimensional (3D) catalytically active sites that couple directly with a conductive support in a suitable architecture.

In this chapter, a hybrid catalyst/current collector assembly is designed for rechargeable zinc-air batteries. In this assembly, a hair-like array of mesoporous cobalt oxide nanopetals in nitrogen-doped carbon nanotubes is grown directly on a stainless-steel mesh. Such integrative design not only ensures a large number of catalytically active sites in a given electrode surface, but also increases the electron transfer between each individual catalyst and the conductive substrate. Moreover, the current collector for the air electrode is not necessary due to sufficient electrically conductivity of the stainless steel mesh. This completely eliminates the voltage drop that reduces battery performance due to the interfacial resistance between the current collector and air electrode.

Herein, inspired by the spinous structure of human hairs and their mechanism and patterns of growth, I introduced a 3D nanoarchitectured rechargeable air electrode assembly through morphological emulation of human hair array, and demonstrate its performance in a flexible solid-state zinc-air battery. This integrative electrode has an array of nanoassembled hair-like catalysts vertically and directly grown on a flexible stainless-steel (SS) mesh. Each individual hair-like catalyst of the array contains a nanoassembly of two-dimensional (2D) mesoporous Co_3O_4 nanopetals in a one-dimensional (1D) nitrogen-doped multi-walled carbon nanotube (NCNT). Architecting the bifunctional catalyzed air electrode through the morphological emulation of human hair array possesses several advantages over the conventional physically prepared air electrodes. First, the vertically-aligned NCNT directly wired to the metallic SS mesh can minimize the electrical contact resistance between the NCNT framework and the current collector (SS mesh), greatly improving the electron transfer properties of the whole electrode. This direct wiring thus completely eliminates the voltage drop that reduces battery performance due to the interface resistance between the current collector and air electrode. Second, every individual self-standing Co_3O_4-NCNT nanoassembly on the electrode serves as the active site, significantly enhancing active material utilization for high efficiency and power generation, especially at high local current densities. In addition, the hair-like 3D nanostructure of the Co_3O_4-NCNT nanoassembly provides intimate interfacial contact through covalent interactions between the Co_3O_4 nanopetals and the conductive NCNT, facilitating rapid charge transfer during catalytic oxygen reactions. Third, the highly porous nature of the 3D nanoarchitectured electrode allows efficient diffusion of reactants (oxygen and electrolyte) through the free space among the neighboring Co_3O_4-NCNT nanoassemblies. This

efficient diffusion within the electrode guarantees a low concentration polarization of the battery especially at high current drains.

6.2 Experimental section

6.2.1 Preparation of the air electrode assembly

The stainless steel (SS) mesh (Super fine #500 E-Cig 25 μm, The Mesh Company) was sonicated sequentially in 2 M hydrochloric acid, acetone and ethanol. Iron hydroxide was directly deposited on the pretreated SS mesh by cathodic electrodeposition in a standard three-electrode electrochemical cell, consisting of the SS mesh working electrode, a platinum foil counter electrode and a saturated calomel electrode (SCE) reference electrode. Cathodic electrodeposition was performed at a fixed potential of -1.1 V (versus SCE) in an electrolyte bath containing 0.03 M iron nitrate and 0.03 M potassium nitrate at 25 ^{o}C for 500 s. Upon calcination at 600 ^{o}C in air for 3 h, a layer of uniformly distributed iron oxide nanoparticles deposited on the SS mesh was derived and the sample was denoted as Fe-SS mesh. The direct growth of NCNT on the Fe-SS mesh (denoted as NCNT/SS) was conducted through chemical vapor deposition (CVD) under atmospheric pressure. The carrier gas used was argon at a flow rate of 140 mL min^{-1}, and the reaction was carried out at 750 °C for 1 h, using a vaporized 4 mL of ethylenediamine (⩾99.5%, Sigma Aldrich) as a carbon and nitrogen precursor. After the growth, the NCNT/SS was rinsed with ethanol and left dry in air. Electrodeposition of $Co(OH)_2$ on the NCNT/SS was performed at a constant potential of -1.0 V (versus SCE) in a solution containing 0.03 M cobalt nitrate and 0.01 M ammonium nitrate at 25 ^{o}C. The optimized deposition time was determined to be 150 s. After being washed with ethanol and dried in air,

the as-deposited sample was annealed at 300 ^{o}C with a ramping rate of 1 ^{o}C min^{-1} for 2 h in air, and the as-annealed sample was denoted as Co_3O_4-NCNT/SS. For comparison, pure Co_3O_4 was also electrodeposited on the SS mesh (denoted as Co_3O_4/SS) through the same electrodeposition procedure as the Co_3O_4-NCNT/SS. The air electrodes using commercial state-of-the-art 20 wt% Pt/C and 20 wt% Ir/C catalysts were prepared by dip coating method. The SS mesh was dipped into a catalyst ink for 1 min, then taken out and dried in air. A catalyst loading of ~1.1mg cm^{-2} was obtained for the Pt-C/SS and Ir-C/SS electrodes by repeating the above dip-coating procedure. The catalyst ink was prepared by dispersing 4.0 mg of the catalyst and 42 µl of 5 wt% basic ionomer (AS-4, Tokuyama Inc.) in 1.0 mL of 1-propanol (anhydrous, 99.7%, Sigma Aldrich).

6.2.2 Fabrication of the PEMZAB

A zinc-air battery was fabricated by a layer-by-layer method, using a zinc electrode, a porous cellulose film, a Co_3O_4-NCNT/SS air electrode and a carbon cloth. The carbon cloth was attached to the Co_3O_4-NCNT/SS air electrode for the purpose of oxygen distribution. The cellulose film was pre-doped by 6 M KOH solution before battery assembly. The actual area of the Co_3O_4-NCNT/SS electrode exposed to the electrolyte was 2.0 cm^2.

6.2.3 Characterization and electrochemical measurements

Scanning electron microscopy (LEO FESEM 1530) and transmission electron microscopy (JEOL 2010F TEM/STEM field emission microscope) were utilized to confirm the electrode's morphology and structure. X-ray Diffraction (INEL XRG 3000, Cu Kα radiation (λ=1.54178 Å)), X-ray photoelectron spectroscopy (Thermal Scientific K-Alpha X-ray source)

and Raman spectroscopy (Bruker Senterra) were conducted to characterize crystal structure, elemental composition and the surface chemistry of the electrode materials. Thermogravimetric analysis (TA Q500, in air atmosphere with a ramp rate of 10 ^{o}C min^{-1}) and Brunauer–Emmett–Teller surface area and porosity analysis (Micromeritics ASAP 2020) were used to determine the weight loss and pore size distribution of electrodes.

The half-cell electrochemical measurements were conducted in a three-electrode electrochemical system using a calibrated reversible hydrogen electrode (RHE) as the reference electrode, a graphite rode as the counter electrode and the as-prepared SS mesh-based electrode as the working electrode. To investigate oxygen reduction and evolution reactions, steady-state linear sweep voltammetry was performed using a potentiostate (CHI 760D) in oxygen- and nitrogen-saturated 0.1 M KOH solution, respectively, at a scan rate of 5.0 mV s^{-1}. The measured currents from voltammetry were normalized by the geometric area of the electrodes (1.0 cm^{-2}). Tafel slopes were derived from the iR-compensated ORR and OER polarization curves. Chronopotentiometry was performed at a constant anodic and cathodic current density of 10 mA cm^{-2} under the same experimental setup. For comparison, the Pt-C/SS and Ir-C/SS electrodes were measured with the same conditions. The zinc-air battery electrochemical evaluation was performed under the oxygen condition. Electrochemical impedance spectroscopy was conducted by operating the battery at a fixed potential of 0.7 V with an alternating current amplitude of 20 mV ranging from 100 kHz to 0.1 Hz. Galvanodynamic discharge and charge polarization data was collected from 0 to 270 mA cm^{-2} at a current step of 1.0 mA s^{-1}. Galvanostatic cycling tests were performed at a fixed current and time interval for each state of discharge and charge.

6.3 Results and Discussion

A schematic of the hair-like array of Co_3O_4-NCNT/SS air electrode is illustrated in **Figure 6-1a**. The synthesis of Co_3O_4-NCNT/SS is based on the following three steps (**Figure 6-1b**). First, iron oxide seeds as NCNT growth catalysts were deposited locally on the SS mesh surface by electrodeposition and subsequent calcination. Second, each individual NCNT was directly and vertically wired to the conducting surface of the SS mesh (referred to as NCNT/SS) , through iron-catalyzed chemical vapor deposition (CVD).

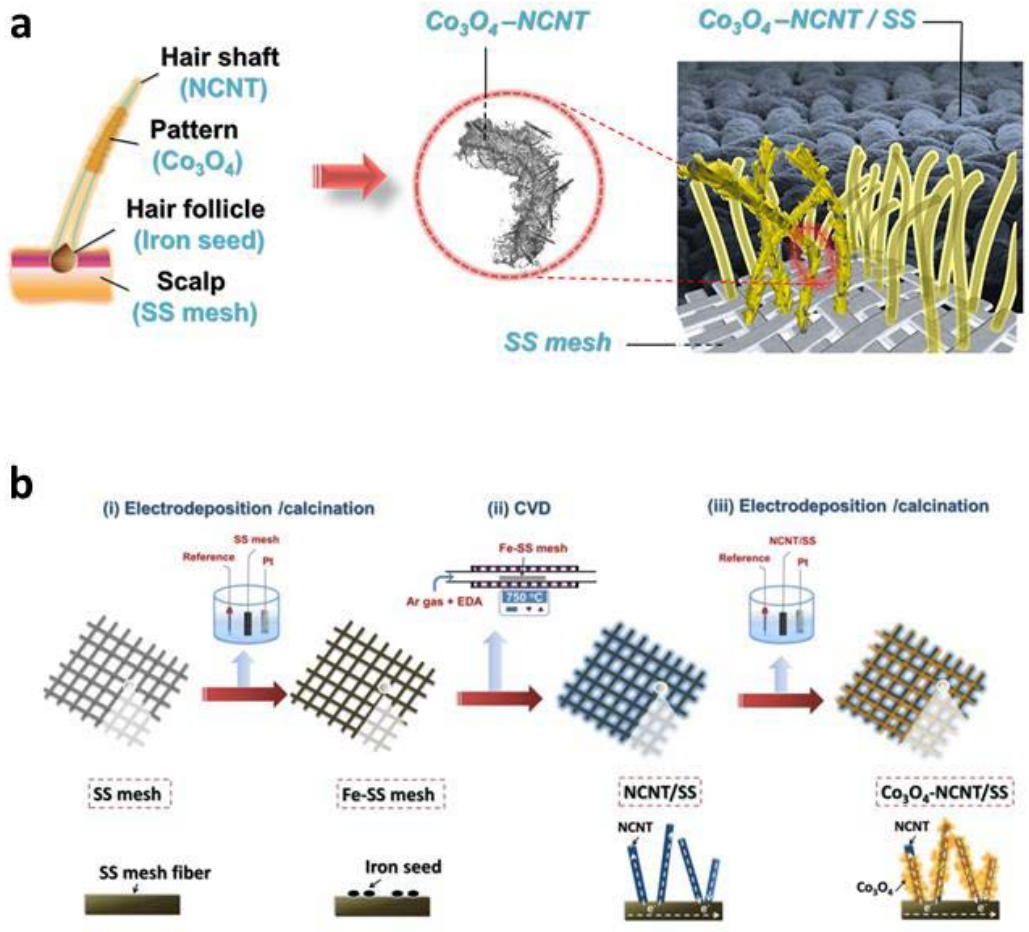

Figure 6-1. a) A schematic illustration of hair-like array of Co_3O_4-NCNT/SS air electrode. b) An illustration of the synthesis process of the Co_3O_4-NCNT/SS air electrode. Iron oxide

nanoparticles grown on the SS mesh (Fe-SS mesh, step i). Growth of NCNT on the Fe-SS mesh by CVD (NCNT/SS, step ii). Electrodeposition of $Co(OH)_2$ on the NCNT/SS and subsequent calcination (Co_3O_4-NCNT/SS, step iii).

Figure 6-2 further reveals the base-growth of NCNT with the iron seeds (Fe_3O_4) residing on the SS mesh substrate, similar to the process by which a hair follicle anchors each hair in skin. This approach enables direct coupling of the NCNT framework to the SS mesh without sacrificing electrical conductivity, and while retaining the beneficial characteristics of NCNT. Finally, Co_3O_4 nanopetals were uniformly distributed on the external surface of the NCNT framework via electrodeposition and subsequent annealing, forming the array of Co_3O_4-NCNT nanoassemblies. This vertically-aligned array on the SS mesh (referred as Co_3O_4-NCNT/SS) shares a remarkable similarity to human hair, while the porous SS mesh substrate serves as the breathable scalp skin.

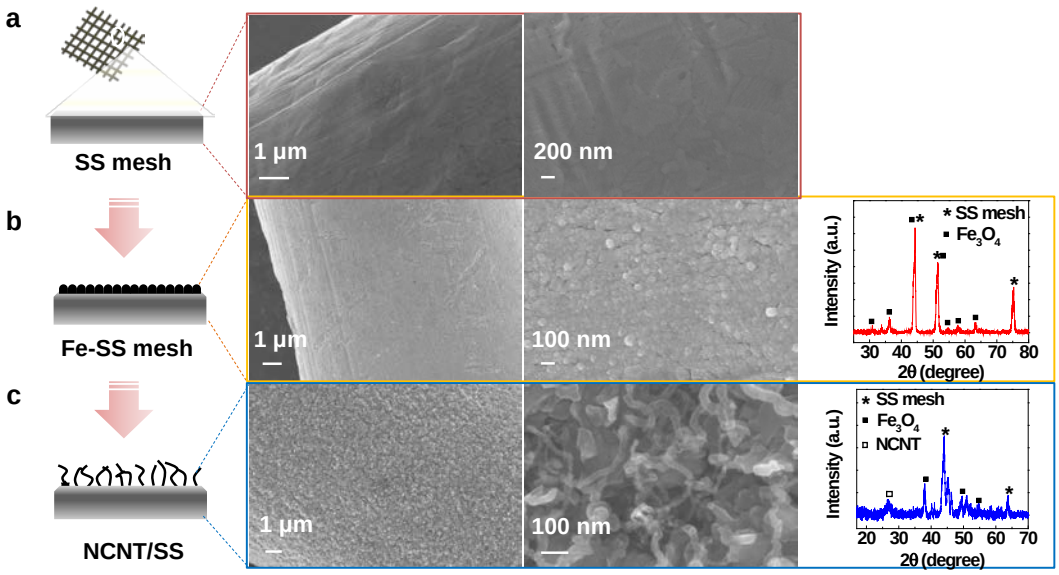

Figure 6-2. Growth mechanism of the NCNT on a stainless steel mesh. Schematics and the corresponding SEM images and XRD analysis of (a) bare SS mesh, (b) Fe-SS mesh and (c) NCNT/SS after the CVD growth for 10 min.

As shown in **Figure 6-3a**, the bare SS mesh skeleton is densely covered with NCNT after the growth by CVD. An enlarged SEM image (**Figure 6-3b**) shows that the NCNT are loosely packed, with free internal spaces. Such internal spaces allow electrolyte-accessible surface areas, facilitating the electrodeposition of Co_3O_4 onto individual NCNT surfaces with a good homogeneity and distribution. The observed bamboo-like structure of NCNT with closely spaced nodes along the nanotube length (**Figure 6-3c**) can be ascribed to high level nitrogen doping of the graphitic structure.[205] In addition to the NCNT, the assembly of Co_3O_4 in the NCNT/SS electrode is detected in **Figure 6-3d**, where the interspace of the SS skeleton is visibly smaller than that of NCNT/SS. **Figure 6-3e, f** further show that the Co_3O_4 was well-distributed on each individual NCNT surface, forming a unique hierarchical nanostructure similar to the human hair with petal-like (spinous) scale patterns (**Figure 6-3f**, inset). This hair-like structure of the Co_3O_4-NCNT nanoassembly can provide intimate interfacial contact between Co_3O_4 and NCNT, favouring a low-resistance pathway for a high flux of charge transfer during ORR and OER.[206] The Co_3O_4-NCNT/SS electrode as prepared (2×8 cm^2) is shown in **Figure 6-3g**, and exhibits superior flexibility even at a torsion angle of 360^o (**Figure 6-3h**).

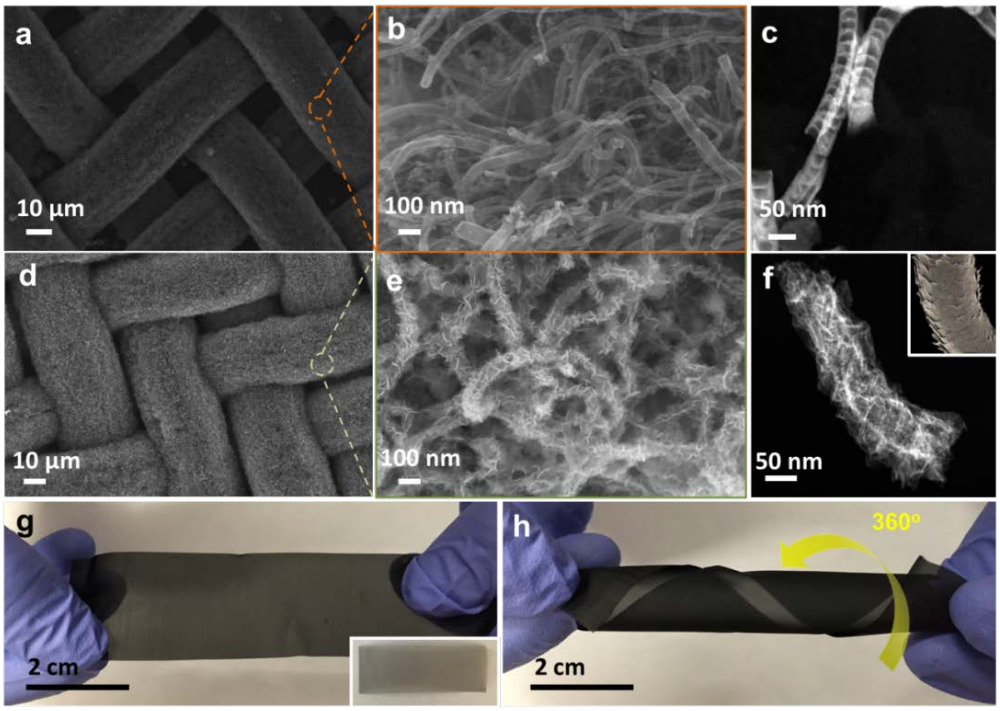

Figure 6-3. a,b,d,e) SEM images of the (a,b) NCNT/SS and (d,e) Co_3O_4-NCNT/SS air electrodes. c,f) TEM images of the (c) individual NCNT and (f) Co_3O_4-NCNT. The inset in (f) showing the petal-like (spinous) scale patterns of human hair. g,h) Digital photos of the Co_3O_4-NCNT/SS electrode (g) without and (h) with twisting the electrode to 360°. The inset in (g) shows a bare SS mesh.

The spatial distribution of nitrogen atoms in NCNT is further identified by electron energy loss spectroscopy (EELS). As shown in **Figure 6-4a**, nitrogen atoms are well overlaid with carbon atoms along the nanotube, indicative of homogenous nitrogen doping in the bamboo-like NCNT. A high atomic nitrogen concentration of 7.96% in NCNT/SS was measured by X-ray photoelectron spectroscopy (XPS) (**Figure 6-4b**). Furthermore, a high resolution transmission electron microscopy (HRTEM) image reveals that the interlayer spacing of the outermost walls (~0.37 nm, blue and yellow lines in **Figure 6-4c**) is slightly larger than that of the inner graphitic walls (~0.34 nm, red and orange lines in **Figure 6-4c**).

The smaller interlayer spacing suggests fewer nitrogen doping-induced defects in the graphitic structure of the inner walls, which could retain the electrical property of the NCNT.[207] **Figure 6-4d** displays a high resolution N1s XPS spectrum of the NCNT/SS. The N 1s spectrum indicates the existence of four nitrogen species, which are fitted into peaks at 398.7 eV (pyridinic N, 50.4 at%), 400.6 eV (pyrrolic N, 22.3 at%), 401.8 eV (graphitic N, 21.6 at%) and 405.3 eV (chemisorbed nitrogen oxide, 5.7 at%).[208]

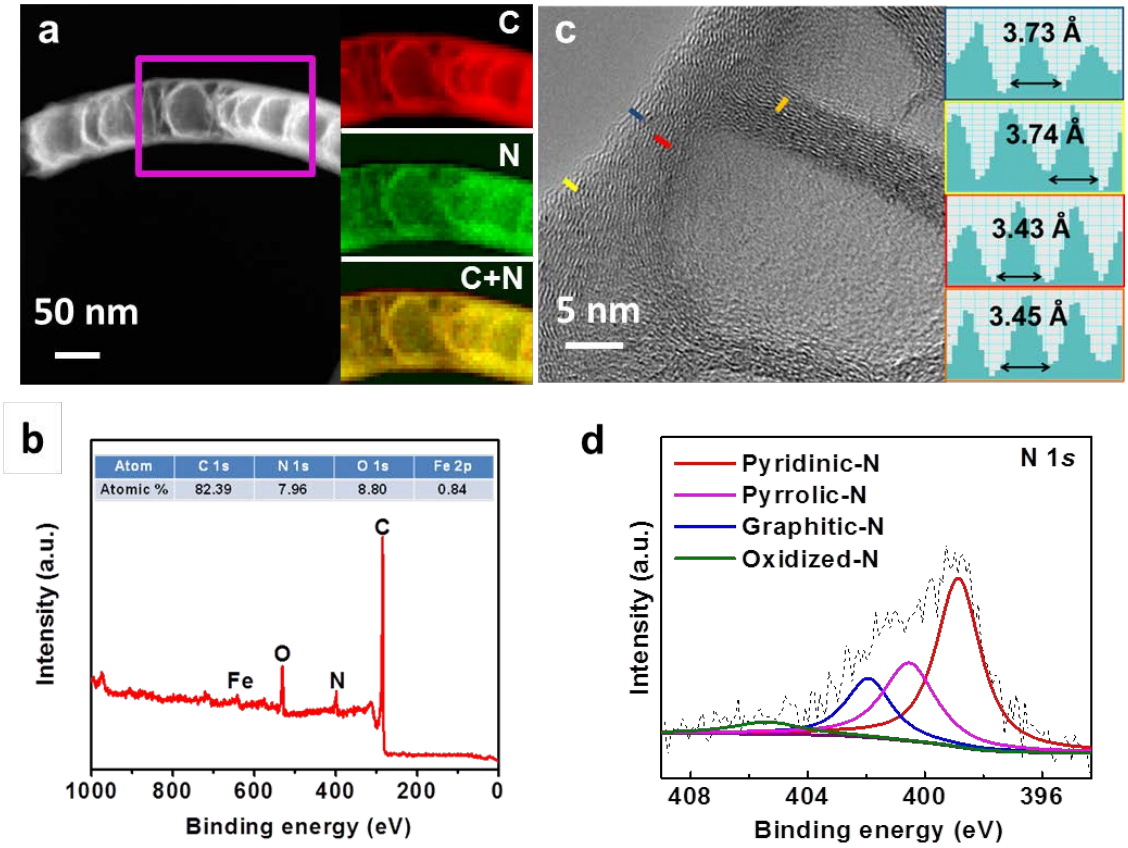

Figure 6-4. a) High-angle annular dark field (HAADF)-STEM image of the NCNT and corresponding electron energy loss spectroscopy (EELS) mappings of carbon, nitrogen, and overlaid carbon and nitrogen atoms. b) XPS survey spectra of the NCNT/SS electrode with atomic composition for the elements C, N, O and Fe. c) High resolution TEM (HRTEM) image of bamboo-like NCNT and corresponding line profiles along the line marked in blue, yellow,

red and orange, showing the interlayer spacing between wall layers. d) High resolution N 1s spectrum of the NCNT/SS.

The bright contrast in the high-angle annular dark field (HAADF) STEM image of the Co_3O_4-NCNT nanoassembly and corresponding energy-dispersive X-ray spectrometry (EDX) mappings (**Figure 6-5a**) show clearly the occupancies of cobalt and oxygen atoms distributed uniformly along NCNT. XPS survey confirms the presence of Co_3O_4, accompanied by two spin-orbit doublets at 795.87 eV and 780.85 eV for Co $2p_{3/2}$ and Co $2p_{1/2}$, respectively (**Figure 6-5b**). The TEM image in **Figure 6-5c** further reveals that each individual Co_3O_4 nanopetal is well attached in a perpendicular-like orientation to the NCNT surface, similar to the spinous structure of human hair. More importantly, these nanopetals also feature a mesoporous structure with a pore diameter of ~4.5 nm (**Figure 6-5c**, inset). The mesoporosity of Co_3O_4 nanopetals observed by TEM is confirmed by Brunauer-Emmett-Teller (BET) analysis (**Figure 6-5d**), with the pore size distribution centered at ~4.3 nm. This mesoporous structure will further enhance the electrolyte-accessible surface area and facilitate easier ion diffusion throughout the 3D nanoassembly of the electrode.[209] The porosity of Co_3O_4 nanopetals may result from dehydration of the electrodeposited cobalt hydroxide during the mild thermal annealing process, suggestive of a phase transformation into Co_3O_4. The lattice fringes and corresponding selected-area electron diffraction (SAED) pattern in **Figure 6-5e** confirm the spinel Co_3O_4 crystal structure of the nanopetals.

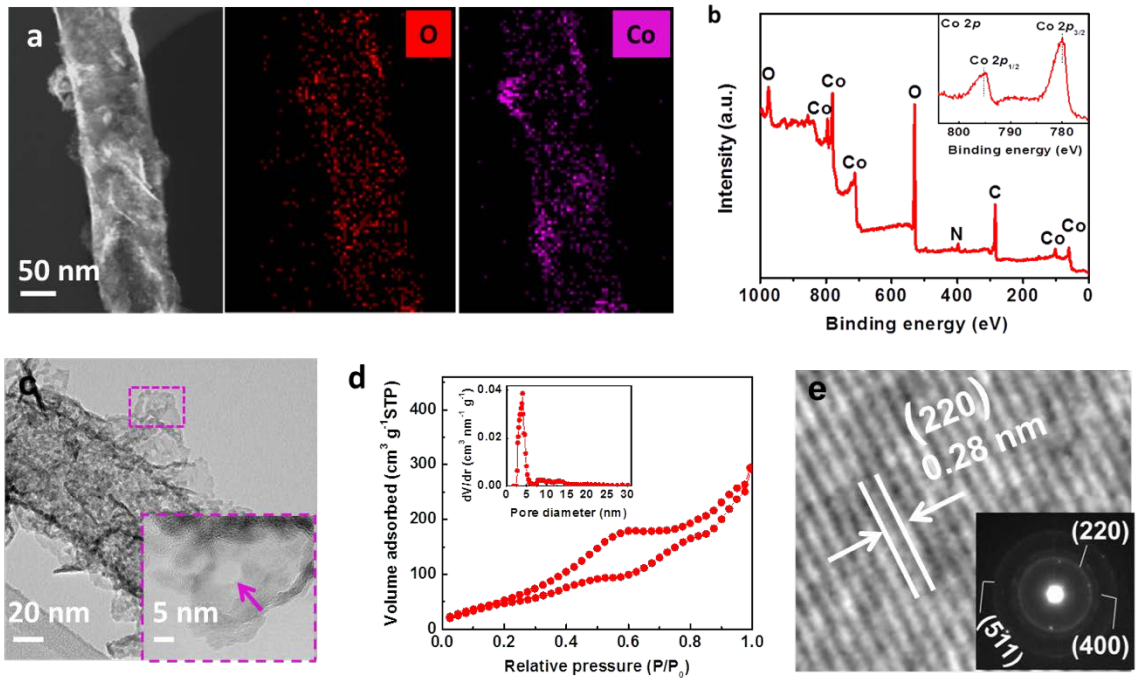

Figure 6-5. a) HAADF-STEM image of the Co_3O_4-NCNT and corresponding EDX mappings of oxygen and cobalt atoms. b) XPS survey spectra of the Co_3O_4-NCNT/SS electrode. c) TEM image of the Co_3O_4-NCNT nanoassembly with the inset showing the mesoporous structure of Co_3O_4 nanopetals. d) Nitrogen adsorption-desorption isotherm and pore size distribution of the Co_3O_4 nanopetals. e) HRTEM image of the Co_3O_4 nanopetal with inset showing the selected area electron diffraction (SAED) pattern of the major ring matching to the atomic plane with the spacing of 0.28 nm.

Figure 6-6a shows a typical Raman spectrum of the Co_3O_4-NCNT/SS, exhibiting signature peaks of both NCNT and Co_3O_4. There are two strong peaks at 1351 and 1580 cm^{-1}, corresponding to the D and G bands of NCNT, respectively. Moreover, five distinguishable peaks are identified at 686, 479, 619, 523 and 199 cm^{-1} (**Figure 6-6a**, inset). They correspond to A_{1g}, E_g and three F_{2g} symmetric phonon modes of spinel-structured Co_3O_4, respectively.[210, 211] The dominant A_{1g} peak is attributed to the Co-O breathing vibration of Co^{2+} ions in tetrahedral coordination, which is a typical characteristic of the spinel Co_3O_4 structure.[212]

Confocal Raman imaging was used to illustrate the homogeneity of the Co_3O_4-NCNT nanoassemblies grown on the SS mesh. This spectral analysis allows for a direct visualization of the spatial variation of the electrode nanoarchitecture by integrating the intensity of characteristic spectral bands.[213] **Figure 6-6b** shows schematically a xyz-coordination system of the Raman mapping of the Co_3O_4-NCNT/SS electrode. A spot-to-spot confocal Raman mapping of the electrode assembly was acquired from 64 points covering an area of 100×100 μm^2 and measured as six layers in a stack for every 1.0 μm in the z-direction up to down. The overall thickness of the bare SS mesh and Co_3O_4-NCNT/SS electrode was measured to be ~56 μm and ~70 μm (with Co_3O_4-NCNT grown on both sides of the SS mesh), respectively. In this regard, a depth profiling with 1.0 μm resolution should effectively represent the spatial distribution of the Co_3O_4-NCNT nanoassemblies while going down the electrode. **Figure 6-6c** displays integration maps over the D, G and A_{1g} bands as a function of depth in the 100×100 μm^2 area outlined in **Figure 6-6b**. The color intensity shows the variation in vertical profile for every imaged layer with the bright regions being the highest peak intensity and the dark blue regions being pores. For the first layer (0 μm), there are the Co_3O_4-NCNT regions identified by the strong intensities of D, G and A_{1g} bands, corresponding to NCNT and Co_3O_4, respectively. Additionally, the location consistency of the three characteristic profiles reveals a highly uniform distribution of the Co_3O_4-NCNT nanoassemblies in this layer. Similarly, for integration maps of the third layer (-2 μm) and the fifth layer (-4 μm), the spatial distribution of D, G and A_{1g} band signals do not vary significantly, where these three characteristic profiles correspond well to the SS mesh pattern. The results reveal a considerable homogeneity of the Co_3O_4-NCNT nanoassemblies among layers of the electrode. This homogeneity is particularly

evident in the seventh layer (-6 μm), which approaches the surface of the SS mesh. Compared to the less deep layers, the average intensities of both the G and D bands show noticeable decreases in the seventh layer, while the A_{1g} band retains high signal intensity. This observation indicates that each individual NCNT had its full length completely covered with Co_3O_4 nanopetals, resulting from the excellent electrical and chemical properties of NCNT.

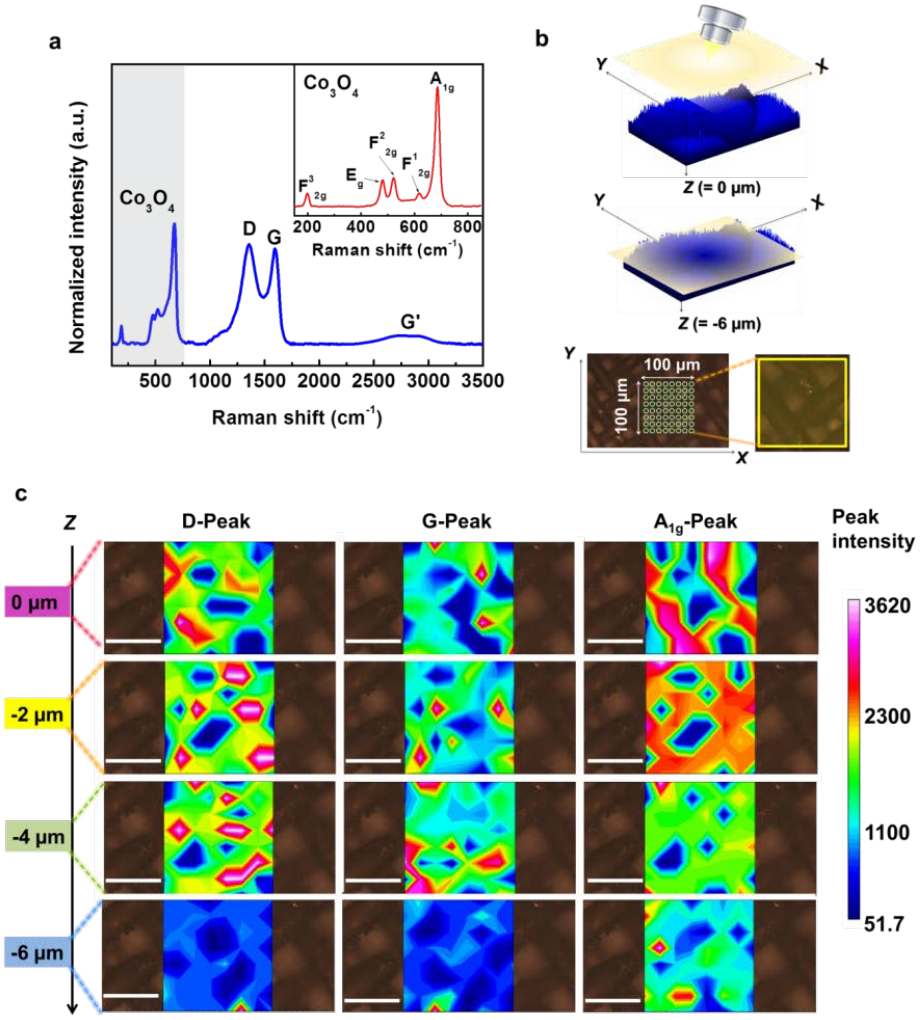

Figure 6-6. a) Raman spectrum of the Co_3O_4-NCNT/SS electrode. b) Schematic of the confocal Raman set-up, with the electrode imaging-stack covering 100×100×6 μm^3. c) Depth scanned

confocal Raman imaging stacks of the Co_3O_4-NCNT/SS electrode by integrating D peak, G peak and A_{1g} peak, respectively. Scale bar, 50 μm (c).

To assess the bifunctional catalytic activity, I performed electrochemical measurements using a standard three-electrode system, in which the Co_3O_4-NCNT/SS electrode served directly as the working electrode. The ORR and OER catalytic activities were evaluated by steady-state linear sweep voltammetry in a 0.1 M KOH solution. We found that a loading of ~1.1 mg cm^{-2} in the Co_3O_4-NCNT/SS electrode yielded the optimal ORR and OER activities. For comparison, Co_3O_4 was electrodeposited on the SS mesh (denoted as Co_3O_4/SS) by the same procedure of Co_3O_4-NCNT/SS. Commercial state-of-the-art 20 wt% Pt/C and 20 wt% Ir/C catalysts also were dip-coated onto the SS mesh surface, with loading of ~1.1 mg cm^{-2} (denoted as Pt-C/SS and Ir-C/SS), and were measured as ORR and OER benchmarks, respectively. Three indicators were examined to evaluate the bifunctional catalytic activities: (1) the onset potential (determined as the potential at 0.1 mA cm^{-2}),[214] (2) the specific activity (defined as the overpotential η at a current density of 10 mA cm^{-2}), and (3) the Tafel slope. The steady-state iR-compensated polarization curves of all the tested electrodes are shown in **Figure 6-7a**. The bare SS mesh shows very poor ORR activity with a negligible cathodic current density at a large overpotential (black line in **Figure 6-7a**). In contrast, Co_3O_4/SS, NCNT/SS and Co_3O_4-NCNT/SS all exhibit substantial improvement in ORR activity, with their more positive shifts of the onset potential and larger diffusion-limited current densities. In particular, NCNT/SS affords an onset potential of ~0.90 V versus the reversible hydrogen electrode (RHE) (green line in **Figure 6-7a**) and an overpotential of ~0.48 V at 10 mA cm^{-2} (blue bar in **Figure 6-7b**), strongly comparable to the ORR performance of Pt-C/SS, with an

onset potential of ~0.93 V (blue line in **Figure 6-7a**) and an overpotential of ~0.47 V at 10 mA cm^{-2} (blue bar in **Figure 6-7b**). The nanoassembling of Co_3O_4 nanopetals on the NCNT surfaces further enhances the ORR activity of the Co_3O_4-NCNT/SS, as reflected by the most positive onset potential (~0.95 V) (magenta line in **Figure 6-7a**) and the smallest overpotential (~0.44 V) at 10 mA cm^{-2} (blue bar in **Figure 6-7b**), outperforming those of the Pt-C/SS benchmark. Additionally, the ORR Tafel slope of Co_3O_4-NCNT/SS (51 mV dec^{-1}) is as low as that of Pt-C/SS (52 mV dec^{-1}) (**Figure 6-7c**), revealing its superior ORR activity. On the other hand, in the anodic region the Co_3O_4-NCNT/SS displays lower OER onset potential (~1.49 V) than that of SS mesh (~ 1.54 V), Co_3O_4 /SS (~ 1.53V, red line in **Figure 6-7a**), NCNT/SS (~ 1.52 V) and Ir-C/SS benchmark (~ 1.51 V, dark yellow line in **Figure 6-7a**). By conducting OER polarization at 10 mA cm^{-2} (red bar in **Figure 6-7b**), the specific activities were found in an order of Co_3O_4-NCNT/SS (η: 0.30 V)> Ir-C/SS (η: 0.32 V)> NCNT/SS (η: 0.34 V)> Co_3O_4/SS (η: 0.35 V)> SS (η: 0.43 V). Furthermore, the high OER activity of Co_3O_4-NCNT/SS is reflected by its low OER Tafel slope of 53 mV dec^{-1} (**Figure 6-7d**), strongly comparable to that of the Ir-C/SS benchmark (52 mV dec^{-1}).

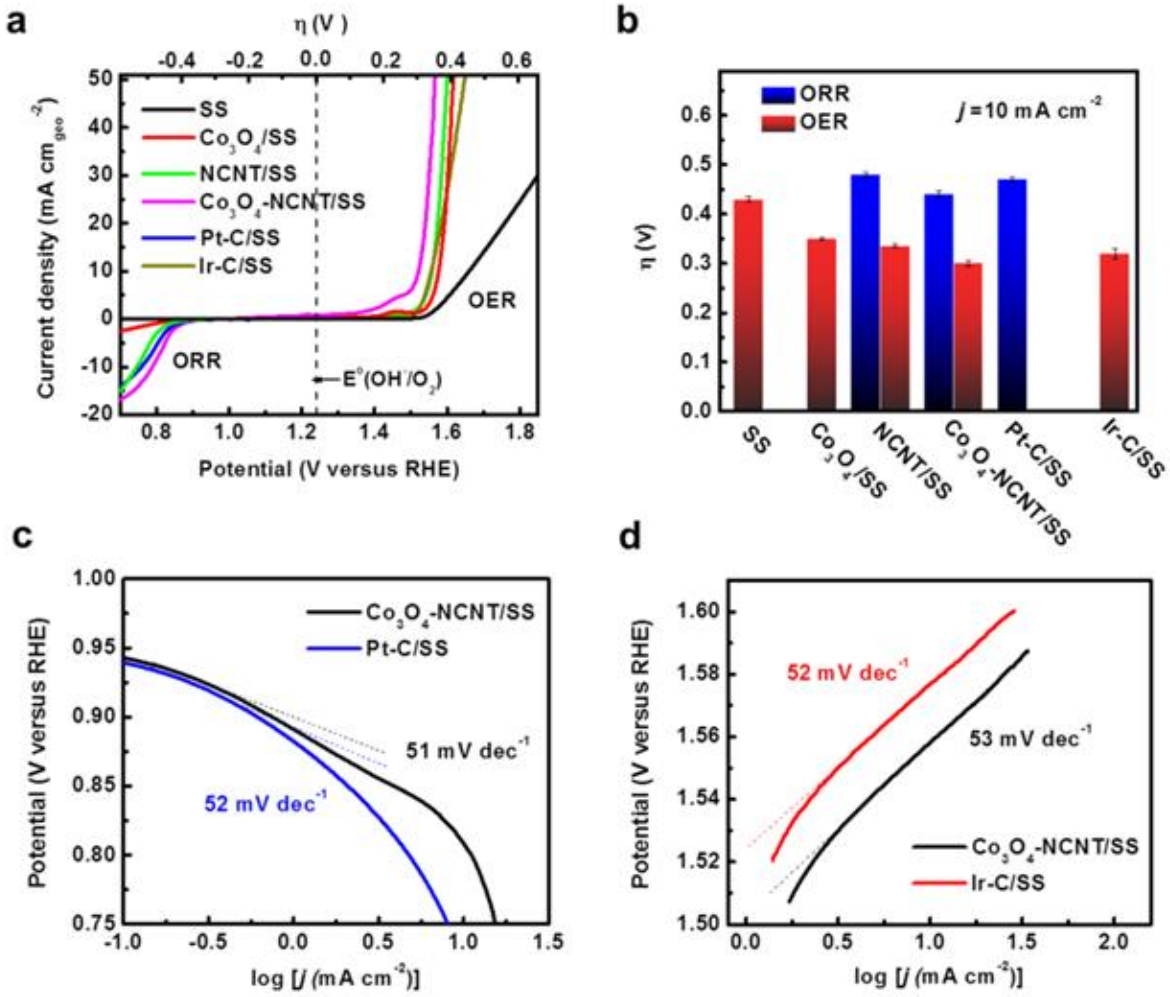

Figure 6-7. a) ORR and OER polarization curves and b) specific activities (at 10 mA cm^{-2}) of different air electrodes in 0.1 M KOH. c) ORR and d) OER Tafel plots of the Co_3O_4-NCNT/SS electrode compared with the Pt-C/SS and Ir-C/SS benchmarks, respectively.

In addition to the high bifunctional catalytic activity, the stability of Co_3O_4-NCNT/SS plays a crucial role in achieving a long lifecycle for rechargeable zinc-air batteries. The stability of Co_3O_4-NCNT/SS was examined at a constant cathodic and anodic current density of 10 mA cm^{-2} in 0.1 M KOH, respectively (**Figure 6-8a**). The Co_3O_4-NCNT/SS exhibits only small increases in the overpotential of ORR (~15 mV) and OER (~30 mV) over 7 h, whereas the

ORR overpotential of Pt-C/SS and the OER overpotential of Ir-C/SS gradually increased by ~ 60 mV and ~ 51 mV, respectively. The slower ORR and OER activity decays of Co_3O_4-NCNT/SS reveal its higher electrocatalytic stability than that of the Pt-C/SS and Ir-C/SS benchmarks in alkaline environment. The outstanding ORR and OER activity as well as stability of the Co_3O_4-NCNT/SS is likely related to its robust and flexible hair-like nanoarchitecture and synergistic effects between Co_3O_4 and NCNT. The vertically-aligned array of Co_3O_4-NCNT plays an important role in not only boosting electrocatalytic active sites, but also preventing each individual Co_3O_4-NCNT nanoassembly from restacking and detaching from the SS mesh substrate, particularly during the OER process. To verify this assumption, the surface morphologies of the Co_3O_4-NCNT/SS, Pt-C/SS and Ir-C/SS electrodes after the aforementioned OER stability test were characterized. An interconnected macroporous structure was observed to form along the SS fiber surface of the Co_3O_4-NCNT/SS electrode as a result of vigorous oxygen dissipation (**Figure 6-8b**), while both the Pt-C/SS and Ir-C/SS electrodes suffered from aggregation and detachment of nanoparticles (**Figure 6-8c-f**). This observation suggests that the hair-like array of the Co_3O_4-NCNT/SS is robust enough to provide adequate paths for easy release of the oxygen bubbles generated during OER, and to alleviate the detachment of Co_3O_4-NCNT nanoassembiles from the SS mesh surface.

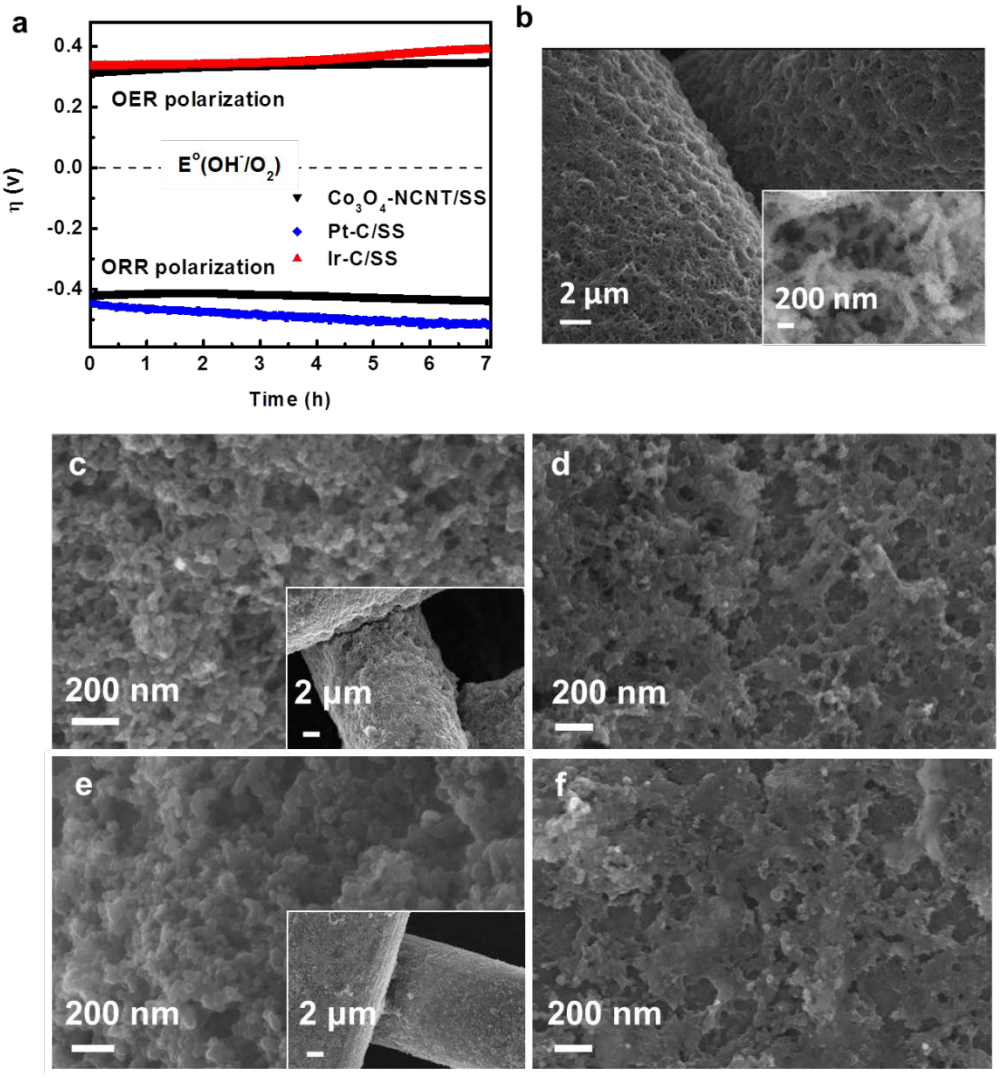

Figure 6-8. a) Chronopotentiometric measurements of the Co_3O_4-NCNT/SS, Pt-C/SS and Ir-C/SS electrodes at a constant anodic and cathodic current density of 10 mA cm^{-2} in 0.1 M KOH, respectively. b) SEM image of the Co_3O_4-NCNT/SS electrode surface after the anodic chronopotentiometric measurement over 7 h. SEM images of (c,d) Pt-C/SS and (e,f) Ir-C/SS air electrodes (c, e) before and (d, f) after chronopotentiometric measurements.

Building on the promising electrochemical activity and stability presented above, I further demonstrated the performance of the Co_3O_4-NCNT/SS air electrode using a solid-state zinc-air battery. I previously developed a thin-film battery design for flexible solid-state zinc-air

application, including a free-standing zinc film, a polymer electrolyte, a catalyst-supported carbon cloth and current collectors.[58, 135] In this regard, the current collector for the air electrode is not necessary due to sufficient electrically conductivity of the Co_3O_4-NCNT/SS electrode. This completely eliminates the voltage drop that reduces battery performance due to the interfacial resistance between the current collector and air electrode. The porous cellulose film gelled with 6M KOH served as the solid-state electrolyte. A thin-film battery (denoted as CoN-battery), assembled from the Co_3O_4-NCNT/SS air electrode, porous cellulose film and zinc electrode, is shown schematically in **Figure 6-9a**. For comparison, batteries using the Pt-C/SS and Ir-C/SS air electrodes were also fabricated through the same method and denoted as the Pt-battery and Ir-battery, respectively. **Figure 6-9b** displays discharge and charge polarization curves of the rechargeable battery using the Co_3O_4-NCNT/SS, Pt-C/SS and Ir-C/SS air electrodes. It clearly reveals that both the discharge and charge performance of the CoN-battery (black lines in **Figure 6-9b**) exhibit lower overpotentials, particularly at high current densities, than those of the Pt-battery (blue line in **Figure 6-9b**) and Ir-battery (red line in **Figure 6-9b**), respectively. The performance trends are consistent with the higher ORR and OER specific activities of Co_3O_4-NCNT/SS in **Figure 6-7a, b**. The more pronounced electrochemical performance of the Co_3O_4-NCNT air electrode is due to the large amount of accessible active Co_3O_4-NCNT nanoassembiles, which guarantees a higher power generation per unit area of the electrode. This is further evident from the fact that the CoN-battery yields a higher power density of 160.7 mW cm^{-2} than that of the Pt-battery (139.3 mW cm^{-2}) at 0.5 V (**Figure 6-9c**) due to smaller interfacial and charge-transfer resistances (**Figure 6-9d**). Additionally, the specific capacity (normalized to the mass of the zinc electrode) of the CoN-battery was

~652.6 mAh g^{-1} and ~632.3 mAh g^{-1} at a current density of 5 mA cm^{-2} and 50 mA cm^{-2} (**Figure 6-9e**), respectively, corresponding to large gravimetric energy densities of ~847.6 Wh kg^{-1} and ~802.6 Wh kg^{-1}.

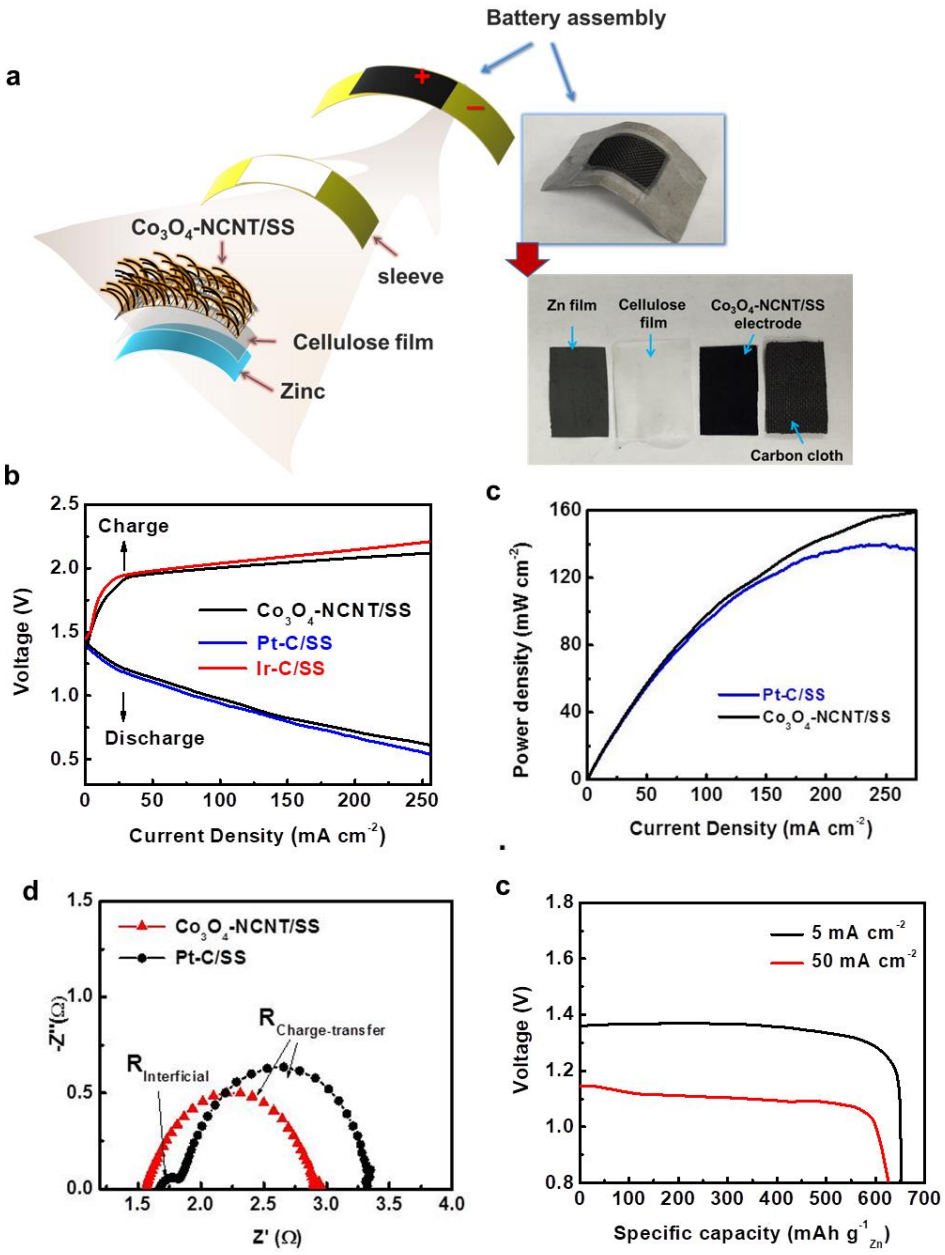

Figure 6-9. a) A schematic illustration of the flexible solid-state zinc-air battery assembly. b) Polarization curves of the battery using the Co_3O_4-NCNT/SS, Pt-C/SS and Ir-C/SS air

electrodes. c) Power density and d) Nyquist plots obtained with the Co_3O_4-NCNT/SS electrode compared to those of the Pt-C/SS electrode. e) Typical specific capacity (normalized to the mass of zinc electrode) curves of the battery using the Co_3O_4-NCNT/SS air electrode at two different current densities.

To investigate the cycle stability using the Co_3O_4-NCNT/SS air electrode, I performed galvanostatic discharge and charge testing on the CoN-battery at 25 mA cm^{-2}, with each cycle being 20 min. The short interval cycling test is an excellent diagnostic tool for examining the rechargeability of the Co_3O_4-NCNT/SS air electrode, while alleviating irreversible impacts from the zinc electrode.[215] As shown in **Figure 6-10a**, the CoN-battery was cycled over 500 h without visible voltage losses, indicative of the excellent stability and robustness of the Co_3O_4-NCNT/SS electrode. Importantly, I continued to cycle the same Co_3O_4-NCNT/SS air electrode by pairing with a fresh zinc electrode, at 25 mA cm^{-2} for an additional 80 h with a much longer cycle period (10 h) (**Figure 6-10b**). Again no significant polarization can be detected during either the discharge and charge segments. The zinc-air battery with such excellent rechargeable stability over this time-scale is strongly comparable to, or even better than, that of zinc-air batteries in tri-electrode system using the conventional air electrode configurations.[69, 79] In addition to the outstanding cycle stability, the CoN-battery shows a great potential for flexible and wearable electronic applications. The galvanodynamic discharge and charge profiles of the CoN-battery without (black solid line) and with bending (red dot line) conditions are shown in **Figure 6-10c**. The discharge and charge potentials of the rolled-up battery remain virtually unchanged compared to those of the flat battery, indicative of a robust mechanical integrity of the Co_3O_4-NCNT/SS electrode under bending. The prospect of bendable application of this device is further demonstrated in **Figure 6-10d**. Two single CoN-batteries (size 1.0×1.0 cm^2)

were connected in series and used to light a red light-emitting diode, which operates at a minimum voltage of 2.0 V.

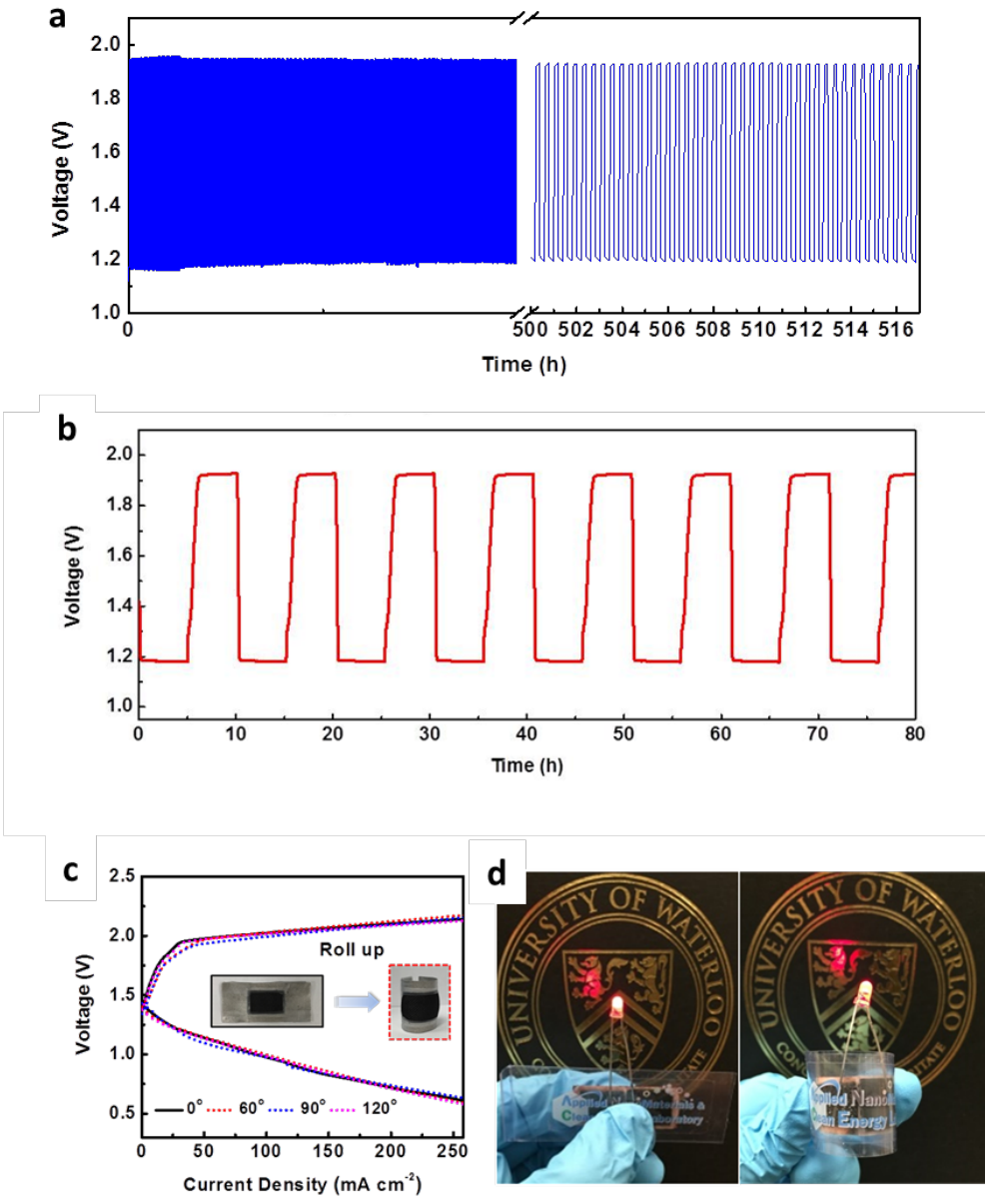

Figure 6-10. a, b) Galvanostatic charge-discharge cycling at a current density of 25 mA cm^{-2} with each cycle being 20 min (a) and 10 h (b). c) Polarization curves of the battery using the Co_3O_4-NCNT/SS air electrode under flat (black solid line) and bent (red dot line) conditions. d)

A demonstration of bendable device integrated with a tandem battery in series to power a LED under flat and bent conditions.

6.4 Conclusions

In summary, designing a nanoarchitectured catalyzed air electrode by morphologically emulating human hair could significantly extend the limits of nanostructured catalysts based on conventional planar air electrodes. Using the Co_3O_4-NCNT/SS air electrode assembly, a practical solid-state zinc-air battery is able to deliver a high energy density of ~847.6 Wh kg^{-1}, accompanied with excellent cycling stability over 600 h at a current density of 25 mA cm^{-2}. In addition to the pronounced electrochemical performance, the good mechanical flexibly of the Co_3O_4-NCNT/SS electrode allows its use in smart-wearable electronic applications. I believe that this advanced electrode design will give great freedom to further boost the electrochemical performance of zinc-air batteries beyond the scope of Co_3O_4-NCNT, through nano-engineering other heteroatom-modified CNT frameworks and transition metal oxides and chalcogenides.

Chapter 7 Conclusions and future work

7.1 Conclusions

In this thesis, approaches to polymeric electrolytes (Chapters 3, 4) and bifunctional oxygen catalyst/assembly design (Chapters 5, 6) were successfully implemented to develop a high-performance rechargeable PEMZAB. In Chapter 3, a porous KOH-doped PVA gel electrolyte was developed for rechargeable zinc-air batteries. A battery was fabricated by laminating a PVA-KOH gel electrolyte between bifunctional air electrodes comprising commercial Co_3O_4 nanoparticles coated carbon cloth and a flexible zinc film. The gel electrolyte ensured a robust adhesion to the electrodes, enabling efficient charge transport at the electrolyte-electrode interface even under bending conditions. The battery performance can be easily improved by stacking the cells in series, in parallel, or in combination of the two to meet high energy supply and high power delivery, without much increase in the physical dimensions of the overall battery due to the thin form factor of the device. In Chapter 4, a highly hydroxide ion-conductive membrane based on quaternized cellulose nanofibers was developed as both the solid alkaline electrolyte and the separator for rechargeable zinc-air batteries. The superior hydroxide-conducting property and water retention within the nanoporous structure of the QAFC membrane as well as low anisotropic swelling boosted the specific capacity and improved the cycling stability of the battery, compared to a commercial alkaline anion-exchange membrane (i.e., Tokuyama A201). A flexible zinc-air battery device was fabricated using the QAFC membrane, where virtually no power density fading nor polarization of the battery were observed for the discharge and the charge process under bending conditions. The

stable performance is also relative to its ability to inhibit zinc dendrite formation and its tolerance to CO_2 poisoning, where the precipitation of carbonates at the air electrode can be avoided.

In addition to the polymeric electrolyte design, in Chapter 5, a hybrid of cobalt oxysulfide nanoparticles and nitrogen-doped graphene nanomeshes ($CoO_{0.87}S_{0.13}$/GN) proved to be a paramount bifunctional electrocatalyst for both the ORR and OER. Moreover, the direct catalyst-membrane assembly was prepared by filtering the $CoO_{0.87}S_{0.13}$/GN catalyst suspension through a QAFC membrane. Such assembly ensures good electrode-electrolyte contact, reducing interfacial resistances and enables thinner layers of the battery assembly. Benefiting from the performance improvement of the QAFC electrolyte membrane and the $CoO_{0.87}S_{0.13}$/GN bifunctional catalyst, the resulting battery possesses a higher energy density of 857.9 Wh kg^{-1} and a more stable cycling performance over 300 hours of operation under ambient conditions, with a lower discharge-charge voltage gap of 0.77 V at 20 mA cm^{-2}, than those of a battery using PVA-KOH gel membrane and a Co_3O_4 bifunctional catalysts. Despite notable advancement in the design of the $CoO_{0.87}S_{0.13}$/GN bifunctional catalyst, there still remains much room for further improvements in the practical performance of the air electrode assembly. In Chapter 6, an integrated bifunctional air electrode, consisting of a stainless steel mesh substrate with a directly coupled Co_3O_4-NCNT bifunctional catalyst in a 3D architecture, was designed for rechargeable zinc-air batteries. Such integrative design not only ensures a large number of catalytically active sites in a given electrode surface, but also increases the electron transfer between each individual catalyst and the conductive substrate. Using the Co_3O_4-NCNT/SS air electrode, a practical solid-state zinc-air battery is able to deliver a high

energy density of 847.6 Wh kg^{-1}, accompanied with excellent cycling stability over 600h at a current density of 25 mA cm^{-2}. Moreover, the zinc-air battery using this electrode exhibits superior mechanical flexibly, allowing its use in flexible and wearable electronic applications.

7.2 Recommended future work

Based on the results from the studies conducted in this thesis research, the following recommendations are proposed for future work.

1. *Further investigations on the CNF-size and inorganic nanofillers effect on the performance of CNF-based polymer electrolyte membranes*. Cellulose nanofibers (CNF) are very attractive due to their high mechanical strengths and one-dimensional structure with a large surface area possessing a large number of hydroxyl groups, which can be chemically, thermally, or electrochemically engineered. In this study, functionalization of a type of CNF to develop a both superionic and mechanical robust polymer electrolyte has already produced some promising results. Further investigation on the size effect of CNF may provide valuable insight into the design of improved CNF-based polymer electrolytes. The formation of hierarchical porous structures (i.e. micro-, meso-, macropores) can be controlled by the sizes of CNF. These hierarchical architectures are expected to tune the ionic conductivity in terms of water uptake and ion-exchange capacities in the membrane. Moreover, it is recommended that an investigation on the incorporation of inorganic nanofillers for the CNF-based composite polymer electrolyte membranes be performed. For instance, graphene oxides (GO) can be used as effective nanofillers to enhance the physiochemical properties and ionic conductivities of the CNF-based composite membrane. Because of the strong interaction (i.e. hydrogen bonding) between CNF skeleton and GO nanosheets, it endows the laminated membrane to resist severe

swelling under a high degree of functionalization and hydration. Moreover, the interconnection and chemical interaction between CNF and GO nanosheets can be further improved by crosslinking methods, resulting in a significant improvement of mechanical strength and structural stability. Upon incorporation into CNF, unique nanochannels among stacked GO can be artificially regulated or designed during the deposition processes. These nanochannels are controlled to allow for hydroxide ion conduction while realizing zincate ions rejection mainly through the size exclusion of the nanochannels formed by stacked GO sheets.

2. *Further investigations on the defects control of the hybrid catalyst/current collector assembly towards high catalytic performance.* In Chapter 5, the role of oxygen vacancy defects in cobalt oxysulfides was demonstrated to be positive in catalyst improvement. In Chapter 6, a 3D hybrid catalyst/current collector assembly, consisting of Co_3O_4-NCNT hybrid catalysts vertically and directly grown on the stainless-steel mesh, was also successfully demonstrated on in a rechargeable zinc-air battery. A combination of these two strategies could inform the next round of advanced catalyst development, through introducing oxygen vacancy defects into the 3D Co_3O_4-NCNT nanostructures, to attain the greatest improvement in electrode activity. In this case, the electrode activity can be improved by (i) increasing the intrinsic activity of each catalytically active site (through defect control), and (ii) increasing the number of active sites on a given electrode surface (through the 3D nanostructures).

3. *Device optimization*. This study focused on the development of polymer electrolytes and nanostructured bifunctional oxygen catalysts for a rechargeable PEMZAB. The 2D cell architecture (i.e., multilayer structure) is selected for ease of fabrication and testing rather than for device performance optimization. The adjustment of the cell architecture can further lead to

significant improvements on electrochemical performance, such as the areal energy density. For instance, a 3D and interpenetrated architecture (**Figure 7-1**) based on a high-surface area aerogel was demonstrated on increasing the areal energy density of a 3D battery.[216] Such architecture can inform 3D integration of the zinc-air battery components by increasing the amount of electrolyte and electrode interfaces while maintaining short hydroxide ion transport distances between the electrodes. This battery architecture can provide better areal energy density without sacrificing power performance. Moreover, understanding of the effects of 3D architectures on the interfacial reaction kinetics, mass transport behaviors within the cell, and overall device performance will require new research including characterization and modeling capabilities.

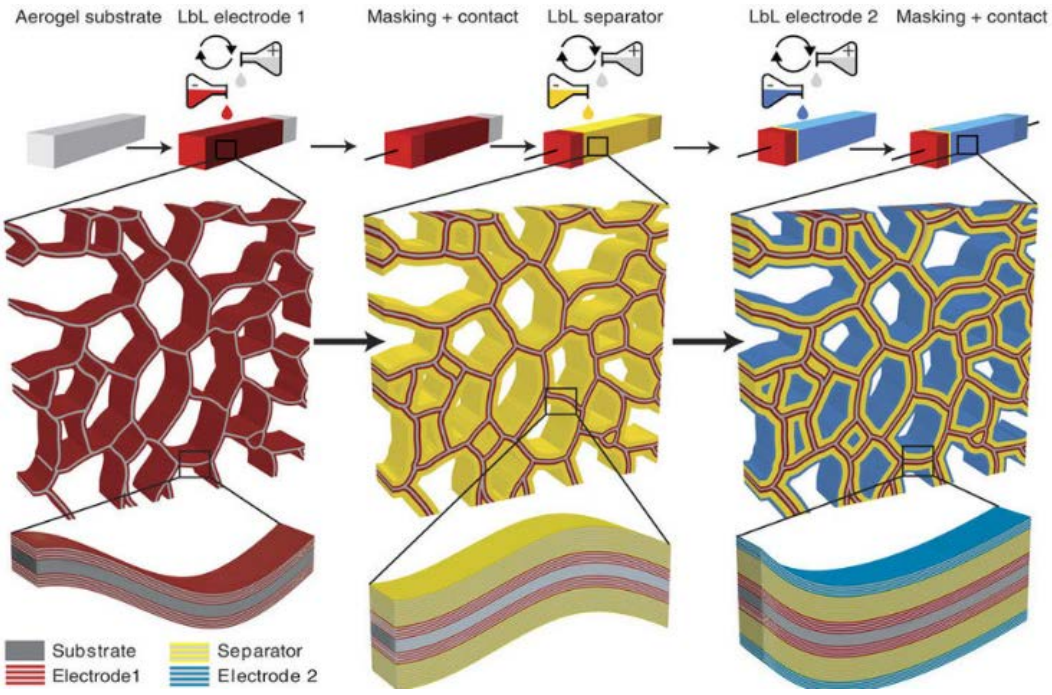

Figure 7-1. Schematics of the layer-by-layer process used to assemble 3D devices in an aerogel. Reproduced from reference[216], with permission from Nature Publishing Group.

References

1. MacKenzie, J. D.; Ho, C. *Proceedings of the IEEE* **2015,** 103, (4), 535-553.
2. Shen, G.; Fan, Z., *Flexible Electronics: From Materials to Devices*. 2016.
3. Tarascon, J. M.; Armand, M. *Nature* **2001,** 414, (6861), 359-367.
4. Fu, J.; Cano, Z. P.; Park, M. G.; Yu, A.; Fowler, M.; Chen, Z. *Advanced Materials* **2017,** 29, (7), 1604685.
5. Lee, J. S.; Tai Kim, S.; Cao, R.; Choi, N. S.; Liu, M.; Lee, K. T.; Cho, J. *Advanced Energy Materials* **2011,** 1, (1), 34-50.
6. Winter, M.; Brodd, R. J., What are batteries, fuel cells, and supercapacitors? ACS Publications: 2004.
7. Wang, Y.-J.; Qiao, J.; Baker, R.; Zhang, J. *Chemical Society Reviews* **2013,** 42, (13), 5768-5787.
8. Zarrin, H.; Fu, J.; Jiang, G.; Yoo, S.; Lenos, J.; Fowler, M.; Chen, Z. *ACS Nano* **2015,** 9, (2), 2028-2037.
9. Janek, J.; Zeier, W. G. *Nature Energy* **2016,** 1, 16141.
10. Klingele, M.; Breitwieser, M.; Zengerle, R.; Thiele, S. *Journal of Materials Chemistry A* **2015,** 3, (21), 11239-11245.
11. Wehkamp, N.; Breitwieser, M.; Buchler, A.; Klingele, M.; Zengerle, R.; Thiele, S. *RSC Advances* **2016,** 6, (29), 24261-24266.
12. Breitwieser, M.; Bayer, T.; Büchler, A.; Zengerle, R.; Lyth, S. M.; Thiele, S. *Journal of Power Sources* **2017,** 351, 145-150.
13. Breitwieser, M.; Klingele, M.; Vierrath, S.; Zengerle, R.; Thiele, S. *Advanced Energy Materials*, 1701257.
14. Lee, D. U.; Xu, P.; Cano, Z. P.; Kashkooli, A. G.; Park, M. G.; Chen, Z. *Journal of Materials Chemistry A* **2016,** 4, (19), 7107-7134.
15. Seh, Z. W.; Kibsgaard, J.; Dickens, C. F.; Chorkendorff, I.; Nørskov, J. K.; Jaramillo, T. F. *Science* **2017,** 355, (6321), 4998.
16. Lee, D. U.; Choi, J. Y.; Feng, K.; Park, H. W.; Chen, Z. *Advanced Energy Materials* **2014,** 4, 1301389.
17. R. Mainar, A.; Leonet, O.; Bengoechea, M.; Boyano, I.; de Meatza, I.; Kvasha, A.; Guerfi, A.; Alberto Blázquez, J. *International Journal of Energy Research* **2016,** 40, (8), 1032-1049.
18. Appleby, A. J.; Jacquelin, J.; Pompon, J. P., Charge-Discharge Behavior of the C.G.E. Circulating Zinc-Air Vehicle Battery. SAE International: 1977.
19. Cheiky, M. C.; Danczyk, L. G.; Wehrey, M. C., Second-Generation Zinc-Air Powered Electric Minivans. SAE International: 1992.
20. Goldstein, J.; Brown, I.; Koretz, B. *Journal of Power Sources* **1999,** 80, (1), 171-179.
21. Cheiky, M. C.; Danczyk, L. G.; Wehrey, M. C., Rechargeable Zinc-Air Batteries in Electric Vehicle Applications. SAE International: 1990.
22. Cheiky, M. C.; Danczyk, L. G.; Scheffler, R. L., Zinc-Air Powered Electric Vehicle Systems Integration Issues. SAE International: 1991.

23. Tweed, K. Eos Energy Storage Closes $23M Funding Round for Cheap Grid Batteries, http://www.greentechmedia.com/articles/read/eos-energy-storage-closes-23m-funding-round (accessed: July 2016).
24. Wesoff, E. Fluidic Energy Is the Biggest Zinc–air Battery Startup You Haven't Heard Of, http://www.greentechmedia.com/articles/read/Fluidic-Energy-is-the-Biggest-Zinc-air-Battery-Startup-You-Havent-Heard-Of (accessed: August 2016).
25. N. R. C. Government of Canada, Archived – Government of Canada and SDTC Announce New Clean Technology Funding in British Columbia, http://news.gc.ca/web/article-en.do?nid = 950589 (accessed: August 2016).
26. Nykvist, B.; Nilsson, M. *Nature Clim. Change* **2015,** 5, (4), 329-332.
27. Khan, P. A.; Venkatesh, B. in *Smart City 360°*, (Eds: A. Leon-Garcia, R. Lenort, D. Holman, D. Staš, V. Krutilova, P. Wicher, D. Cagánˇová, D. Špirková, J. Golej, K. Nguyen), Springer International Publishing, Cham, Switzerland 2016, 277–291.
28. Hong, W.; Li, H.; Wang, B. *International Journal of Electrochemical Science* **2016,** 11, 3843-3851.
29. Ma, H.; Wang, B.; Fan, Y.; Hong, W. *Energies* **2014,** 7, (10), 6549.
30. Li, P.-C.; Chien, Y.-J.; Hu, C.-C. *Journal of Power Sources* **2016,** 313, 37-45.
31. Park, M. G.; Lee, D. U.; Seo, M. H.; Cano, Z. P.; Chen, Z. *Small* **2016,** 12, (20), 2707-2714.
32. Gaikwad, A. M.; Whiting, G. L.; Steingart, D. A.; Arias, A. C. *Advanced Materials* **2011,** 23, (29), 3251-3255.
33. Wang, X.; Lu, X.; Liu, B.; Chen, D.; Tong, Y.; Shen, G. *Advanced Materials* **2014,** 26, (28), 4763-4782.
34. Fu, J.; Lee, D. U.; Hassan, F. M.; Yang, L.; Bai, Z.; Park, M. G.; Chen, Z. *Advanced Materials* **2015,** 27, (37), 5617-5622.
35. Fu, J.; Zhang, J.; Song, X.; Zarrin, H.; Tian, X.; Qiao, J.; Rasen, L.; Li, K.; Chen, Z. *Energy & Environmental Science* **2016,** 9, (2), 663-670.
36. Liu, Q.; Wang, Y.; Dai, L.; Yao, J. *Advanced Materials* **2016**, 28, 3000–3006.
37. Park, J.; Park, M.; Nam, G.; Lee, J.-s.; Cho, J. *Advanced Materials* **2015,** 27, (8), 1396-1401.
38. Hu, Y.; Sun, X. *Journal of Materials Chemistry A* **2014,** 2, (28), 10712-10738.
39. Zheng, G.; Hu, L.; Wu, H.; Xie, X.; Cui, Y. *Energy & Environmental Science* **2011,** 4, (9), 3368-3373.
40. Wang, K.; Luo, S.; Wu, Y.; He, X.; Zhao, F.; Wang, J.; Jiang, K.; Fan, S. *Advanced Functional Materials* **2013,** 23, (7), 846-853.
41. Hu, L.; Wu, H.; La Mantia, F.; Yang, Y.; Cui, Y. *ACS nano* **2010,** 4, (10), 5843-5848.
42. Hu, L.; Choi, J. W.; Yang, Y.; Jeong, S.; La Mantia, F.; Cui, L.-F.; Cui, Y. *Proceedings of the National Academy of Sciences* **2009,** 106, (51), 21490-21494.
43. Li, X.; Yang, J.; Hu, Y.; Wang, J.; Li, Y.; Cai, M.; Li, R.; Sun, X. *Journal of Materials Chemistry* **2012,** 22, (36), 18847-18853.
44. Hu, Y.; Li, X.; Geng, D.; Cai, M.; Li, R.; Sun, X. *Electrochimica Acta* **2013,** 91, 227-233.
45. Zhao, C.; Zhang, J.; Hu, Y.; Robertson, N.; Hu, P. A.; Child, D.; Gibson, D.; Fu, Y. Q. *Scientific Reports* **2015,** 5, 17750.

46. Zhang, Y.; Xia, X.; Kang, J.; Tu, J. *Chinese Science Bulletin* **2012,** 57, (32), 4215-4219.
47. Qu, Q.; Zhang, J.-H.; Wang, J.; Li, Q.-Y.; Xu, C.-W.; Lu, X. *Scientific Reports* **2017,** 7, 41542.
48. Burke, M. S.; Enman, L. J.; Batchellor, A. S.; Zou, S.; Boettcher, S. W. *Chemistry of Materials* **2015,** 27, (22), 7549-7558.
49. Li, Z.; Zhang, J. T.; Chen, Y. M.; Li, J.; Lou, X. W. *Nature Communications* **2015,** 6, 8850.
50. Koo, M.; Park, K.I.; Lee, S. H.; Suh, M.; Jeon, D. Y.; Choi, J. W.; Kang, K.; Lee, K. J. *Nano Letters* **2012,** 12, (9), 4810-4816.
51. Li, N.; Chen, Z.; Ren, W.; Li, F.; Cheng, H.-M. *Proceedings of the National Academy of Sciences* **2012,** 109, (43), 17360-17365.
52. Fu, Y.; Cai, X.; Wu, H.; Lv, Z.; Hou, S.; Peng, M.; Yu, X.; Zou, D. *Advanced Materials* **2012,** 24, (42), 5713-5718.
53. Kwon, Y. H.; Woo, S.-W.; Jung, H.-R.; Yu, H. K.; Kim, K.; Oh, B. H.; Ahn, S.; Lee, S.-Y.; Song, S.-W.; Cho, J.; Shin, H.-C.; Kim, J. Y. *Advanced Materials* **2012,** 24, (38), 5192-5197.
54. Jost, K.; Perez, C. R.; McDonough, J. K.; Presser, V.; Heon, M.; Dion, G.; Gogotsi, Y. *Energy & Environmental Science* **2011,** 4, (12), 5060-5067.
55. Kwon, Y. H.; Woo, S. W.; Jung, H. R.; Yu, H. K.; Kim, K.; Oh, B. H.; Ahn, S.; Lee, S. Y.; Song, S. W.; Cho, J. *Advanced Materials* **2012,** 24, (38), 5192-5197.
56. Sun, K. E. K.; Hoang, T. K. A.; Doan, T. N. L.; Yu, Y.; Zhu, X.; Tian, Y.; Chen, P. *ACS Applied Materials & Interfaces* **2017,** 9, (11), 9681-9687.
57. Schröder, D.; Arlt, T.; Krewer, U.; Manke, I. *Electrochemistry Communications* **2014,** 40, 88-91.
58. Fu, J.; Zhang, J.; Song, X.; Zarrin, H.; Tian, X.; Qiao, J.; Rasen, L.; Li, K.; Chen, Z. *Energy & Environmental Science* **2016,** 9, (2), 663-670.
59. Smitha, B.; Sridhar, S.; Khan, A. *Journal of membrane science* **2005,** 259, (1), 10-26.
60. Yang, C.C.; Lin, S.J. *Journal of Power Sources* **2002,** 112, (2), 497-503.
61. Hilder, M.; Winther-Jensen, B.; Clark, N. B. *Journal of Power Sources* **2009,** 194, (2), 1135-1141.
62. Mohamad, A. A. *Journal of Power Sources* **2006,** 159, (1), 752-757.
63. Wu, G. M.; Lin, S. J.; Yang, C. C. *Journal of Membrane Science* **2006,** 280, (1-2), 802-808.
64. Kim, H.-W.; Lim, J.-M.; Lee, H.-J.; Eom, S.-W.; Hong, Y. T.; Lee, S.-Y. *Journal of Materials Chemistry A* **2016,** 4, (10), 3711-3720.
65. Hwang, H. J.; Chi, W. S.; Kwon, O.; Lee, J. G.; Kim, J. H.; Shul, Y.-G. *ACS Applied Materials & Interfaces* **2016,** 8, (39), 26298-26308.
66. Kim, H.-W.; Lim, J.-M.; Lee, H.-J.; Eom, S.-W.; Hong, Y. T.; Lee, S.-Y. *Journal of Materials Chemistry A* **2016,** 4, (10), 3711-3720.
67. Varcoe, J. R.; Slade, R. C. *Fuel cells* **2005,** 5, (2), 187-200.
68. Smitha, B.; Sridhar, S.; Khan, A. A. *Journal of Membrane Science* **2005,** 259, (1), 10-26.
69. Li, Y.; Gong, M.; Liang, Y.; Feng, J.; Kim, J.-E.; Wang, H.; Hong, G.; Zhang, B.; Dai, H. *Nature Communications* **2013,** 4, 1805.

70. Guo, S.; Zhang, S.; Sun, S. *Angewandte Chemie International Edition* **2013,** 52, (33), 8526-8544.
71. Jörissen, L. *Journal of Power Sources* **2006,** 155, (1), 23-32.
72. Lee, D. U.; Scott, J.; Park, H. W.; Abureden, S.; Choi, J.-Y.; Chen, Z. *Electrochemistry Communications* **2014,** 43, 109-112.
73. Chen, Z.; Yu, A.; Ahmed, R.; Wang, H.; Li, H.; Chen, Z. *Electrochimica Acta* **2012,** 69, 295-300.
74. Lee, D. U.; Kim, B. J.; Chen, Z. *Journal of Materials Chemistry A* **2013,** 1, (15), 4754.
75. Li, G.; Wang, X.; Fu, J.; Li, J.; Park, M. G.; Zhang, Y.; Lui, G.; Chen, Z. *Angewandte Chemie* **2016,** 128, (16), 5061-5066.
76. Lee, D. U.; Park, M. G.; Park, H. W.; Seo, M. H.; Wang, X.; Chen, Z. *ChemSusChem* **2015,** 8, (18), 3129-3138.
77. Lee, D. U.; Park, H. W.; Park, M. G.; Ismayilov, V.; Chen, Z. *ACS Applied Materials & Interfaces* **2015,** 7, (1), 902-910.
78. Yang, H. B.; Miao, J.; Hung, S.-F.; Chen, J.; Tao, H. B.; Wang, X.; Zhang, L.; Chen, R.; Gao, J.; Chen, H. M.; Dai, L.; Liu, B. *Science Advances* **2016,** 2, 1501122.
79. Zhang, J.; Zhao, Z.; Xia, Z.; Dai, L. *Nature Nanotechnology* **2015,** 10, (5), 444-452.
80. Zhang, J.; Qu, L.; Shi, G.; Liu, J.; Chen, J.; Dai, L. *Angewandte Chemie International Edition* **2016,** 55, (6), 2230-2234.
81. Qu, K.; Zheng, Y.; Dai, S.; Qiao, S. Z. *Nano Energy* **2016,** 19, 373-381.
82. Lee, D. U.; Xu, P.; Cano, Z. P.; Kashkooli, A. G.; Park, M. G.; Chen, Z. *Journal of Materials Chemistry A* **2016,** 4, (19), 7107-7134.
83. Song, C.; Zhang, J., Electrocatalytic Oxygen Reduction Reaction. In *PEM Fuel Cell Electrocatalysts and Catalyst Layers: Fundamentals and Applications*, Zhang, J., Ed. Springer London: London, 2008, 89-134.
84. Cao, R.; Lee, J.-S.; Liu, M.; Cho, J. *Advanced Energy Materials* **2012,** 2, (7), 816-829.
85. Kinoshita, K., *Electrochemical Oxygen Technology*. John Wiley & Sons: 1992.
86. Ge, X.; Sumboja, A.; Wuu, D.; An, T.; Li, B.; Goh, F. W. T.; Hor, T. S. A.; Zong, Y.; Liu, Z. *ACS Catalysis* **2015,** 5, (8), 4643-4667.
87. Park, S.-A.; Lee, E.-K.; Song, H.; Kim, Y.-T. *Scientific Reports* **2015,** 5, 13552.
88. He, H.; Lei, Y.; Xiao, C.; Chu, D.; Chen, R.; Wang, G. *The Journal of Physical Chemistry C* **2012,** 116, (30), 16038-16046.
89. Cao, R.; Thapa, R.; Kim, H.; Xu, X.; Gyu Kim, M.; Li, Q.; Park, N.; Liu, M.; Cho, J. *Nature Communications* **2013,** 4, 2076.
90. Sunarso, J.; Torriero, A. A. J.; Zhou, W.; Howlett, P. C.; Forsyth, M. *The Journal of Physical Chemistry C* **2012,** 116, (9), 5827-5834.
91. Wang, Y.; Cheng, H.-P. *The Journal of Physical Chemistry C* **2013,** 117, (5), 2106-2112.
92. Qu, L.; Liu, Y.; Baek, J.-B.; Dai, L. *ACS Nano* **2010,** 4, (3), 1321-1326.
93. Zhang, S.; Cai, Y.; He, H.; Zhang, Y.; Liu, R.; Cao, H.; Wang, M.; Liu, J.; Zhang, G.; Li, Y.; Liu, H.; Li, B. *Journal of Materials Chemistry A* **2016,** 4, (13), 4738-4744.
94. Trotochaud, L.; Boettcher, S. W. *Scripta Materialia* **2014,** 74, 25-32.
95. Reier, T.; Oezaslan, M.; Strasser, P. *ACS Catalysis* **2012,** 2, (8), 1765-1772.
96. Tseung, A.; Jasem, S. *Electrochimica Acta* **1977,** 22, (1), 31-34.

97. Lu, X.; Zhao, C. *Journal of Materials Chemistry A* **2013,** 1, (39), 12053-12059.
98. Rosen, J.; Hutchings, G. S.; Jiao, F. *Journal of the American Chemical Society* **2013,** 135, (11), 4516-4521.
99. Jin, H.; Wang, J.; Su, D.; Wei, Z.; Pang, Z.; Wang, Y. *Journal of the American Chemical Society* **2015,** 137, (7), 2688-2694.
100. Hutchings, G. S.; Zhang, Y.; Li, J.; Yonemoto, B. T.; Zhou, X.; Zhu, K.; Jiao, F. *Journal of the American Chemical Society* **2015,** 137, (12), 4223-4229.
101. Zhu, C.; Wen, D.; Leubner, S.; Oschatz, M.; Liu, W.; Holzschuh, M.; Simon, F.; Kaskel, S.; Eychmuller, A. *Chemical Communications* **2015,** 51, (37), 7851-7854.
102. Wu, G.; Li, N.; Zhou, D.-R.; Mitsuo, K.; Xu, B.-Q. *Journal of Solid State Chemistry* **2004,** 177, (10), 3682-3692.
103. Yang, Y.; Fei, H.; Ruan, G.; Xiang, C.; Tour, J. M. *ACS nano* **2014,** 8, (9), 9518-9523.
104. Otagawa, T.; Bockris, J. O. M. *Journal of The Electrochemical Society* **1982,** 129, (10), 2391-2392.
105. Bockris, J. O. M.; Ottagawa, T., Lanthanum nickelate perovskite-type oxide for the anodic oxygen evolution catalyst. Google Patents: 1985.
106. Jung, S.; McCrory, C. C.; Ferrer, I. M.; Peters, J. C.; Jaramillo, T. F. *Journal of Materials Chemistry A* **2016,** 4, (8), 3068-3076.
107. Wang, Z.-L.; Xu, D.; Xu, J.-J.; Zhang, X.-B. *Chemical Society Reviews* **2014,** 43, (22), 7746-7786.
108. Sadeghifar, H.; Djilali, N.; Bahrami, M. *Journal of Power Sources* **2014,** 248, 632-641.
109. Davari, E.; Johnson, A. D.; Mittal, A.; Xiong, M.; Ivey, D. G. *Electrochimica Acta* **2016,** 211, 735-743.
110. Burchardt, T., Metal-Air Battery or Fuel Cell. Google Patents: 2008.
111. Suren, S.; Kheawhom, S. *Journal of The Electrochemical Society* **2016,** 163, (6), A846-A850.
112. Yan, W.-M.; Hsueh, C.-Y.; Soong, C.-Y.; Chen, F.; Cheng, C.-H.; Mei, S.-C. *International Journal of Hydrogen Energy* **2007,** 32, (17), 4452-4458.
113. Park, S. B.; Park, Y.-i. *International Journal of Precision Engineering and Manufacturing* **2012,** 13, (7), 1145-1151.
114. Haas, O.; Van Wesemael, J., SECONDARY BATTERIES – METAL-AIR SYSTEMS | Zinc–Air: Electrical Recharge A2 - Garche, Jürgen. In *Encyclopedia of Electrochemical Power Sources*, Elsevier: Amsterdam, 2009, 384-392.
115. Park, J.; Oh, H.; Ha, T.; Lee, Y. I.; Min, K. *Applied Energy* **2015,** 155, 866-880.
116. Ma, Z.; Pei, P.; Wang, K.; Wang, X.; Xu, H.; Liu, Y.; peng, G. *Journal of Power Sources* **2015,** 274, 56-64.
117. Chen, Z.; Lee, D. U., Single layer air electrode and processes for the production thereof. Google Patents: 2015.
118. Bockelmann, M.; Kunz, U.; Turek, T. *Electrochemistry Communications* **2016,** 69, 24-27.
119. Li, X.; Pletcher, D.; Russell, A. E.; Walsh, F. C.; Wills, R. G. A.; Gorman, S. F.; Price, S. W. T.; Thompson, S. J. *Electrochemistry Communications* **2013,** 34, 228-230.
120. Price, S. W. T.; Thompson, S. J.; Li, X.; Gorman, S. F.; Pletcher, D.; Russell, A. E.; Walsh, F. C.; Wills, R. G. A. *Journal of Power Sources* **2014,** 259, 43-49.

121. Büker, F.; Hertkorn, D.; Müller, C.; Reinecke, H. *ECS Transactions* **2014,** 58, (36), 69-74.
122. Allebrod, F.; Chatzichristodoulou, C.; Mogensen, M. B. *ECS Transactions* **2014,** 64, (3), 1029-1038.
123. Liu, X.; Park, M.; Kim, M. G.; Gupta, S.; Wang, X.; Wu, G.; Cho, J. *Nano Energy* **2016,** 20, 315-325.
124. Brost, R. D.; Weisenstein, A.; Brost, K. M.; Wilkins, H. F.; Kosted, R. M., Air electrodes including perovskites. Google Patents: 2014.
125. Fu, J.; Hassan, F. M.; Li, J.; Lee, D. U.; Ghannoum, A. R.; Lui, G.; Hoque, M. A.; Chen, Z. *Advanced Materials* **2016**, , 28, 6421–6428.
126. Xu, Y.; Zhang, Y.; Guo, Z.; Ren, J.; Wang, Y.; Peng, H. *Angewandte Chemie International Edition* **2015,** 54, (51), 15390-15394.
127. Wu, X.; Chen, F.; Jin, Y.; Zhang, N.; Johnston, R. L. *ACS Applied Materials & Interfaces* **2015,** 7, (32), 17782-17791.
128. Ng, J. W. D.; Tang, M.; Jaramillo, T. F. *Energy & Environmental Science* **2014,** 7, (6), 2017-2024.
129. Meng, F.; Zhong, H.; Bao, D.; Yan, J.; Zhang, X. *Journal of the American Chemical Society* **2016**, 138 (32), 10226–10231.
130. Sumboja, A.; Ge, X.; Goh, F. W. T.; Li, B.; Geng, D.; Hor, T. S. A.; Zong, Y.; Liu, Z. *ChemPlusChem* **2015,** 80, (8), 1341-1346.
131. Li, B.; Ge, X.; Goh, F. W. T.; Hor, T. S. A.; Geng, D.; Du, G.; Liu, Z.; Zhang, J.; Liu, X.; Zong, Y. *Nanoscale* **2015,** 7, (5), 1830-1838.
132. Lee, C. H.; Park, H. B.; Lee, Y. M.; Lee, R. D. *Industrial & Engineering Chemistry Research* **2005,** 44, (20), 7617-7626.
133. Hong, W. T.; Risch, M.; Stoerzinger, K. A.; Grimaud, A.; Suntivich, J.; Shao-Horn, Y. *Energy & Environmental Science* **2015,** 8, (5), 1404-1427.
134. https://www.pineresearch.com/shop/knowledgebase/rotating-electrode-theory/.
135. Fu, J.; Lee, D. U.; Hassan, F. M.; Yang, L.; Bai, Z.; Park, M. G.; Chen, Z. *Adv. Mater.* **2015,** 27, (37), 5617-5622.
136. Chen, Z.; Yu, A.; Higgins, D.; Li, H.; Wang, H.; Chen, Z. *Nano Letters* **2012,** 12, (4), 1946-1952.
137. Lee, D. U.; Choi, J.-Y.; Feng, K.; Park, H. W.; Chen, Z. *Advanced Energy Materials* **2014,** 4, (6), 1301389.
138. Qiao, J.; Fu, J.; Lin, R.; Ma, J.; Liu, J. *Polymer* **2010,** 51, (21), 4850-4859.
139. Fu, J.; Qiao, J.; Wang, X.; Ma, J.; Okada, T. *Synthetic Metals* **2010,** 160, (1), 193-199.
140. Zhang, G.; Zhang, X. *Solid State Ionics* **2003,** 160, (1), 155-159.
141. Yang, C. C.; Lin, S. J.; Huang, C. N.; Chiu, J. M., Method for preparing solid-state polymer zinc-air battery. Google Patents: 2007.
142. Wang, Z.; Wu, Z.; Bramnik, N.; Mitra, S. *Advanced Materials* **2014,** 26, (6), 970-976.
143. Gaikwad, A. M.; Whiting, G. L.; Steingart, D. A.; Arias, A. C. *Advanced Materials* **2011,** 23, (29), 3251-3255.
144. Chae, S.-K.; Mun, C. H.; Noh, D.-Y.; Kang, E.; Lee, S.-H. *Langmuir* **2014,** 30, (41), 12107-12113.

145. Fei, H.; Yang, C.; Bao, H.; Wang, G. *Journal of Power Sources* **2014,** 266, (1), 488-495.
146. Lee, D. U.; Park, H. W.; Park, M. G.; Ismayilov, V.; Chen, Z. *ACS Appl. Mater. Interfaces* **2014,** 7, (1), 902-910.
147. Cheng, Q.; Song, Z.; Ma, T.; Smith, B. B.; Tang, R.; Yu, H.; Jiang, H.; Chan, C. K. *Nano Letters* **2013,** 13, (10), 4969-4974.
148. Winter, M.; Brodd, R. J. *Chemical Reviews* **2004,** 104, (10), 4245-4270.
149. El-Kady, M. F.; Strong, V.; Dubin, S.; Kaner, R. B. *Science* **2012,** 335, (6074), 1326-1330.
150. Gui, Z.; Zhu, H.; Gillette, E.; Han, X.; Rubloff, G. W.; Hu, L.; Lee, S. B. *ACS Nano* **2013,** 7, (7), 6037-6046.
151. Zhu, H.; Xiao, Z.; Liu, D.; Li, Y.; Weadock, N. J.; Fang, Z.; Huang, J.; Hu, L. *Energy & Environmental Science* **2013,** 6, (7), 2105-2111.
152. Zhu, H.; Fang, Z.; Preston, C.; Li, Y.; Hu, L. *Energy & Environmental Science* **2014,** 7, (1), 269-287.
153. Lu, X.; Yu, M.; Wang, G.; Tong, Y.; Li, Y. *Energy & Environmental Science* **2014,** 7, (7), 2160-2181.
154. Fang, Z.; Zhu, H.; Bao, W.; Preston, C.; Liu, Z.; Dai, J.; Li, Y.; Hu, L. *Energy & Environmental Science* **2014,** 7, (10), 3313-3319.
155. Hu, L.; Zheng, G.; Yao, J.; Liu, N.; Weil, B.; Eskilsson, M.; Karabulut, E.; Ruan, Z.; Fan, S.; Bloking, J. T.; McGehee, M. D.; Wagberg, L.; Cui, Y. *Energy & Environmental Science* **2013,** 6, (2), 513-518.
156. Wei, H.; Rodriguez, K.; Renneckar, S.; Vikesland, P. J. *Environmental Science: Nano* **2014,** 1, (4), 302-316.
157. Andresen, M.; Stenstad, P.; Møretrø, T.; Langsrud, S.; Syverud, K.; Johansson, L.-S.; Stenius, P. *Biomacromolecules* **2007,** 8, (7), 2149-2155.
158. Yun, S.; Kang, K. S.; Kim, J. *Polymer International* **2010,** 59, (8), 1071-1076.
159. Zhao, Y.; Nakamura, R.; Kamiya, K.; Nakanishi, S.; Hashimoto, K. *Nat Commun* **2013,** 4.
160. Gu, S.; Skovgard, J.; Yan, Y. S. *ChemSusChem* **2012,** 5, (5), 843-848.
161. Park, S.; Baker, J.; Himmel, M.; Parilla, P.; Johnson, D. *Biotechnol Biofuels* **2010,** 3, (1), 1-10.
162. Duan, Q.; Ge, S.; Wang, C.-Y. *Journal of Power Sources* **2013,** 243, 773-778.
163. Mishra, S. P., *A Text Book of Fibre Science and Technology*. New Age International: 2000.
164. Park, Y.-S.; Yamazaki, Y. *Journal of Membrane Science* **2005,** 261, (1–2), 58-66.
165. Kiss, A. M.; Myles, T. D.; Grew, K. N.; Peracchio, A. A.; Nelson, G. J.; Chiu, W. K. S. *Journal of The Electrochemical Society* **2013,** 160, (9), F994-F999.
166. Lu, J.; Askeland, P.; Drzal, L. T. *Polymer* **2008,** 49, (5), 1285-1296.
167. Kumar, B.; Asadi, M.; Pisasale, D.; Sinha-Ray, S.; Rosen, B. A.; Haasch, R.; Abiade, J.; Yarin, A. L.; Salehi-Khojin, A. *Nature Commununications* **2013,** 4, 2819.
168. Henriksson, M.; Berglund, L. A.; Isaksson, P.; Lindström, T.; Nishino, T. *Biomacromolecules* **2008,** 9, (6), 1579-1585.

169. Jianhua, F.; Xiaoxia, G., Phosphoric Acid?Doped Polybenzimidazole Membranes for High-Temperature Proton Exchange Membrane Fuel Cells. In *Electrochemical Polymer Electrolyte Membranes*, CRC Press: 2015,315-364.
170. Fu, J.; Qiao, J.; Lv, H.; Ma, J.; Yuan, X.-Z.; Wang, H. *ECS Transactions* **2010,** 25, (13), 15-23.
171. Qiao, J.; Fu, J.; Liu, L.; Liu, Y.; Sheng, J. *Int. J. Hydrogen Energy* **2012,** 37, (5), 4580-4589.
172. Ren, X.; Price, S. C.; Jackson, A. C.; Pomerantz, N.; Beyer, F. L. *ACS Applied Materials & Interfaces* **2014,** 6, (16), 13330-13333.
173. Li, Y.; Dai, H. *Chemical Society Reviews* **2014,** 43, (15), 5257-5275.
174. Cheng, F.; Shen, J.; Peng, B.; Pan, Y.; Tao, Z.; Chen, J. *Nat Chem* **2011,** 3, (1), 79-84.
175. De Koninck, M.; Marsan, B. *Electrochimica Acta* **2008,** 53, (23), 7012-7021.
176. Park, J.; Risch, M.; Nam, G.; park, m.; Shin, T. J.; Park, S.; Kim, M. G.; Shao-Horn, Y.; Cho, J. *Energy Environment Science* **2017** , 10, 129-136.
177. Jung, J.-I.; Jeong, H. Y.; Lee, J.-S.; Kim, M. G.; Cho, J. *Angewandte Chemie International Edition* **2014,** 53, (18), 4582-4586.
178. Tsvetkov, N.; Lu, Q.; Sun, L.; Crumlin, E. J.; Yildiz, B. *Nature Materials* **2016,** 15, (9), 1010-1016.
179. Caban-Acevedo, M.; Stone, M. L.; Schmidt, J. R.; Thomas, J. G.; Ding, Q.; Chang, H.-C.; Tsai, M.-L.; He, J.-H.; Jin, S. *Nature Materials* **2015,** 14, (12), 1245-1251.
180. Liu, W.; Hu, E.; Jiang, H.; Xiang, Y.; Weng, Z.; Li, M.; Fan, Q.; Yu, X.; Altman, E. I.; Wang, H. *Nature Communications* **2016,** 7, 10771.
181. Nelson, A.; Fritz, K. E.; Honrao, S.; Hennig, R. G.; Robinson, R. D.; Suntivich, J. *Journal of Materials Chemistry A* **2016,** 4, (8), 2842-2848.
182. Asahi, R.; Morikawa, T.; Ohwaki, T.; Aoki, K.; Taga, Y. *Science* **2001,** 293, (5528), 269-271.
183. Fu, J.; Hassan, F. M.; Li, J.; Lee, D. U.; Ghannoum, A. R.; Lui, G.; Hoque, M. A.; Chen, Z. *Advanced Materials* **2016,** 28, (30), 6421-6428.
184. Ma, T. Y.; Dai, S.; Qiao, S. Z. *Materials Today* **2016,** 19, (5), 265-273.
185. Xu, Y.; Lin, Z.; Zhong, X.; Huang, X.; Weiss, N. O.; Huang, Y.; Duan, X. *Nature Communications* **2014,** 5, 4554.
186. Geng, D.; Ding, N.; Andy Hor, T. S.; Liu, Z.; Sun, X.; Zong, Y. *Journal of Materials Chemistry A* **2015,** 3, (5), 1795-1810.
187. Dou, S.; Tao, L.; Huo, J.; Wang, S.; Dai, L. *Energy Environment Science* **2016,** 9, (4), 1320-1326.
188. Morozan, A.; Jegou, P.; Jousselme, B.; Palacin, S. *Physical Chemistry Chemical Physics* **2011,** 13, (48), 21600-21607.
189. Fu, X.; Choi, J.-Y.; Zamani, P.; Jiang, G.; Hoque, M. A.; Hassan, F. M.; Chen, Z. *ACS Applied Material Interfaces* **2016,** 8, (10), 6488-6495.
190. Ha, D.-H.; Moreau, L. M.; Honrao, S.; Hennig, R. G.; Robinson, R. D. *The Journal of Physical Chemistry C* **2013,** 117, (27), 14303-14312.
191. Lu, X.-F.; Gu, L.-F.; Wang, J.-W.; Wu, J.-X.; Liao, P.-Q.; Li, G.-R. *Advanced Materials* **2017** , 29, 1604437.

192. Ling, T.; Yan, D.-Y.; Jiao, Y.; Wang, H.; Zheng, Y.; Zheng, X.; Mao, J.; Du, X.-W.; Hu, Z.; Jaroniec, M.; Qiao, S.-Z. *Nature Communications* **2016,** 7, 12876.
193. de Groot, F. M. F.; Grioni, M.; Fuggle, J. C.; Ghijsen, J.; Sawatzky, G. A.; Petersen, H. *Physical Review B* **1989,** 40, (8), 5715-5723.
194. Luo, K.; Roberts, M. R.; Guerrini, N.; Tapia-Ruiz, N.; Hao, R.; Massel, F.; Pickup, D. M.; Ramos, S.; Liu, Y.-S.; Guo, J.; Chadwick, A. V.; Duda, L. C.; Bruce, P. G. *J. Am. Chem. Soc.* **2016,** 138, (35), 11211-11218.
195. Muller, D. A.; Nakagawa, N.; Ohtomo, A.; Grazul, J. L.; Hwang, H. Y. *Nature* **2004,** 430, (7000), 657-661.
196. Suntivich, J.; Hong, W. T.; Lee, Y.-L.; Rondinelli, J. M.; Yang, W.; Goodenough, J. B.; Dabrowski, B.; Freeland, J. W.; Shao-Horn, Y. *The Journal of Physical Chemistry C* **2014,** 118, (4), 1856-1863.
197. Keast, V. J.; Scott, A. J.; Brydson, R.; Williams, D. B.; Bruley, J. *Journal of Microscopy* **2001,** 203, (2), 135-175.
198. Amri, A.; Jiang, Z.-T.; Bahri, P. A.; Yin, C.-Y.; Zhao, X.; Xie, Z.; Duan, X.; Widjaja, H.; Rahman, M. M.; Pryor, T. *The Journal of Physical Chemistry C* **2013,** 117, (32), 16457-16467.
199. Chen, J.; Wu, X.; Selloni, A. *Physical Review B* **2011,** 83, (24), 245204.
200. Gorlin, Y.; Jaramillo, T. F. *Journal of the American Chemical Society* **2010,** 132, (39), 13612-13614.
201. Li, J.; Sun, L.; Shenai, P. M.; Wang, J.; Zheng, H.; Zhao, Y. *Journal of Alloys and Compounds* **2015,** 649, 973-980.
202. Mueller, D. N.; Machala, M. L.; Bluhm, H.; Chueh, W. C. *Nature Communications* **2015,** 6, 6097.
203. Fu, J.; Cano, Z. P.; Park, M. G.; Yu, A.; Fowler, M.; Chen, Z. *Adv. Mater.* **2017** , 29, 1604685.
204. Fu, J.; Hassan, F. M.; Zhong, C.; Lu, J.; Liu, H.; Yu, A.; Chen, Z. *Advanced Materials* **2017,** 29, (35), 1702526.
205. Yang, S.; Zhao, G.-L.; Khosravi, E. *The Journal of Physical Chemistry C* **2010,** 114, (8), 3371-3375.
206. Liu, Q.-C.; Xu, J.-J.; Xu, D.; Zhang, X.-B. *Nat Commun* **2015,** 6, 7892.
207. Liang, Y.; Wang, H.; Diao, P.; Chang, W.; Hong, G.; Li, Y.; Gong, M.; Xie, L.; Zhou, J.; Wang, J.; Regier, T. Z.; Wei, F.; Dai, H. *Journal of the American Chemical Society* **2012,** 134, (38), 15849-15857.
208. Liu, H.; Zhang, Y.; Li, R.; Sun, X.; Désilets, S.; Abou-Rachid, H.; Jaidann, M.; Lussier, L.-S. *Carbon* **2010,** 48, (5), 1498-1507.
209. Yu, D.; Goh, K.; Wang, H.; Wei, L.; Jiang, W.; Zhang, Q.; Dai, L.; Chen, Y. *Nat Nano* **2014,** 9, (7), 555-562.
210. Yang, J.; Liu, H.; Martens, W. N.; Frost, R. L. *The Journal of Physical Chemistry C* **2010,** 114, (1), 111-119.
211. Rakhi, R. B.; Chen, W.; Cha, D.; Alshareef, H. N. *Nano Letters* **2012,** 12, (5), 2559-2567.
212. Hadjiev, V. G.; Iliev, M. N.; Vergilov, I. V. *Journal of Physics C: Solid State Physics* **1988,** 21, (7), 199.

213. Majzner, K.; Kaczor, A.; Kachamakova-Trojanowska, N.; Fedorowicz, A.; Chlopicki, S.; Baranska, M. *Analyst* **2013,** 138, (2), 603-610.
214. Chen, S.; Duan, J.; Jaroniec, M.; Qiao, S.-Z. *Advanced Materials* **2014,** 26, (18), 2925-2930.
215. Lee, D. U.; Choi, J.-Y.; Feng, K.; Park, H. W.; Chen, Z. *Advanced Energy Materials* **2014,** 4, 1301389.
216. Nyström, G.; Marais, A.; Karabulut, E.; Wågberg, L.; Cui, Y.; Hamedi, M. M. *Nature Communications* **2015,** 6, 7259.